

KAON TAGGING SYSTEM  
AND MEASUREMENT OF THE  $K^+ \rightarrow \pi^+ \gamma \gamma$   
DECAY AT THE NA62 EXPERIMENT AT  
CERN

by

MARIA BRIGIDA BRUNETTI

*A thesis submitted for the degree of  
Doctor of Philosophy*



School of Physics and Astronomy  
College of Engineering and Physical Sciences  
University of Birmingham  
*December 2019*

UNIVERSITY OF  
BIRMINGHAM

**University of Birmingham Research Archive**

**e-theses repository**

This unpublished thesis/dissertation is copyright of the author and/or third parties. The intellectual property rights of the author or third parties in respect of this work are as defined by The Copyright Designs and Patents Act 1988 or as modified by any successor legislation.

Any use made of information contained in this thesis/dissertation must be in accordance with that legislation and must be properly acknowledged. Further distribution or reproduction in any format is prohibited without the permission of the copyright holder.



## Abstract

A model-dependent measurement of the branching ratio of the  $K^+ \rightarrow \pi^+ \gamma \gamma$  decay and a model-independent measurement in bins of the  $z$  kinematic variable, performed on the world's largest data sample, collected by NA62, are presented. In particular, the event selection, the main backgrounds and the addition of an option to bias MC generators to increase the precision of estimates, and the study of systematics are discussed. The combined model-independent branching ratio was found to be  $BR_{MI} = (0.73 \pm 0.04) \times 10^{-6}$ . The implementation in the NA62 high-level trigger framework of decoding tools for the STRAW sub-detector, necessary for running trigger algorithms, and of output structures to transfer data to storage is discussed. The performance of the KTAG sub-detector, which has the task of identifying the kaon component in the NA62 secondary beam, is presented. The sub-detector is shown to meet the efficiency requirements during all the 2016-2018 data-taking.

# DECLARATION OF AUTHOR'S CONTRIBUTION

The present document contains the description of the research I carried out during my PhD; it consists of five chapters. The first chapter gives an introduction to the theoretical framework which describes the analysis I performed, discussed in chapter 5; the second chapter introduces the strategy and the detector of the NA62 experiment, which collected the data I used in the aforementioned analysis. They do not describe my own research work, and are included in this thesis to provide context for the following chapters.

The third chapter provides an overview of the NA62 trigger system; it then proceeds to discuss my own contribution to such framework. In particular, the encoder for the STRAW read-out boards, and the output structures used to write triggered data to storage are my own work.

The fourth chapter is dedicated to the KTAG, the sub-detector in charge of tagging kaons in the NA62 secondary beam. Its design, its working principles and its operational procedures, discussed in the first part of the chapter, are the result of the work of the whole KTAG group. A discussion of my personal contributions follows; in particular, I performed the sub-detector's performance studies for the 2016-2018 data-taking.

The final chapter describes in detail the main project of my PhD, that is the analysis of the  $K^+ \rightarrow \pi^+ \gamma \gamma$  decay. All the strategy and results presented in this chapter, unless otherwise specified, are the outcome of my own research.

I have furthermore contributed to the NA62 experiment operation by taking numerous shifts and serving as on-call expert for the KTAG, the High-Level trigger system and the Online Monitor throughout the 2016-2018 data-taking. No other qualifications have been achieved with the work reported in this thesis.

# ACKNOWLEDGEMENTS

This work would not have been possible without the support of many people.

I would like to thank in the first place the members of the NA62 group in Birmingham for providing a friendly and positive learning environment. The biggest thanks go to Cristina, for her gentle and well-directed supervision, her constant support, and for always suggesting practical solutions to any kind of problem. Further than that, Cristina helped me a lot to overcome difficulties and unexpected life circumstances. I am grateful for all the enthusiasm and passion she communicated to me, and for involving me in multiple outreach activities.

I would like to particularly thank Nicolas for providing further guidance in my analysis work, both on physics and on computing, for always being there when I needed him, and for being a good friend in all other circumstances; working with him has been a pleasure.

Throughout my PhD I also received excellent support from other members of the group; from all of them I learned a lot, and in them I have found good friends. With Tonino I shared many interesting conversations, and from him I learned a lot on a large number of topics; his advice has always been extremely reliable and useful, and his presence has enriched my PhD experience. Angela showed me how to navigate the trigger framework, gave me precious advice on many other aspects of my work and brought a bit of homely sunshine whenever she entered the room. Francesco has been a great friend, and patiently endured my bad moods trying to give helpful advice - which he knows I not often listened to. Chris, who sat at the other side of the wall, has provided me with a lot of good advice, good laughs and long enjoyable chats, that I will greatly miss. I am very grateful to John Fry for reading my thesis and providing extremely useful advice, comments and

corrections, and for kindly and steadily helping me keep track of my progress.

I would like to thank the whole particle physics group at the University of Birmingham; I really enjoyed the atmosphere in the group, the many friendly interactions with staff and students. I enjoyed the company of many great people in my office. A special mention goes to Lorenza, who shared with me joys and tears during this hard path; I do not know what I would have done if I could not turn to her for words of empathy and cheerfulness. I would like to thank everyone else for tolerating with patience our many loud chats in Italian, but also for the nice time together.

I owe many thanks to several members of the NA62 collaboration: in particular Giuseppe, Karim and Riccardo F., for their precious advice on multiple aspects of my work, but also all the colleagues and friends I shared shifts, laughs, travels and meals with.

Many, many thanks go to Kristian and Georgios, with whom I started this adventure more than four years ago, and then shared many more: I will forever cherish the memories of our trips, our coffees, our climbing nights, and all the support we gave each other; it all made my early PhD years pretty special.

Although Elliot is part of the above group too, I wish to thank him separately, as I share with him the biggest adventure. He supported me and motivated me to persist when everything seemed dark, to find the courage to decide to keep doing research after my PhD, and to look at the future with optimism; he has given me and gives me every day much more than I can put into words.

From the past years in Birmingham I will remember many people and periods with affection. I remember with pleasure my time with Rosanna, who should definitely have stayed in Birmingham. I have fond memories of my acting classes, and all the trips I made and the people I shared them with. I need to thank of course my old time friends, those who were close before and after I moved here: Fabrizia and Francesco, with whom I managed to stay in touch despite very long distances and who made me feel at home away from home every single day, Martina, especially for our frequent meetings during

her time in Oxford, her advice and her numerous words of encouragement, my friends from my undergraduate years and beyond.

Lastly I wish to thank my family, for being always supportive and understanding despite the long distance. I know they would rather have me closer to home, but I hope they are proud of this achievement.

Finally, this work would not have been possible without a big dose of resilience, of patience, and courage to proceed despite the difficulties; I dedicate this work to whoever is struggling - be always kind to yourself.

# CONTENTS

<b>1</b>	<b>Rare kaon decays</b>	<b>3</b>
1.1	The Standard Model of particle physics . . . . .	3
1.1.1	Quark mixing . . . . .	5
1.2	Kaons and physics beyond the SM . . . . .	8
1.2.1	The $K^+ \rightarrow \pi^+ \nu \bar{\nu}$ and $K_L \rightarrow \pi^0 \nu \bar{\nu}$ decays . . . . .	11
1.2.2	Further searches for physics beyond the SM . . . . .	15
1.3	Symmetries in QCD . . . . .	17
1.3.1	Flavour symmetry . . . . .	17
1.3.2	Axial symmetry . . . . .	19
1.3.3	Chiral symmetry . . . . .	20
1.3.4	Chiral symmetry realization modes . . . . .	20
1.3.5	Effective field theories . . . . .	21
1.3.6	ChPT . . . . .	22
1.3.7	The $K^+ \rightarrow \pi^+ \gamma \gamma$ decay . . . . .	24
<b>2</b>	<b>The NA62 experiment</b>	<b>30</b>
2.1	The experimental strategy . . . . .	30
2.2	The NA62 beam . . . . .	33
2.3	The NA62 detector . . . . .	36
2.3.1	The CEDAR/KTAG . . . . .	36
2.3.2	The GTK . . . . .	38
2.3.3	The CHANTI . . . . .	41

2.3.4	The STRAW . . . . .	41
2.3.5	The Photon Veto System . . . . .	43
2.3.6	The RICH . . . . .	49
2.3.7	The CHOD and the OldCHOD . . . . .	50
2.3.8	The MUV1 and MUV2 . . . . .	51
2.3.9	The MUV3 . . . . .	52
2.3.10	The MUV0 and the HASC . . . . .	52
2.3.11	Summary . . . . .	53
<b>3</b>	<b>The NA62 data-acquisition, trigger and software</b>	<b>54</b>
3.1	The trigger system . . . . .	54
3.1.1	The data flow from detection to storage . . . . .	55
3.2	The NA62 DAQ system . . . . .	60
3.3	The NA62 L0 trigger . . . . .	62
3.4	The NA62 HLT . . . . .	64
3.4.1	The NA62 software framework . . . . .	64
3.4.2	The NA62 Online System . . . . .	65
3.4.3	The testing environment . . . . .	65
3.5	The Online System software framework . . . . .	66
3.5.1	Tools for running HLT algorithms for the SRBs . . . . .	68
3.5.2	HLT output structures . . . . .	69
3.5.3	Summary . . . . .	69
<b>4</b>	<b>The CEDAR/KTAG sub-detector</b>	<b>70</b>
4.1	CERN CEDARs principles of operation . . . . .	71
4.1.1	Ring broadening effect . . . . .	73
4.2	The NA62 CEDAR/KTAG sub-detector's description . . . . .	75
4.2.1	The KTAG's PMTs . . . . .	82
4.2.2	The KTAG's read-out and reconstruction . . . . .	82

4.2.3	Light spectrum, detection efficiency and time resolution . . . . .	87
4.3	Procedures, monitoring and performance assessment . . . . .	92
4.3.1	Preliminary procedures for data-taking . . . . .	93
4.3.2	Online data monitoring . . . . .	98
4.3.3	Offline sub-detector performance assessment . . . . .	103
4.4	Conclusions . . . . .	112
<b>5</b>	<b>Measurement of the BR of <math>K^+ \rightarrow \pi^+ \gamma \gamma</math></b>	<b>113</b>
5.1	Measurement strategy . . . . .	113
5.1.1	Decays of the charged kaon . . . . .	114
5.1.2	Data samples and trigger lines . . . . .	115
5.1.3	Filter . . . . .	115
5.2	Data selection . . . . .	116
5.3	Study of backgrounds . . . . .	120
5.3.1	Implementation of biased MC generators . . . . .	124
5.4	Measurement of the BR . . . . .	128
5.4.1	Model-dependent BR estimate . . . . .	130
5.4.2	Model-independent BR estimate . . . . .	130
5.5	Study of systematics . . . . .	132
5.5.1	BR dependence on the model parameters . . . . .	133
5.5.2	Systematic uncertainties from z bin migration . . . . .	135
5.5.3	Systematic uncertainty from the accidental combinations of one track and two clusters . . . . .	135
5.5.4	BR dependence on cluster merging . . . . .	136
5.5.5	BR dependence on cluster distance . . . . .	138
5.5.6	Summary and prospects . . . . .	138
	<b>Bibliography</b>	<b>148</b>

# INTRODUCTION

The Standard Model (SM) of particle physics provides high-precision predictions on a large number of phenomena; however, in the recent past, many shortcomings of the model have become evident, of which a notable example is given by the observation of non-zero neutrino mass differences [1]. Furthermore, tensions are observed between experimental observations and theoretical predictions in many high-energy physics measurements, such as LHCb at the Large Hadron Collider [2, 3].

A possible way to probe physics beyond the SM is to progressively increase the energy at colliders to allow the production of new particles. A different approach, less limited by accelerator technology advancements, is that of performing precision measurements of highly suppressed decay channels, such as Flavour-Changing Neutral Currents. Examples are the decay of  $B_s$  mesons to two muons, performed at the LHCb [4], or that of the  $K^+ \rightarrow \pi^+ \nu \bar{\nu}$  currently being measured at the NA62 experiment at CERN [5]. The latter channel is particularly effective in discriminating between several new physics scenarios when it is compared to that of the neutral channel  $K_L \rightarrow \pi^0 \nu \bar{\nu}$ , currently under study at the KOTO experiment at JPARC [6]. Besides these golden modes, a broad program of kaon searches and measurements, many of which are sensitive to new physics, is carried out at NA62.

This thesis reports the result of the research I carried out on the NA62 experiment during my PhD at the University of Birmingham. The document is organised in five chapters. In the first chapter, a brief overview of the SM of particle physics and the historical milestones in kaon physics is given, followed by a discussion of the frontiers and open questions in the field and the current experimental scenario for kaon research. Chiral

Perturbation Theory is presented in detail, as it describes meson interactions in the low-energy, non-perturbative quantum chromodynamics regime, including the  $K^+ \rightarrow \pi^+ \gamma \gamma$  which is the main project of my PhD.

The second chapter is dedicated to the description of the NA62 experiment; its main goal and challenges, and its beam and detector are presented to provide context to the content of the following chapters.

The third chapter is focused on the NA62 Trigger System, and in particular the High-Level Trigger, which I contributed to in the first months of my PhD. An overview of the system is given, and my personal contribution, related to the development of a decoding tool that allows running trigger algorithms for the STRAW sub-detector, and the implementation of output structures to write data to storage, is discussed.

The fourth chapter is dedicated to the KTAG sub-detectors, which has the task of identifying the 6% kaon component in the NA62 unseparated beam and therefore is of primary importance for the measurement of  $K^+ \rightarrow \pi^+ \nu \bar{\nu}$ . During my PhD I was trained as an expert for this sub-system, and have been on-call for several data-taking periods. Further than this, I have carried out studies to assess the sub-detector's performance for data collected between 2016 and 2018. The result of these studies is presented in this chapter.

The fifth chapter contains a full description of a model-dependent and a model-independent measurement of the BR of the  $K^+ \rightarrow \pi^+ \gamma \gamma$  decay that I performed on NA62 data. The decay signature and the event selection, the backgrounds, the study of systematics and the results and prospects of the analysis are discussed.

# CHAPTER 1

## RARE KAON DECAYS

Since their discovery in 1947 [7], kaons have played a central role in expanding our understanding of particle physics phenomena. In this chapter, after a brief overview of the Standard Model (SM) of particle physics and the historical role of kaons in its development, the ongoing kaon physics scenario, focused on the study of rare decays, will be discussed. The broad kaon physics programme carried out at the NA62 experiment, part of this scenario, will be examined. The main goal of the experiment is the measurement of the ultra-rare decay  $K^+ \rightarrow \pi^+ \nu \bar{\nu}$ , which proceeds at leading order via loop diagrams and is sensitive to new physics contributions. The scope of the experiment also includes the measurement of the  $K^+ \rightarrow \pi^+ \gamma \gamma$  decay, that I carried out in my PhD, which constrains Chiral Perturbation Theory (ChPT), an effective theory that describes mesons interactions in the non-perturbative QCD domain. In order to understand the relevance of the latter process, a sub-section of this chapter will be devoted to ChPT.

### 1.1 The Standard Model of particle physics

The SM of particle physics is a mathematical model developed in the second half of the last century that provides a unified framework for the description of particle physics phenomena. The particle content of the model consists of three generations of left-handed (LH) quarks and leptons and of the corresponding right-handed (RH) antiparticles. Quarks

and leptons form doublets under the *weak isospin*  $SU(2)_L$  symmetry:

$$\begin{pmatrix} u \\ d \end{pmatrix} \quad \begin{pmatrix} c \\ s \end{pmatrix} \quad \begin{pmatrix} t \\ b \end{pmatrix}$$

$$\begin{pmatrix} e \\ \nu_e \end{pmatrix} \quad \begin{pmatrix} \mu \\ \nu_\mu \end{pmatrix} \quad \begin{pmatrix} \tau \\ \nu_\tau \end{pmatrix}$$

whereas antiparticles transform as singlets under  $SU(2)_L$ . The  $SU(2)_L$  group describes weak charged current interactions. By introducing the symmetry group of *weak hypercharge*  $U(1)_Y$ , a unified description of weak neutral current and electromagnetic interactions is obtained. The mediators of electroweak interactions are the photon  $\gamma$  and the massive gauge bosons  $W^\pm$  and  $Z^0$ .

The three generations of quarks and leptons are referred to with the label *flavour*. Quarks are distinguished, further to their flavour, by a quantum number called *colour*, that has in quantum chromodynamics (QCD), the theory of strong interactions, a role analogous to the electric charge in quantum electrodynamics (QED). Each quark exists in three different colours (R, G, B); the underlying symmetry group is  $SU(3)_C$ . The carriers of the strong force are called *gluons*; they come in eight types each characterised by a different color combination, as many as the generators of  $SU(3)_C$ . Baryons and mesons must have zero colour quantum number because of *colour confinement*; they are  $SU(3)_C$  singlets.

The combined strong and electroweak interactions are described, in the SM, by the following group product:

$$SU(3)_C \otimes SU(2)_L \otimes U(1)_Y \tag{1.1}$$

The final constituent is a neutral Higgs scalar H, generated by a spontaneous symmetry breaking mechanism with the potential:  $V(\phi) = -\mu^2\phi\phi^\dagger + \lambda(\phi\phi^\dagger)^2$ , where  $(\phi^+, \phi^0)$  form a

complex scalar Higgs doublet added to the model to generate Yukawa masses for fermions.

### 1.1.1 Quark mixing

The particles in the doublets previously described are eigenstates of weak interactions. They are, however, not mass eigenstates. If the upper members of the doublets are taken to be mass eigenstates, the mass eigenstates lower members are linear combinations of the interaction eigenstates. For the quark sector, the relation is  $d'_i \equiv \sum_j V_{ij} d_j$ , where  $i$  and  $j$  are generation labels running from 1 to 3, and  $V_{ij}$  is the quark mixing matrix or Cabibbo-Kobayashi-Maskawa (CKM) matrix [8]. The relation describing the mixing of the lower members of the first two generations was first postulated by N. Cabibbo [9] when the charm quark was discovered. In that case, the mixing was described in terms of a single angle  $\theta_C$ . In matrix form:

$$\begin{pmatrix} d' \\ s' \end{pmatrix} = \begin{pmatrix} V_{ud} & V_{us} \\ V_{cd} & V_{cs} \end{pmatrix} \begin{pmatrix} d \\ s \end{pmatrix} = \begin{pmatrix} \cos\theta_C & \sin\theta_C \\ -\sin\theta_C & \cos\theta_C \end{pmatrix} \begin{pmatrix} d \\ s \end{pmatrix}$$

Where  $\theta_C \sim 13$  deg. The matrix was later extended by Kobayashi and Maskawa after the discovery of the last generation of quarks.

$$\begin{pmatrix} d' \\ s' \\ b' \end{pmatrix} = \begin{pmatrix} V_{ud} & V_{us} & V_{ub} \\ V_{cd} & V_{cs} & V_{cb} \\ V_{td} & V_{ts} & V_{tb} \end{pmatrix} \begin{pmatrix} d \\ b \\ s \end{pmatrix}$$

Several parametrisation can be chosen to represent the CKM elements. L. Wolfenstein's parametrisation highlights the matrix main characteristics. The four parameters in this case are  $(\lambda, A, \rho, \eta)$ , and the CKM matrix takes the form:

$$V_{CKM} = \begin{pmatrix} 1 - \frac{\lambda^2}{2} & \lambda & A\lambda^3(\bar{\rho} - i\bar{\eta}) \\ -\lambda & 1 - \frac{\lambda^2}{2} & A\lambda^2 \\ A\lambda^3(1 - \bar{\rho} - i\bar{\eta}) & -A\lambda^2 & 1 \end{pmatrix} \quad (1.2)$$

the relations between the CKM elements in the two parametrisations are the following:

$$\sin \theta_C = s_{12} = \lambda = \frac{|V_{us}|}{\sqrt{|V_{ud}|^2 + |V_{us}|^2}} \quad (1.3)$$

$$s_{23} = A\lambda^2 = \lambda \left| \frac{V_{cb}}{V_{us}} \right| \quad (1.4)$$

$$s_{13}e^{i\delta} = V_{ub}^* = \frac{A\lambda^3(\bar{\rho} + i\bar{\eta})\sqrt{1 - A^2\lambda^4}}{\sqrt{1 - \lambda^2[1 - A^2\lambda^4(\bar{\rho} + i\bar{\eta})]}} \quad (1.5)$$

From (1.2) it is immediately evident that a hierarchy exists: the elements on the main diagonal are  $\approx 1$ , and the elements connecting near generations are larger than those connecting far generations.

The CKM matrix is unitary. This yields six vanishing combinations:

$$\sum_i V_{ij}V_{ik}^* = \delta_{jk} \quad (1.6)$$

$$\sum_j V_{ij}V_{kj}^* = \delta_{ik} \quad (1.7)$$

The above conditions can be represented, in the complex plane, as triangles. All the triangles have the same area, given by half the Jarlskog invariant  $J$ . The invariant provides a phase-convention-independent measurement of CP-violation. Its value is defined by:  $\Im[V_{ij}V_{kl}V_{il}^*V_{kj}^*] = J \sum_{m,n} \epsilon_{ikm}\epsilon_{jln}$ . The triangle that is most commonly used is given by the relation:

$$V_{ud}V_{ub}^* + V_{cd}V_{cb}^* + V_{td}V_{tb}^* = 0 \quad (1.8)$$

which, when dividing it by the best-known product  $V_{cd}V_{cb}^*$ , has vertices in  $(0,0)$ ,  $(1,0)$  and  $(\bar{\rho}, \bar{\eta})$ . The triangle, known as *unitarity triangle*, is shown in fig. 1.1. An analogous matrix, the Pontecorvo-Maki-Nagasawa-Sakata (PMNS) matrix, determines mixing in the lepton sector.

The current status of constraints on the CKM parameters is shown in fig. 1.2. By measuring the unitarity triangle, one can constrain the SM or, in case anomalies are detected, probe physics beyond the SM. Therefore, constraining the CKM triangle is one

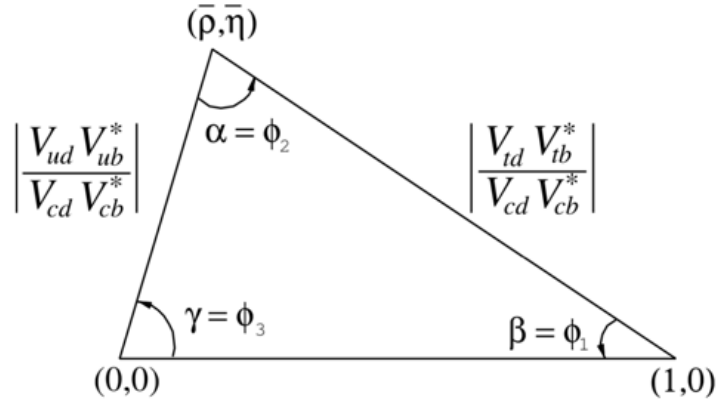


Figure 1.1: Unitarity triangle, which is a representation in the complex plane of one of the CKM matrix unitarity conditions. [10].

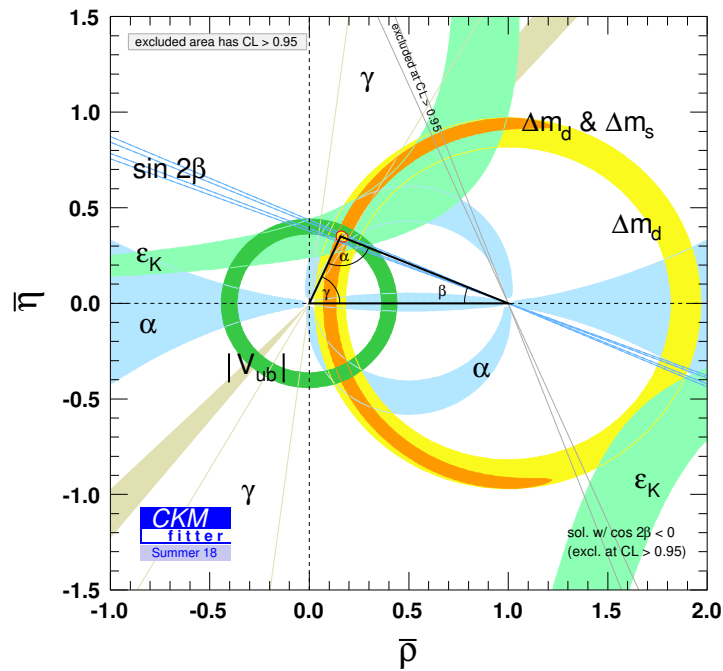


Figure 1.2: Current constraints on the CKM unitarity triangle, as determined by global fits to experimental results; the red-hatched region of the global combination at the top of the triangle corresponds to a 68% exclusion region. [10].

of the goals of flavour physics. At present, several anomalies have been observed, many of which in the B sector. They include [2, 3]:

- tests of lepton flavour universality in  $R_{K^{(*)}} = B \rightarrow K^{(*)}\mu\mu/B \rightarrow K^{(*)}ee$ , exceeding SM predictions by 2.5( $R_K$ ) and 2.4 ( $R_{K^{(*)}}$ ) standard deviations respectively;
- tests of lepton flavour universality in  $R_{D^{(*)}} = B \rightarrow D^{(*)}\tau\bar{\nu}/B \rightarrow D^{(*)}l\bar{\nu}$ , with  $l = e, \mu$ , exceeding SM predictions by 2.3 ( $R_D$ ) and 3.4 ( $R_{D^{(*)}}$ ) standard deviations respectively;
- discrepancy in the SM predictions and experimental values for angular observables such as  $P'_5$  in  $B \rightarrow K^{(*)}\mu^+\mu^-$  decays, exhibiting a discrepancy with the SM predictions of 3.3 standard deviations [11];
- The experimental value of the BR of  $B_s \rightarrow \phi\mu^+\mu^-$  is smaller than the SM prediction by 3.7 standard deviations.

Aside from finding tensions with the SM, a promising avenue to search for physics beyond the SM consists in constraining the BR of ultra-rare decays, such as flavour-changing neutral currents (FCNCs). The LHCb experiment has recently published new physics-constraining results on the decay rate of  $B_s$  mesons to two muons [4]. The measurement of the BR of the ultra-rare decay  $K^+ \rightarrow \pi^+\nu\bar{\nu}$  at NA62 is discussed in the following sections and chapters.

The constraints to the CKM matrix coming from the kaon sector are discussed in the next sections.

## 1.2 Kaons and physics beyond the SM

Kaons allowed us to lay down many fundamental pieces of the SM. With kaons, the idea of strangeness has been introduced for the first time [12]. As a consequence, the oscillation of neutral mesons was postulated [13], and laws of physics previously considered to hold

universally were observed to be violated in certain weak processes. This was the case for the parity symmetry [14, 15]. Following the discovery of parity violation, a violation of CP, which transforms a left-handed particle into its right-handed antiparticle, was observed, both indirectly [16] and directly [17, 18]. Kaons played a role in the introduction of the three quark-model to explain the spectra of mesons and baryons observed experimentally [19]. The necessity to explain why FCNC kaon decays such as  $K_L \rightarrow \mu^+ \mu^-$  were not observed led to the formulation of the GIM mechanism, in which the charm was added for the first time to the three-quark scenario [20].

Rare kaon decays today still play a central role in particle physics. They can in fact shed light on some very fundamental open questions, such as the following [21]:

- Do new sources of CP violation exist other than a single phase in the CKM matrix predicted by the Kobayashi-Maskawa mechanism [8]? This is motivated, among other reasons, by baryogenesis [22], a mechanism to explain the matter-antimatter asymmetry in the universe deduced from nucleosynthesis and Cosmic Microwave Background Radiation, where the observed asymmetry is much larger than that predicted by the SM;
- Does lepton universality hold? This question can be tackled, for example, by comparing the ratio of semi-leptonic kaon decays to electrons and two muons, e.g.  $R_K = K^+ \rightarrow e \nu_e(\gamma) / K^+ \rightarrow \mu \nu_\mu(\gamma)$  [23];
- Can we constrain the SM or find new physics in rare decays? A very promising kaon channel to study to this end is the loop-mediated process  $K^+ \rightarrow \pi^+ \nu \bar{\nu}$ , currently being measured at the NA62 experiment at CERN and discussed later in this chapter.

Rare kaon decays, involved in the last questions, are particularly interesting because they are very precisely predicted in the SM and they are not affected by large hadronic uncertainties. Among these, four main areas of investigation are identified [10]:

1. Searches for decays that explicitly violate the SM;

2. Studies of ultra-rare decays with small theoretical uncertainties;
3. Studies of modes with low energy strong interactions;
4. Studies of additional modes that constrain SM parameters.

The four categories are interconnected and together fully constrain the CKM unitarity triangle. This is illustrated in fig. 1.3.

The first group includes searches for lepton flavour violating (LFV) and lepton number violating (LNV) decays. Examples of these processes are  $K_L \rightarrow \mu^\pm e^\mp$ ,  $K^+ \rightarrow \pi^+ e^\mp \mu^\pm$  and  $K_L \rightarrow \pi^0 e^\mp \mu^\pm$ . LFV decays are predicted in many extensions of the SM. In these models, they are mediated by LFV vector bosons with masses above 100 TeV; measurements of these decay modes thus allow high energy scales to be probed [24]. Studies of LNV decays are also of interest, as such channels constrain possible extensions of the SM in the neutrino sector. At NA62, the  $K^+ \rightarrow \pi^- e^+ e^+$  and  $K^+ \rightarrow \pi^- \mu^+ \mu^+$  channels, that violate lepton number conservations by two units and may therefore be mediated by Majorana neutrinos, are being measured [25]. Searches for new particles in the  $K^+ \rightarrow \pi^+ X^0$  mode, with  $X^0$  including both long-lived and short-lived particles, fall under this category as well.

The second group includes the FCNC decay  $K^+ \rightarrow \pi^+ \nu \bar{\nu}$  decay and the neutral mode  $K_L \rightarrow \pi^0 \nu \bar{\nu}$ . These will be described in more detail in the next subsections.

The third group includes processes where long-distance contributions are dominant, such as  $K^+ \rightarrow \pi^+ \gamma \gamma$ . Through the study of these channels one can test ChPT, an effective field theory that describes strong interactions at low energy, which will be discussed in section 1.3.6. The  $K^+ \rightarrow \pi^+ \gamma \gamma$  decay is discussed in the framework of ChPT in section 1.3.7. The measurement that I performed with NA62 data is fully described in chapter 5. The  $K_L \rightarrow \pi^0 \gamma \gamma$  and  $K_L \rightarrow l^+ l^- \gamma$  decays belong to this category as well; by measuring them, information on kaon decays belonging to other groups is obtained, as shown in fig. 1.3.

The last group includes decays that are sensitive to SM parameters with final state

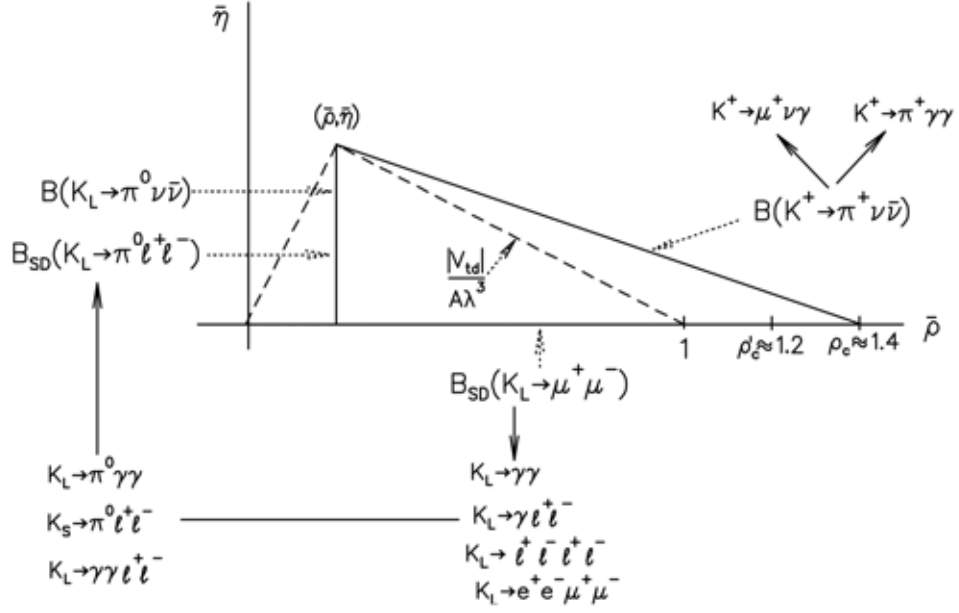


Figure 1.3: The unitarity triangle and the rare kaon decays that play a role in constraining its parameters. The solid arrows indicate auxiliary modes that help obtaining the main results, or that constitute background for them. [10]

leptons, such as  $K_L \rightarrow \pi^0 l^+ l^-$  and  $K_L \rightarrow l^+ l^-$ , with  $l = e, \mu$ . These processes are affected by multiple hadronic uncertainties that the modes belonging to the third group can contribute to estimate.

### 1.2.1 The $K^+ \rightarrow \pi^+ \nu \bar{\nu}$ and $K_L \rightarrow \pi^0 \nu \bar{\nu}$ decays

The  $K^+ \rightarrow \pi^+ \nu \bar{\nu}$  and  $K_L \rightarrow \pi^0 \nu \bar{\nu}$  decays are FCNC processes. Therefore, there is no contribution to their BR at tree level. The leading orders are loop diagrams such as electroweak penguins or z-box (see fig. 1.5). As the largest contribution comes from the top quark loop, the decay is short-distance dominated, with a small contribution from the charm quark loop. Moreover, the hadronic matrix element is expressed in terms of that of the very well-measured decay  $K^+ \rightarrow \pi^0 e \nu_e$ . It follows that intrinsic theoretical uncertainties on the prediction of the BR of this decay are due to QCD corrections to the top and charm quark contributions; they are of the order of 2%, the rest of the uncertainty being dominated by the uncertainty on the CKM matrix elements. The BR can be written

in a compact form in terms of the CKM parameters  $V_{cb}$ ,  $\bar{\rho}$  and  $\bar{\eta}$ :

$$BR(K^+ \rightarrow \pi^+ \nu \bar{\nu}) = 1.6 \times 10^{-5} |V_{cb}|^4 [\sigma \bar{\eta}^2 + (\rho_c - \bar{\rho})^2] \quad (1.9)$$

where  $\rho_c \approx 1.45$  and  $\sigma \equiv 1/(1 - \frac{1}{2}\lambda^2)^2$ . The theoretical prediction of the BR is:

$$BR(K^+ \rightarrow \pi^+ \nu \bar{\nu}) = (8.3 \pm 0.4) \times 10^{-11}. \quad (1.10)$$

The  $K^+ \rightarrow \pi^+ \nu \bar{\nu}$  decay was observed before by the BNL-787 and BNL-949 experiments; in particular, they observed respectively two and one candidate events in the clean high  $\pi^+$  momentum region and one and three in the low-momentum region. The measured BR is:

$$BR(K^+ \rightarrow \pi^+ \nu \bar{\nu}) = (1.73_{-1.05}^{+1.15}) \times 10^{-10} \quad (1.11)$$

NA62 expects to make a 10% precision measurement of the BR of  $K^+ \rightarrow \pi^+ \nu \bar{\nu}$ ; the observed events over the first data sets are in agreement with the SM predictions [5]. The combined results from the 2016 and 2017 data samples yield the following two-sided 68% band BR:

$$BR(K^+ \rightarrow \pi^+ \nu \bar{\nu}) = (0.47_{-0.47}^{+0.72}) \times 10^{-10}. \quad (1.12)$$

The neutral channel  $K_L \rightarrow \pi^0 \nu \bar{\nu}$  is characterised by a very clean BR, free of the hadronic uncertainties that affect the charged mode. It is dominated by a top-quark intermediate state, and it therefore has no uncertainty related to a charm quark contribution. Its BR can be written as:

$$BR(K_L \rightarrow \pi^0 \nu \bar{\nu}) = \mathfrak{K}_L \left( \frac{Im(V_{ts}^* V_{td})}{\lambda^5} X_t \right)^2 \approx 7.6 \times 10^{-5} |V_{cb}|^4 \bar{\eta}^2 \quad (1.13)$$

where the hadronic matrix element is related to that of the decay  $K_L \rightarrow \pi^\pm l^\mp \nu_l$  and it is parametrised in  $\mathfrak{K}_L$ . In models with lepton flavour conservation, the decay is fully CP-violating. The theoretical prediction is  $BR(K_L \rightarrow \pi^0 \nu \bar{\nu}) = (2.9 \pm 0.2) \times 10^{-11}$ . The

$K_L \rightarrow \pi^0 \nu \bar{\nu}$  decay is under study at the KOTO experiment at JPARC. An upper limit at 90% CL based on the 2015 data sample has been published [6]:

$$BR(K_L \rightarrow \pi^0 \nu \bar{\nu}) < 3.0 \times 10^{-9} \quad (1.14)$$

By combining the measurements of the BR for the charged and the neutral channel, it is possible to distinguish between several new physics scenarios. Furthermore, a measurement of the ratio of the BR of the two channels allows a clean measurement of a CP-violating phase generated in the SM, new physics models or a mix of the two [26].

In fig. 1.4 the correlation between the two channels is plotted according to various new physics models is shown, and the SM predictions are indicated by a black cross. The grey area in the plot represents the Grossman-Nir bound, a limit on the  $BR(K_L \rightarrow \pi^0 \nu \bar{\nu})$  determined by the experimental value of  $BR(K^+ \rightarrow \pi^+ \nu \bar{\nu})$  [26].

By a combined study of the BRs it is possible to distinguish between three classes of NP models:

- Models with a flavour interactions CKM-like structure, such as Minimal Flavour Violation (MFV) models, based on the flavour symmetry of the SM in the quark sector, and  $U(2)^3$  models (green branches in fig. 1.4) [27];
- Models with new flavour and CP-violating interactions, with either LH or RH dominant currents, such as the composite Higgs model Littlest Higgs with T-parity (LHT) or Z, Z' FCNC scenarios (blue branches in fig. 1.4) [28–30];
- Models producing weak or no correlation, such as Randall-Sundrum models with custodial protection (red region in fig. 1.4) [31].

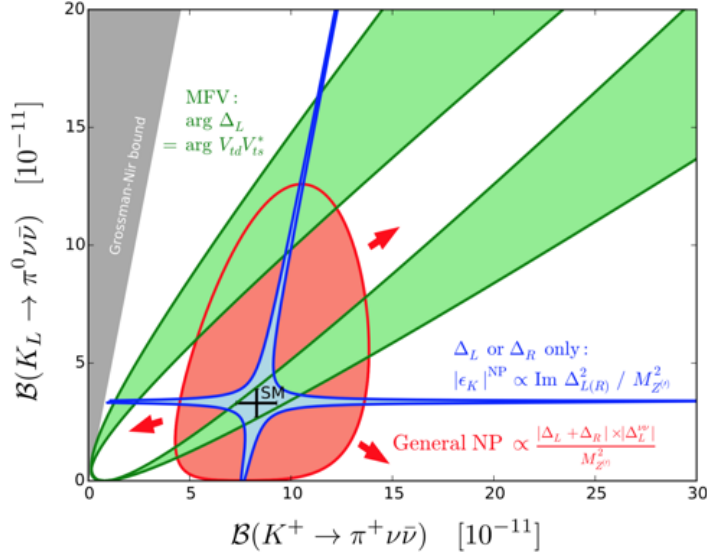


Figure 1.4: Correlation between the  $BR(K^+ \rightarrow \pi^+ \nu \bar{\nu})$  and the  $BR(K_L \rightarrow \pi^0 \nu \bar{\nu})$  channel according to various new physics models. The black cross indicates the SM prediction, while the grey area represents the Grossman-Nir bound. [32]

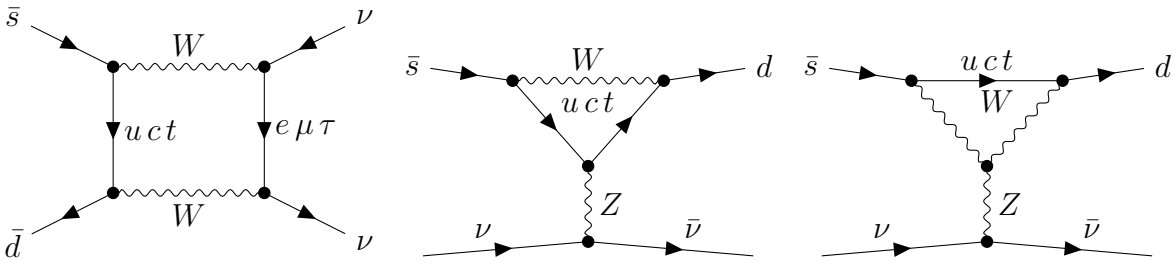


Figure 1.5: The FCNC process  $K^+ \rightarrow \pi^+ \nu \bar{\nu}$  is forbidden at tree level. Its leading order contributions are one-loop diagrams such as W box (left) and electroweak penguin (center and right).

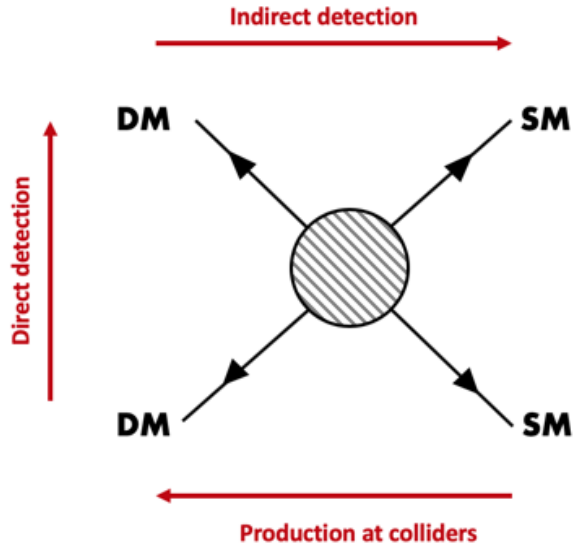


Figure 1.6: Experimental strategies for dark matter searches: the red arrow on top indicates the indirect detection of dark matter particles via the production of SM particles; the red arrow on the left indicates the collision of DM and SM particles; the red arrow at the bottom indicates the production of DM particles at colliders.

### 1.2.2 Further searches for physics beyond the SM

Decay channels and observables sensitive to new physics in the flavour sector have been discussed in the previous section. Further efforts are made, outside the field of flavour physics, to explore new physics scenarios that tackle tensions within the SM, and/or account for phenomena not predicted by it. The latter category includes, notably, the observation of dark matter (DM). Dark matter can be searched in three main ways:

- directly, for example through the recoil of dark-matter particles off target nuclei. The DAMA experiment, looking for weakly interacting massive particles (WIMPs) DM candidates, reported a signal at  $12.9 \sigma$  over 7 years of exposure [33];
- indirectly, via the decay or the annihilation of dark matter particles and detection of their decay products. The best upper limit comes from SuperKamiokande [34];
- in production at colliders, as shown in fig. 1.6.

The latter strategy is pursued at the Large Hadron Collider (LHC). Ongoing searches

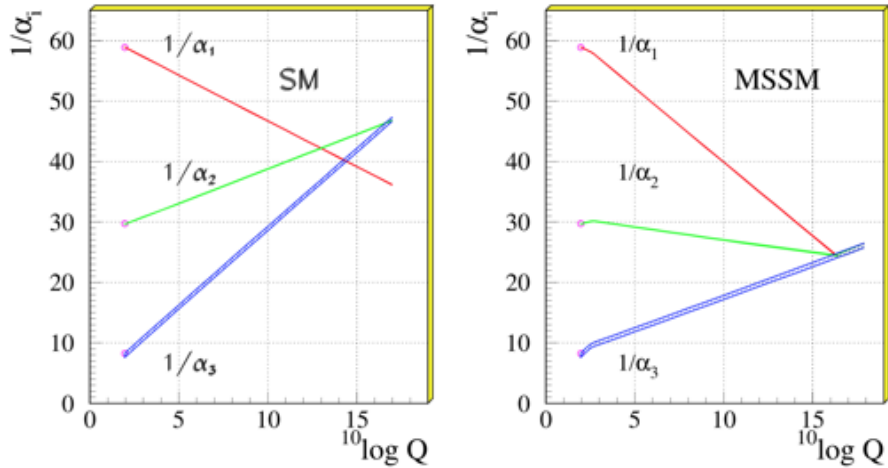


Figure 1.7: Gauge couplings running in the SM, on the left, and in the Minimal Supersymmetric extension of the SM (MSSM), on the right. Supersymmetric corrections to the gauge coupling runnings allow forces unification. [43]

aim at testing: *portal* models, where a new particle [35, 36], the Z or the Higgs boson mediates the DM–SM interaction; supersymmetric models [37–40]; Higgs decay to invisibles [41]. Further open questions include [42]:

- The hierarchy problem, namely the large difference between the Higgs mass scale ( $\approx 100$  GeV) and the Planck mass scale ( $\approx 10^{18}$  GeV), assumed to be the energy at which forces unification occurs;
- The origin of the hierarchical pattern in quarks and charged leptons masses, and in quark mixing;
- The gauge coupling unification problem: the three couplings of the weak, strong and EM forces do not meet precisely when extrapolated to high energies within the SM (see fig. 1.7);
- The strong CP problem, that is the absence of observed CP violation in QCD.

## 1.3 Symmetries in QCD

### 1.3.1 Flavour symmetry

As previously discussed, the SM contains six types or *flavours* of quarks. The following discussion applies to a scenario with an arbitrary number  $N_f$  of flavours. QCD, the theory that describes strong interactions in the SM, is encoded in the SU(3) component of the group product in eq. (1.1). The Lagrangian of QCD is the following [10]:

$$\mathfrak{L} = \sum_q \bar{\psi}_{q,a} (i\gamma^\mu \partial_\mu \delta_{ab} - g_s \gamma^\mu t_{ab}^C \mathfrak{A}_\mu^C - m_q \delta_{ab}) \psi_{q,b} - \frac{1}{4} F_{\mu\nu}^A F^{A\mu\nu} \quad (1.15)$$

where summation over repeated indices is assumed, and:

- $\gamma^\mu$  indicates the Dirac  $\gamma$ -matrices;
- $\psi_{q,a}$  are field spinors for quarks of flavour  $q$  and mass  $m_q$ , and  $a$  is the color index running from 1 to  $N_c = 3$ ;
- $\mathfrak{A}_\mu^C$  are the gluon fields, where C runs from 1 to  $N_c^2 - 1 = 8$  ;
- $t_{ab}^C$  are  $3 \times 3$  matrices that act as the generators of SU(3);
- $g_s$  is the coupling constant of QCD;

Moreover,  $F_{\mu\nu}^A$  represent the following tensor field:

$$F_{\mu\nu}^A = \partial_\mu \mathfrak{A}_\nu^A - \partial_\nu \mathfrak{A}_\mu^A - g_s f_{ABC} \mathfrak{A}_\mu^B \mathfrak{A}_\nu^C \quad (1.16)$$

where the  $f_{ABC}$  are the structure constants of the group. Quarks and anti-quarks (matter fields) are in the fundamental representation of the SU(3) colour group and in its complex conjugate respectively, which have dimension  $N_c$ , whereas gluons (gauge fields) transform in the adjoint representation of SU(3), which has dimension  $N_c^2 - 1$ . In the following, colour indices will be omitted, and a summation over colour will be assumed in the

gauge-invariant quantities. The Lagrangian thus takes the simpler form:

$$\mathcal{L} = \bar{\psi}_a(i\gamma^\mu(\partial_\mu + ig\mathfrak{A}_\mu) - m)\psi^a. \quad (1.17)$$

If one considers the ideal case of  $N_f$  quarks of equal mass, quarks and antiquarks can be assigned to the  $N_f$ -dimensional representation (and its complex conjugate) of the  $SU(N_f)$  flavour symmetry group. The Lagrangian in eq. (1.17) is invariant under global transformations of the group. Infinitesimal transformation of the fields can be written as:

$$\delta\psi^a = -i\delta\alpha^A(T^A)_b^a\psi^b \quad (1.18)$$

$$\delta\bar{\psi}^a = i\delta\alpha^A\bar{\psi}^b(T^A)_a^b \quad (1.19)$$

By application of Noether's theorem, one finds  $N_f^2 - 1$  conserved currents:

$$\partial^\mu j_\mu^A(x) = -i\frac{\partial\mathcal{L}_q}{\partial(\partial^\mu\psi^a)}(T^A)_b^a\psi^b = \bar{\psi}_a\gamma_\mu(T^A)_b^a\psi^b\partial^\mu j_\mu^A = 0 \quad (1.20)$$

Where  $T^a$  are the  $N_f \times N_f$  hermitian traceless generators of the group:  $[T^A, T^B] = if_{ABC}T^C$  with  $A, B, C = 1, \dots, N_f^2 - 1$ , and  $f_s$  are the structure constants.

This ideal symmetry mode with equal quark masses is called *Wigner-Weyl* mode. In the real world, quarks have different masses. In this case, the Lagrangian density will take the form:

$$\mathcal{L} = \sum_{a=1}^{N_f} \bar{\psi}_a(i\gamma^\mu(\partial_\mu + ig\mathfrak{A}_\mu) - m_a)\psi^a \quad (1.21)$$

In this case, the Lagrangian density's mass term is not invariant under transformations of  $SU(N_f)$ . As illustrated by eq. (1.22), the mass difference between members of the representation multiplet implies the Noether currents are no more conserved:

$$\partial^\mu j_\mu^A = -i \sum_{a,b=1}^{N_f} (m_a - m_b)\bar{\psi}_a(T^A)_b^a\psi^b \neq 0 \quad (1.22)$$

It is possible, anyway, to handle the mass difference effects as perturbative corrections to

the ideal (symmetric) case. The Lagrangian density can then be written as:

$$\mathcal{L} = \mathcal{L}_0 + \Delta\mathcal{L} \quad (1.23)$$

where the former term represents the Lagrangian for equal masses, while the latter is the perturbation introduced by unequal quark masses. Because of the large mass difference between the u, d, s and the c, b, t quarks, an approximate symmetry holds only for the three lightest quarks; the corresponding group is  $SU(3)_f$ .

### 1.3.2 Axial symmetry

Besides the flavour transformations shown in eq. (1.19), fermion fields undergo another type of transformation called *axial flavour*, which changes the parity of fields. It is obtained by including the Dirac  $\gamma^5$  matrix in flavour transformations. Infinitesimal transformations take the form:

$$\delta\psi^a = -i\delta\alpha^A (T^A)_b^a \gamma_5 \psi^b \quad (1.24)$$

$$\delta\bar{\psi}^a = i\delta\alpha^A \bar{\psi}^b \gamma_5 (T^A)_a^b \quad (1.25)$$

The Lagrangian density, however, is in this case not invariant under field transformations.

The term:

$$\delta\mathcal{L} = 2im\delta\alpha^A \bar{\psi}_a (T^A)_b^a \gamma_5 \psi^b \quad (1.26)$$

only vanish for zero quark masses. To summarise:

- the Lagrangian density is invariant under flavour transformations only for equal quark masses;
- the Lagrangian density is invariant under flavour and axial flavour transformations for null quark masses.

### 1.3.3 Chiral symmetry

Flavour and axial flavour transformations together form the group of *chiral transformations*. The conserved currents and charges, defined by integrating the currents over space, are:

$$j_\mu^A(x) = \bar{\psi}_a \gamma_\mu (T^A)_b^a \psi^b \quad (1.27)$$

$$j_{5\mu}^A(x) = \bar{\psi}_a \gamma_\mu \gamma_5 (T^A)_b^a \psi^b \quad (1.28)$$

$$Q^A = \int d^3x j_0^A(x) \quad (1.29)$$

$$Q_5^A = \int d^3x j_{50}^A(x). \quad (1.30)$$

It is possible to combine the flavour and axial flavour charges in the following way:

$$Q_L^A = \frac{1}{2}(Q^A - Q_5^A) \quad Q_R^A = \frac{1}{2}(Q^A + Q_5^A) \quad (1.31)$$

The two new left-handed ( $Q_L$ ) and right-handed ( $Q_R$ ) charges satisfy the commutation relations:

$$[Q_L^A, Q_L^B] = if_{ABC} Q_L^C \quad [Q_R^A, Q_R^B] = if_{ABC} Q_R^C \quad [Q_L^A, Q_R^B] = 0 \quad (1.32)$$

This means that  $Q_L$  and  $Q_R$  act in a decoupled way and generate independent groups of transformations; in other words, the chiral group is decomposed in the group product  $SU(3)_L \otimes SU(3)_R$ , and the flavour group is a subgroup of it.

### 1.3.4 Chiral symmetry realization modes

As quarks are not massless, chiral symmetry is not an exact symmetry in nature; it must therefore be broken. There are two possible realization modes for a broken symmetry:

- Explicit symmetry breaking (Wigner-Weyl): the vacuum state is annihilated by the action of the group generators, and therefore it is symmetric;

- Spontaneous symmetry breaking (Nambu-Goldstone): the vacuum state is not annihilated by the action of the group generators; instead, new massless pseudo-scalar states are produced.

As the action of chiral transformations on hadronic states in flavour multiplets is that of creating an equal state with opposite parity, and thus producing parity doublets, and these are not observed in the hadronic sector, the symmetry breaking cannot happen solely in Wigner-Weyl mode. Instead, it happens via a combination of the above two realizations: the flavour part of chiral symmetry undergoes explicit symmetry breaking, whereas the axial flavour part undergoes spontaneous symmetry breaking, with the associate production of eight pseudo-scalar massless mesons (Nambu-Goldstone bosons). Because quarks are massive, the chiral group then undergoes an additional explicit symmetry breaking; in this way, members of the pseudo-scalar octet acquires a small mass. These can be identified with the  $\pi^+$ ,  $\pi^-$ ,  $\pi^0$ ,  $\eta$ ,  $K^+$ ,  $K^0$ ,  $K^-$  and  $\bar{K}^0$  mesons.

### 1.3.5 Effective field theories

Effective field theories are approximations of more fundamental theories, valid at a sub-range of energies of the latter [44]. The only degrees of freedom used in the theory are states with masses smaller than the energy scale of the exact theory, whose interactions are organised in an expansion of powers of the ratio  $E/\Lambda$ . Heavier particles are integrated out and encoded in so-called *low energy coefficients* (LECs), that are the couplings of the resulting Lagrangian of the approximate theory. At increasingly higher order (or energies) in the expansion, new degrees of freedom need to be taken into account, and thus new LECs are produced. As, on the other hand, one lowers the energy, some of the degrees of freedom are frozen out. Effective field theories are specified by an infinite number of terms; however, if one considers a specific order in the energy expansion, the theory is specified by a finite number of LECs and it is renormalizable at that order.

The effective field theory must contain all the terms predicted by the symmetries of

the underlying fundamental theory. In the case of ChPT, this is Chiral Symmetry.

There are two types of effective field theories:

- *decoupling* theories: the Lagrangian of this theory can be written down as the sum of renormalizable and non-renormalizable terms; heavy particles of the fundamental theory do not need to be taken into account by the low-energy effective theory;
- *non-decoupling* theories: the light particles of the effective theory are generated through spontaneous symmetry breaking. It is not possible to decouple the heavy particles from the light particles, and the Lagrangian of the theory is non-renormalisable.

ChPT, the low-energy ( $E \ll 1 \text{ GeV}$ ) realisation of the SM in the hadronic sector, is an example of the latter type.

### 1.3.6 ChPT

Kaon decays proceed via an interplay of weak, electromagnetic and intrinsically low-energy (long-distance) strong interactions; the main challenge in theoretical kaon physics is related to the non-perturbative nature of QCD at this regime, with the growing running QCD coupling and asymptotic freedom. This makes it a non-trivial task to derive hadronic interactions from the fundamental QCD Lagrangian. In ChPT, an effective field theory defined by a chiral hadronic Lagrangian, the highly complex QCD structure is translated, at low energies, into an elegant and simpler form exploiting the theory's symmetry properties. [45]

In ChPT the degrees of freedom are not quarks and leptons, but low-mass hadrons; decay amplitudes are expanded in terms of meson masses and momenta. Contributions from high-mass particles are integrated out of the Lagrangian and enclosed in coupling constants called *low energy constants* or LECs. The more complete the knowledge of LECs, the more precise theoretical predictions are achievable. At energies below the mass of the  $\rho$  resonance, the only hadrons are those making up the light pseudo-scalar octet ( $\pi$ ,  $K$ ,  $\eta$ ). These can be approximated as the massless Goldstone bosons produced in

the spontaneous breaking of chiral symmetry, and constitute the dynamical degrees of freedom of the theory. ChPT is therefore based on both an expansion in small momenta  $p$ , being a low energy effective field theory, and an expansion in quark masses  $m_q$  around the chiral limit. The most general form of a ChPT Lagrangian is the following:

$$\mathfrak{L}_{eff} = \sum_{i,j} \mathfrak{L}_{ij} \quad \mathfrak{L}_{ij} = O(p^i m_q^j) \quad (1.33)$$

The two expansions are connected by expressing the mass of the pseudo-scalar mesons in terms of quark masses.

As mentioned previously, at any given order, ChPT is renormalisable. The Lagrangian density is specified by a finite set of LECs; in order to be able to make ChPT predictions at that order, the LECs must be determined experimentally. If one considers an extended QCD Lagrangian with quarks coupling to external vector, axial, scalar and pseudoscalar fields  $v_\mu$ ,  $a_\mu$ ,  $s$  and  $p$ , taking the form:

$$\mathfrak{L}_{QCD} = \mathfrak{L}_{QCD}^0 + \bar{q}\gamma^\mu(v_\mu + \gamma_5 a_\mu)q - \bar{q}(s - i\gamma_5 p)q \quad (1.34)$$

At the lowest order,  $O(p^2)$ , the locally chiral invariant Lagrangian density that described the strong, electromagnetic and semileptonic weak interactions of mesons can be written as [46]:

$$\mathfrak{L}_2 = \frac{F^2}{4} \langle D_\mu U D^\mu U^\dagger + \chi U^\dagger + \chi^\dagger U \rangle \quad (1.35)$$

Where  $U$  is the pseudoscalar meson fields matrix,  $D_\mu$  is the covariant derivative  $D_\mu U = \partial_\mu U - ir_\mu U + iUl_\mu$ ,  $r_\mu = v_\mu + a_\mu$ ,  $l_\mu = v_\mu - a_\mu$ ,  $\chi = 2B(s + ip)$ , and the two remaining LECs,  $F$  and  $B$ , are determined from experimental measurements of the pion decay constant  $F_\pi$  and the quark condensate in the chiral limit:

$$F_\pi = F[1 + O(m_q)] \quad (1.36)$$

$$\langle 0 | \bar{u}u | 0 \rangle = -F^2 B[1 + O(m_q)] \quad (1.37)$$

It is in this scenario, a measurement of the BR of  $K^+ \rightarrow \pi^+\gamma\gamma$ , described in the next subsection, is an important tool to gain new knowledge on ChPT parameters and increase the predictive power of the theory.

### 1.3.7 The $K^+ \rightarrow \pi^+\gamma\gamma$ decay

By indicating the kaon four-momentum as  $k$  and the pion and photon four-momenta as  $p$ ,  $q_1$  and  $q_2$  respectively, the  $K^+ \rightarrow \pi^+\gamma\gamma$  decay is described in terms of the kinematic variables:

$$z = \frac{(q_1 + q_2)^2}{M_K^2} \quad (1.38)$$

$$y = \frac{k \cdot (q_1 - q_2)}{M_K^2} \quad (1.39)$$

The  $z$  variable represents the square of the final-state photons invariant mass, normalised to the squared mass of the kaon, and is a measure of collinearity of the two photons; in case of two photons coming from a  $\pi^0$  decay, it takes the value  $r^2$ , with  $r_\pi = m_\pi/m_K$ . The  $y$  variable is the product of the four-momentum of the kaon and the difference between the two photons four-momenta normalised to the squared kaon mass, and it yields information about the angle formed by the pion and the photon pair. The decay amplitudes generating the process are due, in the ChPT description, to meson loops; in order to render the Lagrangian renormalisable at each perturbative order, one must subtract *counterterms*, corresponding to additional Feynman diagrams, that absorb loop divergences. The double differential decay rate of  $K^+ \rightarrow \pi^+\gamma\gamma$  with respect to  $y$  and  $z$  contains four decay amplitudes A, B, C, D, and is given by:

$$\frac{d^2\Gamma}{dydz} = \frac{M_K}{2^9\pi^3} \left\{ z^2(|A+B|^2 + |C|^2) + \left[ y^2 - \frac{1}{4}\lambda(1, r_\pi^2, z) \right]^2 (|B|^2 + |D|^2) \right\} \quad (1.40)$$

. The physical regions for  $y$  and  $z$  are:

$$0 \leq |y| \leq \lambda^{1/2}(1, r_\pi^2, z)/2 \quad (1.41)$$

$$0 \leq z \leq (1 - r_\pi)^2 \quad (1.42)$$

where  $\lambda(a, b, c) = a^2 + b^2 + c^2 - 2(ab + ac + bc)$ .

### Contributions at $O(p^4)$

The double differential decay rate has no contributions at tree level ( $O(p^2)$ ); at the first non-null order,  $O(p^4)$ , the B and D amplitudes are still zero. The leading contribution at this order comes from the A amplitude; a smaller contribution comes from the pole amplitude C. B and D arise at order  $O(p^6)$ ; these two amplitudes are responsible for the distribution of  $z$  at low relative angles between the photons. At  $O(p^4)$ , A can be expressed as:

$$A^{(4)}(z) = \frac{G_8 M_K^2 \alpha_{em}}{2\pi z} [(z + 1 - r_\pi^2)F(z/r_\pi^2) + (z - 1 + r_\pi^2)F(z) - \hat{c}z] \quad (1.43)$$

where  $F(z)$  is defined as follows:

$$F_z = \begin{cases} 1 - \frac{4}{z} \arcsin^2\left(\frac{\sqrt{z}}{2}\right) & z \leq 4 \\ 1 + \frac{1}{z} \left( \ln \frac{1 - \sqrt{(1-4/z)}}{1 + \sqrt{(1-4/z)}} + i\pi \right)^2 & z > 4 \end{cases} \quad (1.44)$$

The terms  $(z + 1 - r_\pi^2)F(z/r_\pi^2)$  and  $(z - 1 + r_\pi^2)F(z)$  in eq. (1.43) represent a pion and a kaon loop contribution respectively. By considering the behaviour of  $F(z)$ , one finds that the pion loop amplitude dominates over the kaon loop amplitude. The last contribution to A in eq. (1.43) is a local counterterm-generated contribution expressed in terms of the  $\hat{c}$  parameter, which is related to ChPT LECs via the expression:

$$\hat{c} = 128\pi^2 [3(L_9 + L_{10}) + N_{14} - N_{15} - 2N_{18}]/3 \quad (1.45)$$

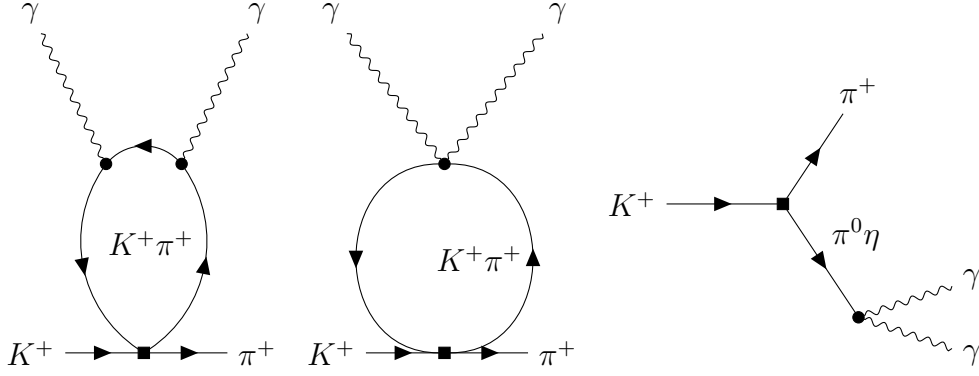


Figure 1.8: Feynman diagrams contributing to the A amplitude (left and center) and pole amplitude C (right) for the  $K^+ \rightarrow \pi^+ \gamma \gamma$  decay. [49]

Where the  $L_9$  and  $L_{10}$  factors are strong couplings, and the  $N_{14}$ ,  $N_{15}$  and  $N_{18}$  factor are weak couplings at  $O(p^4)$ ; all the factors are model-dependent. Certain models, such as the Weak Deformation Model (WDM), predict  $\hat{c} = 0$ , while others predict for it non-zero values, as is the case for the Factorisation Model (FM) predicting  $\hat{c} = -2.3$  [47, 48]. It is worth noting that at this order A, the dominant amplitude at  $O(p^4)$ , only depends on  $y$ ,  $z$  and on  $\hat{c}$ .

At the same order, the C amplitude, which is generated via the chain  $K^+ \rightarrow \pi^+(\pi^0, \eta) \rightarrow \pi^+ \gamma \gamma$ , can be written as:

$$C^{(4)}(z) = \frac{G_8 M_K^2 \alpha_{em}}{\pi} \left[ \frac{z - r_\pi^2}{z - r_\pi^2 + i r_\pi} \frac{\Gamma_{\pi^0} m_K}{-} \frac{z - \frac{2+r_\pi^2}{3}}{z - r_\eta^2} \right] \quad (1.46)$$

with  $r_\eta = m_\eta/m_K$  and  $\Gamma_{\pi^0} \rightarrow \gamma\gamma$ ) The kaon and pion loop contributions to the amplitude A, and the pole contribution C, are shown in fig. 1.8. The fact that at  $O(p^4)$  the leading amplitude A is written in terms of the single ChPT parameter  $\hat{c}$  implies that, by measuring the  $K^+ \rightarrow \pi^+ \gamma \gamma$  decay, one can constrain  $\hat{c}$ . The value of  $\hat{c}$  affects both the BR and the kinematic variables distributions. The way the  $z$  variable is influenced by the value of the  $\hat{c}$  parameter is illustrated in fig. 1.9 for the orders  $O(p^4)$  and  $O(p^6)$ .

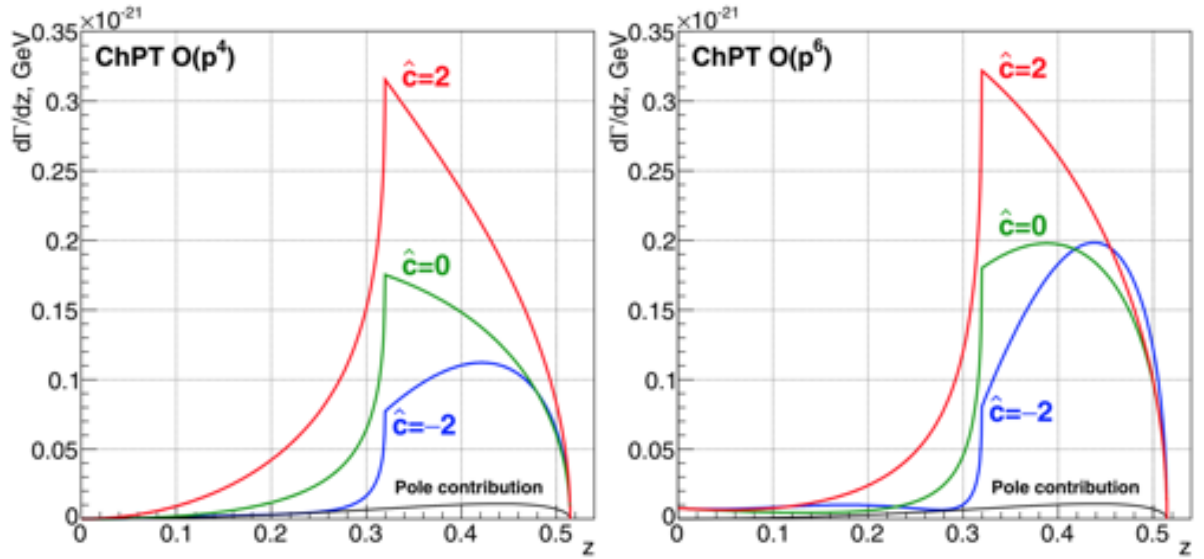


Figure 1.9: Differential decay rate in the kinematic variable  $z$  for  $K^+ \rightarrow \pi^+\gamma\gamma$  at the orders  $O(p^4)$  (left-hand side) and  $O(p^6)$  (left-hand side) for different values of the ChPT parameter  $\hat{c}$ . The amplitude  $A$  is the leading contributor at  $O(p^4)$ ; at  $O(p^6)$  the amplitudes  $B$  and  $D$ , responsible for the low  $z$  component, contribute as well. [50, 51]

### Contributions at $O(p^6)$

At order  $O(p^6)$  a complete theoretical description is not yet available. The main contributions have, however, been estimated. They are:

- Unitarity corrections from  $K^+ \rightarrow \pi^+\pi^+\pi^-$ , contributing to both  $A(z, y)$  and  $B(z)$  [50];
- Local non-resonant contributions, shown to be small by chiral dimensional estimates;
- Vector-resonance contributions, proceeding via strong resonance exchange with a weak transition in the external legs;
- Vector-resonance contributions, proceeding via strong resonance exchange between a direct weak vector-pseudoscalar-photon ( $VP\gamma$ ) vertex.

The latter contribution is model-dependent; however, the combination of the two vector-resonance contributions is predicted to be small across various models, leading to conclude that the unitarity corrections are the dominant contribution at  $O(p^6)$ . It follows that the

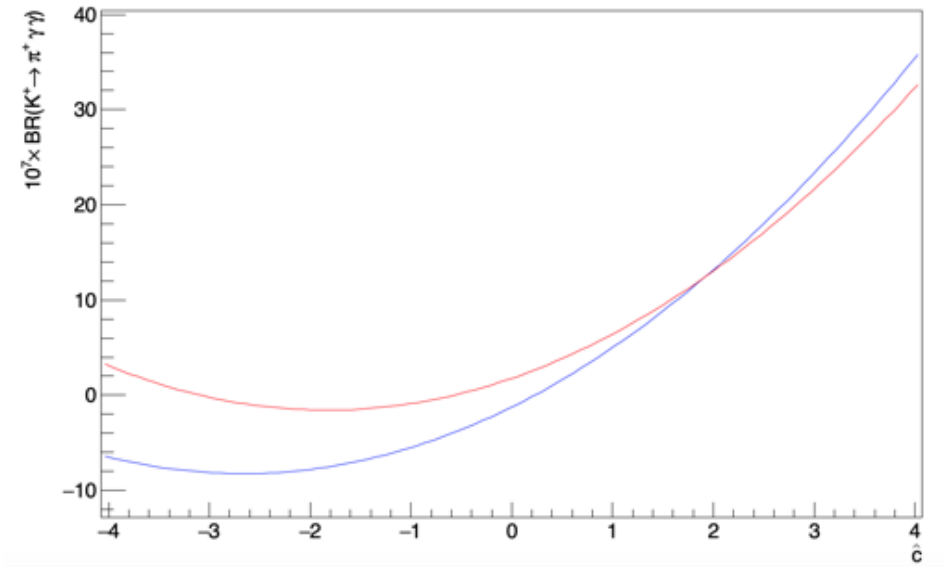


Figure 1.10:  $K^+ \rightarrow \pi^+ \gamma \gamma$  BR as a function of the parameter  $\hat{c}$ , related to ChPT LECs, at the  $O(p^4)$  (blue line) and  $O(p^6)$  (red line) order [50].

small values of  $z$ , which is non-null from the  $O(p^6)$ , which yields the leading contribution, can be estimated in a model-independent way.

### Theoretical estimate of the total BR

Estimates of the total BR of the  $K^+ \rightarrow \pi^+ \gamma \gamma$  decay depend on the value of the  $\hat{c}$  parameter appearing in the dominant  $O(p^4)$  amplitude  $A$  in eq. (1.43). As the latter is model-dependent, experimental measurements will allow to discriminate between different models. The WDM and FM models, where  $\hat{c} = 0$  and  $\hat{c} = -2.3$  respectively, predict:

$$BR(K^+ \rightarrow \pi^+ \gamma \gamma)|_{WDM} = 7.24 \times 10^{-7} \quad (1.47)$$

$$BR(K^+ \rightarrow \pi^+ \gamma \gamma)|_{FM} = 6.20 \times 10^{-7} \quad (1.48)$$

The variation of the total BR as a function of the  $\hat{c}$  parameter is shown in fig. 1.10 at the  $O(p^4)$  and  $O(p^6)$  orders [50].

The uncertainty due to the value of  $\hat{c}$  also contributes to a variation in the spectra shown in fig. 1.9 for the distribution of the kinematic  $z$  variable.

## Experimental status

The most recent measurement of the BR of the  $K^+ \rightarrow \pi^+\gamma\gamma$  decay comes from a combined analysis from the NA48/2 and NA62/2007 experiments at CERN. A challenging aspect at both experiments is related to the fact that the analysis could not be performed on the main trigger lines. Given the very similar signature of  $K^+ \rightarrow \pi^+\pi^0$  and its large BR, a dedicated trigger line for  $K^+ \rightarrow \pi^+\gamma\gamma$  would mainly select  $K^+ \rightarrow \pi^+\pi^0$  events, occupying a large fraction of the available bandwidth. A dedicated trigger line is therefore unfeasible; the analysis can, however, be performed on minimum bias samples. Signal and normalisation channels were collected with the same trigger chains, which implies that trigger inefficiencies cancelled out at first order. At NA48/2, the sample was collected with simultaneous 60 GeV/ $c$   $K^+$  and  $K^-$  beams and trigger condition requirements related to the presence of a charged track and calorimetric energy depositions. The total number of kaon decays in fiducial volume (FV) is  $0.93 \times 10^9$  and 149 decay candidates were found, with an estimated background contribution of  $15.5 \pm 0.7$ . At NA62/2007, data from single and simultaneous  $K^+$  and  $K^-$  beams at 74 GeV/ $c$  was collected via five downscaled control trigger chains. The total number of kaon decays in FV is  $1.51 \times 10^9$ , and 232 decay candidates were found, with an estimated background contribution of  $17.4 \pm 1.1$ .

The reported combined model-independent branching ratio in the  $z > 0.2$  kinematic range is [51]:

$$BR_{MI}(K^+ \rightarrow \pi^+\gamma\gamma, z > 0.2) = (0.965 \pm 0.063) \times 10^{-6}. \quad (1.49)$$

At NA62, large data-sets allow a measurement with world-leading precision. A measurement of the BR of  $K^+ \rightarrow \pi^+\gamma\gamma$  with NA62 data, my PhD's analysis project, is described in chapter 5.

## CHAPTER 2

# THE NA62 EXPERIMENT

NA62 is a fixed target experiment located in the CERN North Area and designed with the main goal of measuring the branching ratio (BR) of the ultra-rare decay of a positively charged kaon into a positively charged pion and a neutrino-antineutrino pair [52], one of the golden channels in kaon physics, discussed in chapter 1. The BR of this decay is known with little theoretical uncertainty:  $BR(K^+ \rightarrow \pi^+ \nu \bar{\nu}) = (0.84 \pm 0.10) \times 10^{-10}$ . NA62 aims at performing a measurement of this decay matching the precision of the current theoretical predictions. The redundant system of sub-detectors, and the flexible trigger system described in chapter 3, allow, furthermore, for a broad range of rare kaon decays studies, including the measurement of the rare decay  $K^+ \rightarrow \pi^+ \gamma \gamma$ , my main PhD project. The experimental strategy and the setup of NA62 will be described in the present chapter, where the motivation behind the large number of high-efficiency sub-detectors will be discussed relatively to the measurement of the main experimental goal; the sub-systems involved in the analysis of the  $K^+ \rightarrow \pi^+ \gamma \gamma$  will be described in more detail.

### 2.1 The experimental strategy

To perform a high-precision measurement of the  $K^+ \rightarrow \pi^+ \nu \bar{\nu}$  decay, NA62 uses a novel experimental technique, which is based on a beam of high-momentum kaons decaying in-flight in the detector. The experimental signature of the decay consists of a kaon track

Decay mode	BR
$K^+ \rightarrow \pi^+ \nu_\mu$	$(63.55 \pm 0.11)\%$
$K^+ \rightarrow \pi^+ \pi^0$	$(20.66 \pm 0.08)\%$
$K^+ \rightarrow \pi^+ \pi^+ \pi^-$	$(5.59 \pm 0.04)\%$
$K^+ \rightarrow \pi^0 e^+ \nu_e$	$(5.07 \pm 0.04)\%$
$K^+ \rightarrow \pi^0 \mu^+ \nu_\mu$	$(3.353 \pm 0.034)\%$
$K^+ \rightarrow \pi^+ \pi^0 \pi^0$	$(1.761 \pm 0.022)\%$

Table 2.1: Main  $K^+$  decay modes.

matched to a single charged pion track, and no extra in-time activity. The smallness of the BR in the SM scenario dictates the need for a high flux of particles. In order to collect a sample of  $\approx 100$  signal events, with a SM BR of the order of  $10^{-10}$  and assuming a detector acceptance of 10%, one must collect a total sample of  $10^{13}$  kaon decays. This can be achieved with a few years of data-taking and a beam particle rate downstream of the target of  $\approx 750$  MHz, with 6% kaons. It follows that excellent time resolution, at the order of 100 ps, is required for the most critical sub-detectors, such as the ones performing particle identification, the ones involved in triggering, and the beam spectrometer. In order to match the theoretical precision on the BR, a background rejection factor of the order of  $10^{12}$  against the main  $K^+$  decay modes, listed in table 2.1, must be achieved.

As the dominant decay modes, such as  $K^+ \rightarrow \pi^+ \pi^0$  and  $K^+ \rightarrow \mu^+ \nu_\mu$ , have an experimental signature very similar to that of the signal, the necessary level of rejection is performed via a mixed approach:

- at kinematic level, through the squared missing mass variable  $m_{miss}^2 = (P_K - P_\pi)^2$  illustrated in fig. 2.1, where  $P_K$  and  $P_\pi$  are, respectively, the 4-momenta of the kaon and the charged decay product, assumed to be a pion - this allows a background rejection factor of  $10^4$ . Reaching this level of kinematic rejection requires a highly efficient low-mass tracking system with excellent time resolution;
- with hermetic and high-efficiency veto systems for photons and muons, a further rejection factor of  $10^8$  must be achieved.

Further to other kaon decays, another type of background for the measurement of

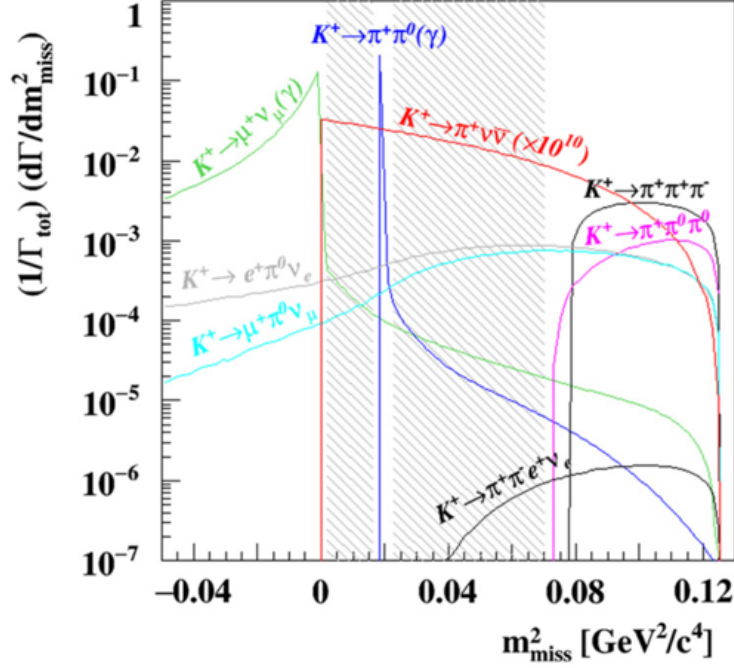


Figure 2.1: Squared missing mass distribution, under the  $\pi^+$  mass hypothesis, for  $K^+ \rightarrow \pi^+ \nu \bar{\nu}$  and the main  $K^+$  decay channels. Two signal regions are defined on the left and on the right of the  $K^+ \rightarrow \pi^+ \pi^0$  peak. The signal, shown in red, is multiplied by  $10^{10}$  for visibility purposes. [5]

$K^+ \rightarrow \pi^+ \nu \bar{\nu}$  exists: the *upstream background*, related to the production of  $\pi^+$  from  $K^+$  or  $\pi^+$  decays occurring in the beam spectrometer, or interactions of beam particles in the spectrometer's material, matched to an accidental kaon. This background is reduced with the aid of veto systems for charged particles, precise association of the  $K^+$  and the  $\pi^+$  tracks, and kinematic cuts on the extrapolation of the pion track to the fiducial region.

The experimental setup of NA62 is illustrated in fig. 2.5. The beryllium target is located, in the scheme, at the origin of the longitudinal axis ( $z$ ); the first (*upstream*) sub-detectors identify (CEDAR/KTAG) and measure the momentum and direction of kaons in the secondary beam (GTK), and veto inelastic background (CHANTI). Decays of the kaons happen in a fiducial volume (FV) located between  $\approx 100$  and  $180$  m from the target. The downstream sub-detectors study the products of these decays. They include:

- a spectrometer for the decay products (STRAW);
- a photon veto system composed of:

- a sub-detector composed of multiple stations at large angles with respect to the decay vertices in the FV (LAV);
- an electromagnetic calorimeter also used to perform particle identification (LKr);
- two intermediate and small-angle photon veto sub-detectors (IRC and SAC);
- a RICH for  $\pi/\mu$  separation;
- two hodoscopes for charged tracks (CHOD and NA48 CHOD) for triggering and timing;
- two hadronic calorimeters (MUV1/2);
- a muon veto system (MUV3);
- two additional sub-detectors to reduce background due to multi-track decays (MUV0 and HASC).

In order to minimise beam scattering and interactions, the GTK and the decay products sub-detectors are placed in vacuum.

## 2.2 The NA62 beam

NA62 uses a beam of protons of 400 GeV/c momentum coming from the CERN Super-Proton-Synchrotron (SPS). The primary beam impinges on the NA62 target, T10 in the CERN numbering scheme, to produce a secondary beam. T10 consists of a rod of beryllium of 400 mm length and 2 mm diameter. The momenta of particles in the secondary beam, which is produced downstream of T10 and indicated as K12, have been chosen to have mean value 75 GeV/c in order to maximise the kaon component. The latter makes up  $\approx 6\%$  of the particles in K12, the rest being composed of pions and protons. The beam has a momentum bite  $\frac{\Delta p}{p} \approx 1\%$ . The layout of the K12 beamline and

its optical elements upstream of the decay region in the horizontal ( $x$ - $z$ ) and vertical ( $y$ - $z$ ) planes can be found in fig. 2.3. The optical elements and the beam's trajectory in the downstream detectors are shown, instead, in fig. 2.4. The functions of the main optical elements are explained in the following list:

- Three quadrupole magnets (Q1, Q2 and Q3) define the beam's solid angle acceptance at 75 GeV/ $c$ ;
- A pair of magnets deflect the beam downwards in the vertical direction; they are followed by two more magnets that return the beam to its original direction (A1). This particular magnet configuration is indicated as an *achromat*. Between the two pairs of magnets, two motorised beam-dump units, TAX1 and TAX2, absorb the protons and other undesired particles, and select the desired momentum component by means of a set of graduated holes;
- A radiator, between TAX1 and TAX2, causes energy loss by Bremsstrahlung for positrons in order to facilitate their subsequent rejection;
- Three quadrupole magnets (Q4, Q5 and Q6) make the beam parallel to the longitudinal axis in the horizontal plane, and refocus it in the vertical plane. At the same time, its acceptance is redefined by the C1 and C2 collimators;
- A further collimator, C3, redefines the beam in the vertical plane and absorbs the positrons previously degraded by the radiator;
- The dipole magnet B3 sweeps away the halo of muons surrounding the beam, as the latter passes through a bore in iron plates placed between the magnet poles. Two steering dipoles, TRIM2 and TRIM3, cancel the effect of the small stray-field inside the hole;
- Two quadrupole magnets (Q7 and Q8) render the beam parallel to the longitudinal axis in both planes to prepare it for passage in the CEDAR/KTAG sub-detector, whereas particles in the beam tails are absorbed by two *cleaning* collimators;

- Two weakly-focusing quadrupoles (Q9 and Q10) prepare the beam for the momentum and direction measurements performed by the GTK sub-detector, described later in this chapter. The GTK uses a second achromat (A2), consisting in two pairs of magnets and a magnetized iron collimator (SCR1), to perform momentum measurements of beam particles and to defocus and disperse the muon component. Two cleaning collimators, C6 and C7, located right before the third GTK station, are used to reject background outside the acceptance of the beam;
- At the exit of the third GTK station, a horizontal steering magnet, TRIM5, gives the beam a momentum kick to produce a deflection of 1.2 mrad in the positive  $x$  direction. Such deflection is given so that, when combined with the one produced by the decay products spectrometer's magnet, it causes the beam to enter the LKr calorimeter central hole.

The FV is located at  $\approx 100$  m downstream of the target, in a 117 m long vacuum tank that also contains the decay products spectrometer ((for more details see chapter 5)) and 11 out of the 12 large angle veto (LAV) stations. At its far end, the vacuum tank is sealed by a thin aluminium window, that separates it from the neon gas of the RICH sub-detector. At the center of the window, a circular opening of 168 mm radius is attached to an aluminium tube to transport in vacuum the undecayed beam.

Downstream of the fiducial volume, the following optical elements can be found:

- Between the second and third station of the STRAW spectrometer, a large aperture dipole magnet, MNP33, gives particles a momentum kick of 270 MeV/ $c$  in the positive  $x$  direction, thus producing a beam deflection of  $-3.6$  mrad. The beam passes through the RICH with this angle. The sub-detector, which has a length of 17 m, is, therefore, rotated to be parallel to the beam. The beam crosses the X axis again 2.8 m after the center of the LKr calorimeter;
- A dipole magnet, BEND, gives one last kick to the beam near the muon veto detector (MUV3), so that it does not intercept the small angle calorimeter (SAC), the last

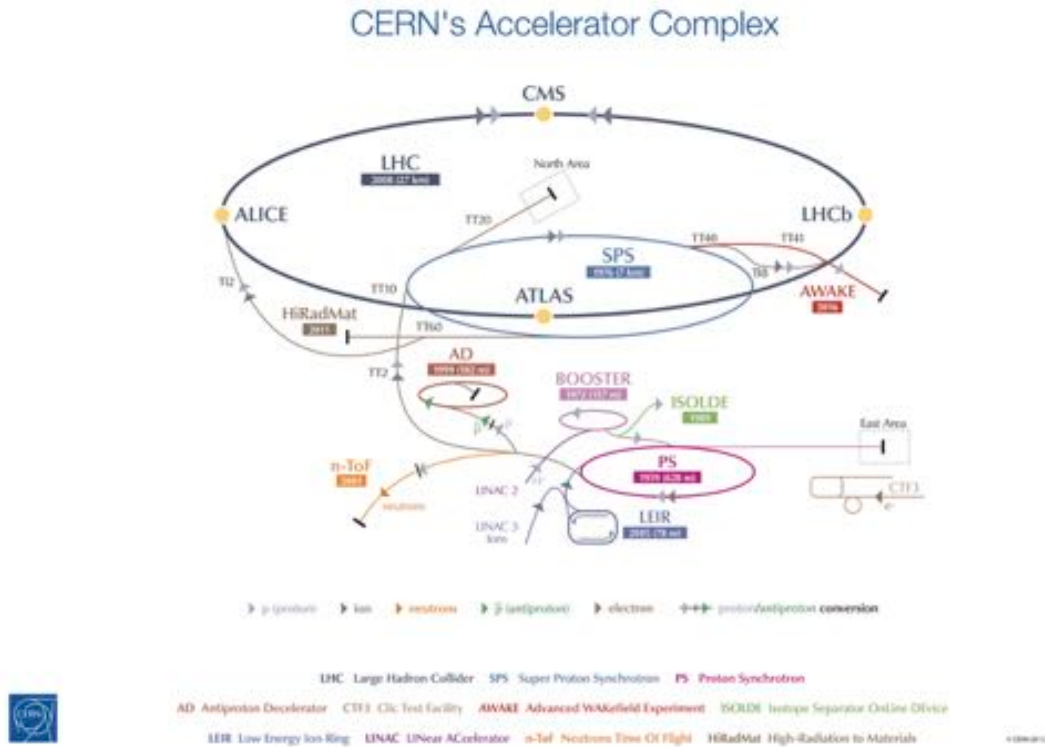


Figure 2.2: The CERN accelerator complex. Part of the beam from the SPS is sent to the North Area, where it is used by fixed target experiments such as NA62. [53]

sub-detector in the setup;

- Finally, a beam dump made of concrete with an iron core absorbs the residual beam.

## 2.3 The NA62 detector

In this section, the NA62 detector will be described; particular emphasis will be placed on the sub-systems playing a role in the analysis of the  $K^+ \rightarrow \pi^+ \gamma \gamma$  decay.

### 2.3.1 The CEDAR/KTAG

A CERN Differential Cherenkov Counter with Achromat Ring Focus (CEDAR), coupled to a photon detection and read-out system specifically designed for NA62, forms the experiment's kaon tagging system, which has the task of identifying kaons in the unseparated

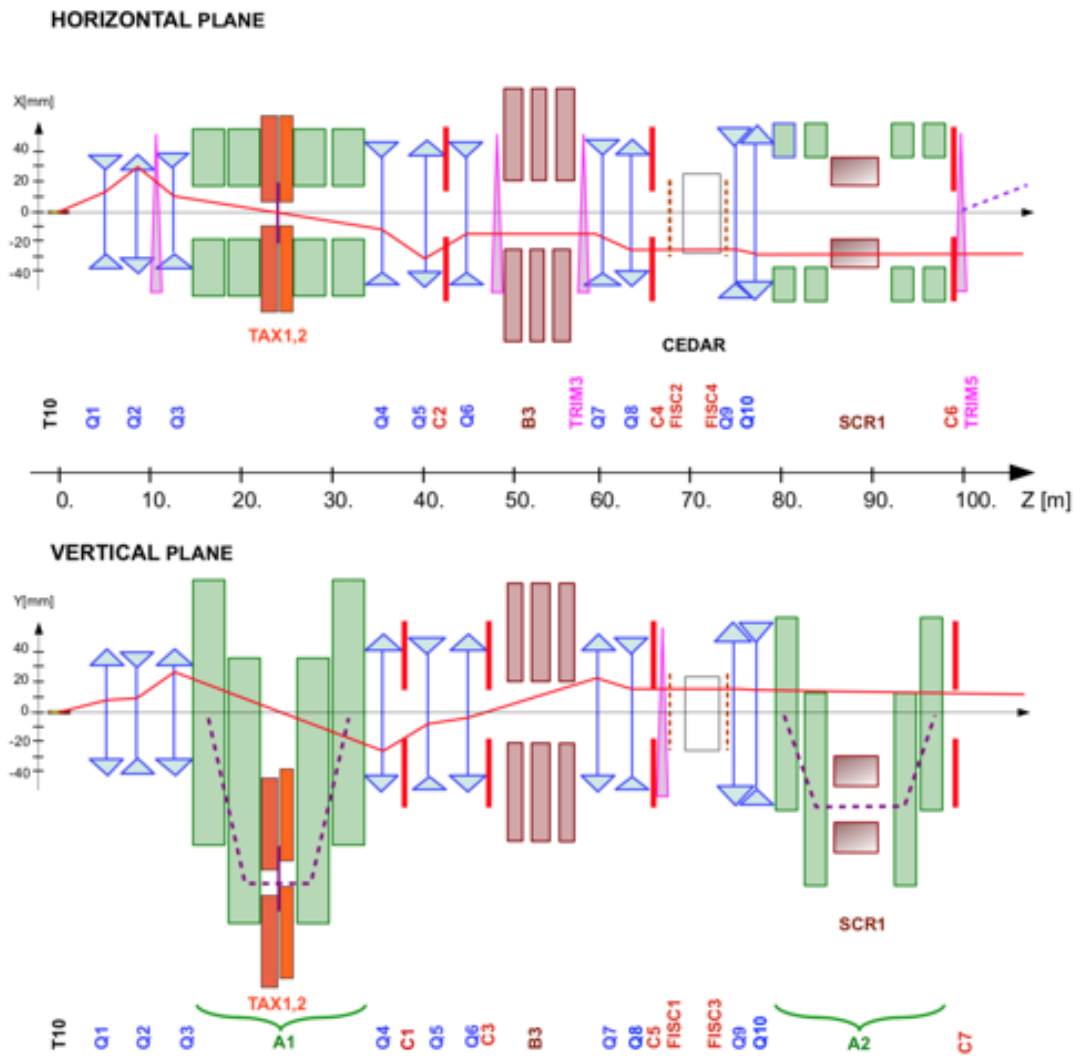


Figure 2.3: Layout, in the horizontal ( $x$ - $z$ ) and vertical ( $y$ - $z$ ) planes, of the secondary beamline (K12) and the optical elements used to perform momentum selection, focusing, cleaning and steering, from the T10 target to the end of the upstream region. [52]

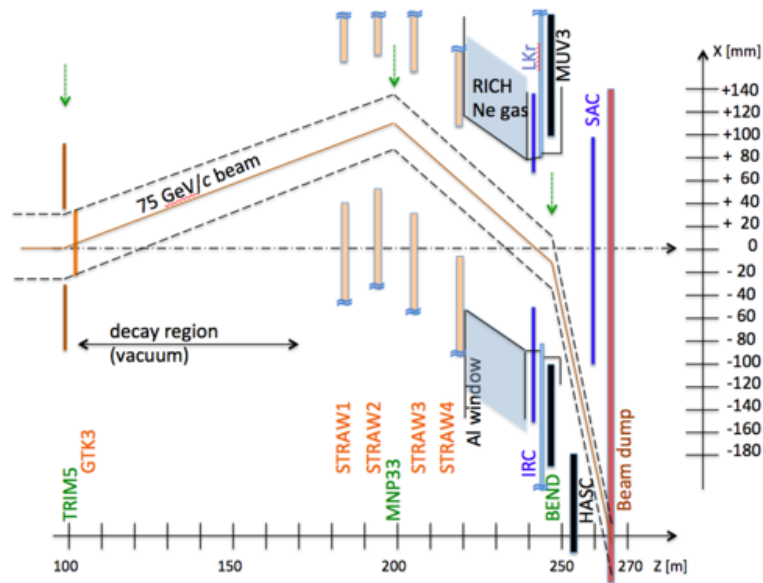


Figure 2.4: Layout, in the horizontal ( $x$ - $z$ ) plane, of the secondary beamline (K12) and the optical elements used for steering in the downstream region. [52]

secondary beam. There are 6% kaons in the 750 MHz secondary beam, making up a 45 MHz rate on the CEDAR/KTAG. The sub-detector, for which I carried out performance studies and routine operations, is used in the high-level trigger for the samples I used in my analysis of the  $K^+ \rightarrow \pi^+ \gamma \gamma$  decay (described in chapter 5). Its time resolution is of the order of 70 ps, its design kaon detection efficiency is 95% for light hitting at least six sectors, and the mis-tagging rate for pions is of the order  $10^{-4}$ . The sub-system is described in detail in chapter 4.

### 2.3.2 The GTK

The GigaTracker (GTK) is a spectrometer located in vacuum upstream of the decay region at  $\approx 80$  to 100 m from the target. The sub-detector measures momentum, direction and time of beam kaons, and it is composed of three stations of silicon pixel detectors with an achromat consisting of a pair of dipole magnets between each two GTK stations.

Each GTK station consists of a matrix of  $200 \times 90$  silicon pixels having an area of  $300 \times 300 \mu\text{m}^2$  and a thickness of  $200 \mu\text{m}$  and read-out by application-specific integrated circuits (ASICs), each corresponding to  $40 \times 45$  pixels. A picture of the sensor side of

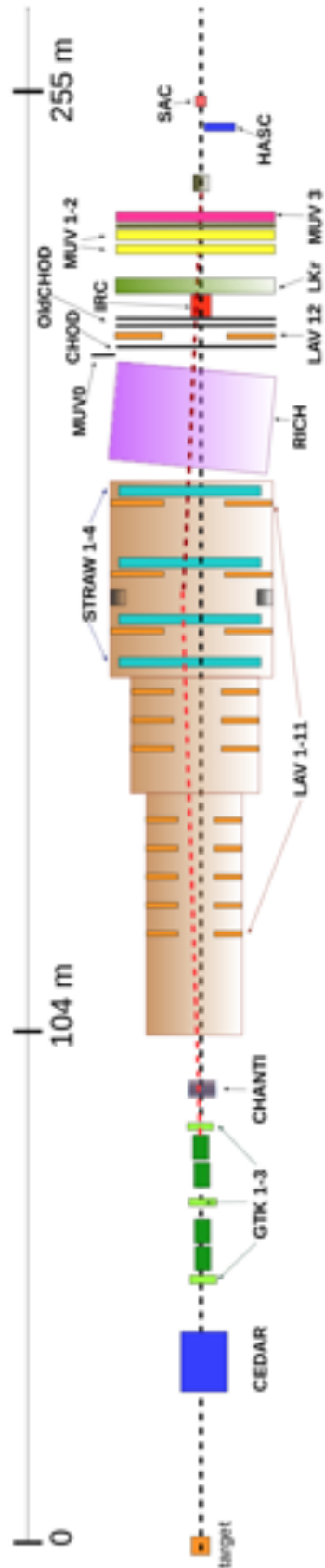


Figure 2.5: Schematic view of the NA62 detector in the horizontal plane  $x-z$

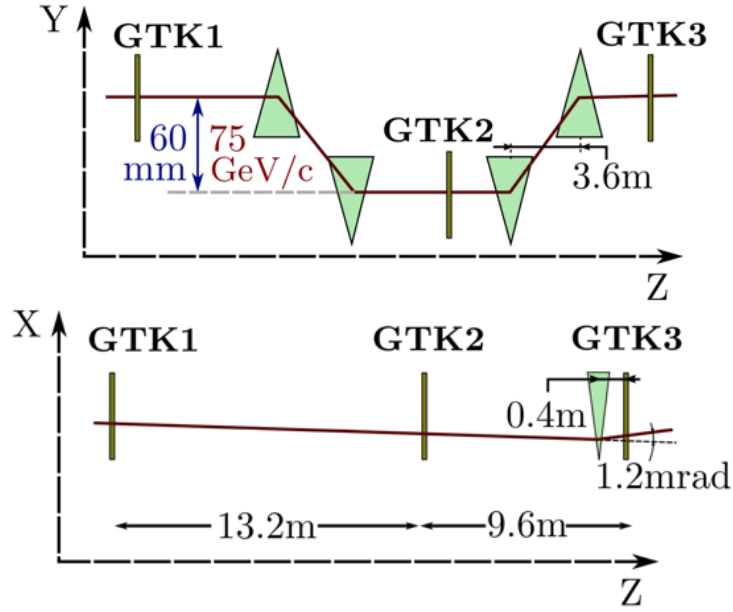


Figure 2.6: Vertical (top) and horizontal (bottom) arrangement of the GTK stations. The triangle-shaped objects in the top scheme represent the four magnets composing the achromat A2, used for momentum measurement and muon defocusing.

a GTK station can be found in fig. 2.6. The pixel size was chosen in order to ensure a momentum resolution of 0.2%. The sub-detector's resolution on the directions  $dx/dz$  and  $dy/dz$  is  $16 \mu\text{rad}$  and its time resolution is in the range 150 - 225 ps depending on how many pixels per station are used in the estimate of time.

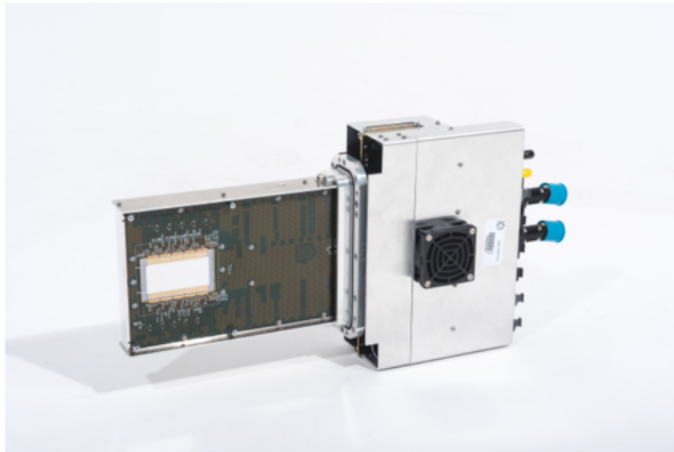


Figure 2.7: Sensor-side view of an assembled GTK station.

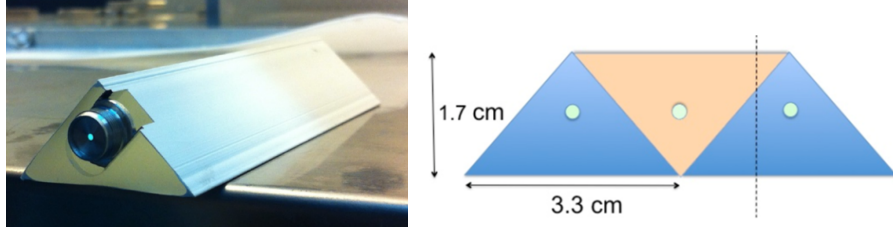


Figure 2.8: One of the triangular-based scintillator bars employed by the CHANTI sub-detector (left); arrangement of the bars to form a station (right).

### 2.3.3 The CHANTI

The CHANTI sub-detector is located 28 mm downstream of and in the same vacuum region as the GTK and it acts as a veto against charged tracks produced in inelastic interactions in the third GTK station, as well as beam halo muons and charged particles produced before GTK3. It consists of six squared-section stations made of triangular cross-section scintillator bars. The stations have an area of  $300 \times 300 \text{ mm}^2$  and have a central  $95 \times 96 \text{ mm}^2$  hole for the passage of the beam. Each station is composed of two planes of 48 bars each; in the two planes (X and Y view), bars are arranged in an orthogonal way, in order to get more precise information on the particle's crossing position. The arrangement of bars in each view is illustrated in fig. 2.8 together with a single scintillator bar, whereas a fully assembled station can be seen in fig. 2.9. Fast wavelength-shifting (WS) optic fibres couple the scintillator bars to silicon photomultipliers (SiPM). The dimensions and position of CHANTI allow an angular coverage for particles produced in GTK3 between 49 mrad and 1.34 rad.

### 2.3.4 The STRAW

The STRAW sub-detector is the downstream spectrometer. It is located at  $\approx 180 \text{ m}$  from the target and it measures the momentum and direction of the charged decay products of kaon decays. The spectrometer, housed in the vacuum tank in order to minimise multiple scattering, consists of four chambers distributed across a 35 m long region along the beam-line. A dipole magnet, MNP33, is located between the second and third STRAW chambers

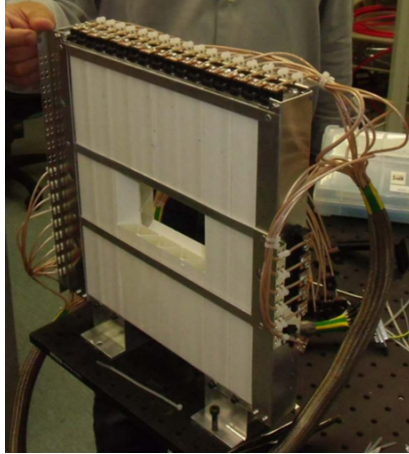


Figure 2.9: An assembled CHANTI station.

and, with an integrated magnetic field of  $0.9 \text{ T m}$  pointed at the negative  $y$  coordinate, provides a  $270 \text{ MeV}/c$  transverse momentum kick towards the positive  $x$  coordinate.

Each chamber contains two modules, and each module contains two views with straws arranged in orthogonal orientation. The two modules have with respect to one another an angular displacement of  $45 \text{ deg}$  with respect to their centers. As every module has a  $12 \text{ cm}$  wide central region with no straws, when the four views are arranged into two overlapped modules a  $6 \text{ cm}$  apothem octagonal hole is obtained for the passage of the beam. The four chambers are displaced in the  $x$  direction to accommodate the beam, which forms with the longitudinal  $z$  axis an angle of  $1.2 \text{ mrad}$  before the MNP33 kick, and an angle of  $-3.6 \text{ mrad}$  after.

The straw tubes are  $36 \mu\text{m}$  thick and are made of polyethylene terephthalate (PET), with an inner coating of  $50 \text{ nm}$  copper and  $20 \text{ nm}$  gold. They have  $9.82 \text{ mm}$  diameter and  $2.16 \text{ m}$  length and contain a mixture of  $70\%$  Ar and  $30\%$   $\text{CO}_2$  at atmospheric pressure. The walls of the straw constitute the cathode, whereas the anode, a gold-plated tungsten wire, runs through its center.

The spatial resolution of the STRAW spectrometer is  $130 \mu\text{m}$ . Its track's angular resolution is  $60 \mu\text{rad}$  at  $10 \text{ GeV}/c$ , and it decreases to  $20 \mu\text{rad}$  at  $50 \text{ GeV}/c$ . The sub-

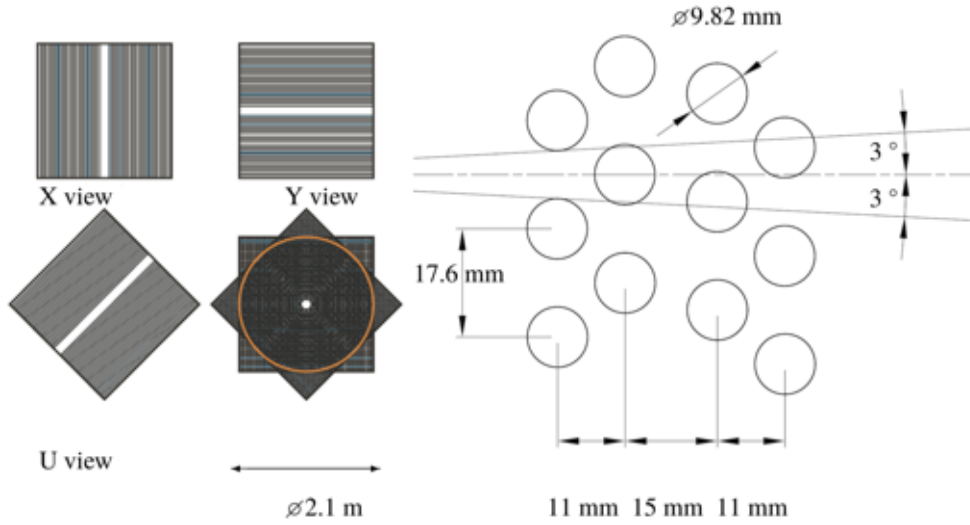


Figure 2.10: The four figures in the left-hand-side picture represent an X, a Y and a U view, and an assembled chamber; the X and Y views together, and the U and V views together, each form a module. The two modules together make up one chamber. The four views have gaps that, when they are overlapped, produce an octagonal hole for the passage of the beam. On the right-hand-side, a scheme shows that a track, produced at a  $\pm 3$  deg angle - the angular range of tracks produced by kaon decays in the FV - always intercepts at least two straws in a view thanks to their sufficiently overlapping arrangement.

detector's momentum resolution is given by:

$$\frac{\sigma(p)}{p} = 0.30\% \oplus 0.005\% \cdot p \quad (2.1)$$

The STRAW sub-detector is used to provide momentum and direction measurements for charged pions produced in the  $K^+ \rightarrow \pi^+ \gamma \gamma$  decay, discussed in chapter 5.

### 2.3.5 The Photon Veto System

Many kaon decays have two or more photons in the final state and therefore they constitute backgrounds for the measurements of other channels. This is the case for backgrounds to the  $K^+ \rightarrow \pi^+ \gamma \gamma$  decay and for the  $K^+ \rightarrow \pi^+ \nu \bar{\nu}$ . In order to efficiently reject background channels, NA62 requires a system of veto detectors covering hermetically the angular region reached by kaon decay products. To this end, the following sub-detectors are employed:

- Large Angle Veto (LAV) - covering between 8.5 and 50 mrad;
- Liquid Krypton Calorimeter (LKr) - covering between 1 and 8.5 mrad;
- Intermediate Ring Calorimeter (IRC) and the Small Angle Calorimeter (SAC) - covering below 1 mrad;

In my analysis of the  $K^+ \rightarrow \pi^+\gamma\gamma$  decay, I used the LKr sub-detector for measuring the energies of the produced photons, and the LAV, IRC and SAC in veto, for detecting additional photons produced in background channels. The analysis will be fully described in chapter 5. The sub-detectors are described in the following sub-sections.

### The LAV

The LAV consists of 12 stations of circular shape that surround the beam. They are located at different longitudinal positions across the fiducial volume and the downstream region. The first 11 stations are operated in the vacuum chamber, whereas LAV12, placed 3 m upstream of the LKr, is operated in air. The ring-shaped stations employ detector modules previously used in the calorimeter of the OPAL experiment.

The modules consist in Schott SF57 lead-glass blocks, where electromagnetic showers are produced and detected via Cherenkov radiation. The blocks are 37 cm long and have front and rear faces measuring respectively  $10 \times 10 \text{ cm}^2$  and  $11 \times 11 \text{ cm}^2$ . The blocks are coupled via 4 cm long light guides to Hamamatsu photomultiplier tubes (PMTs).

The modules are arranged in rings, and several rings form each station in order to provide the necessary number of radiation length to contain showers from incoming particles. The stations that are operated in vacuum are assembled in three different sizes; the radius is larger as the distance from the decay region increases.

Examples of assembled LAV stations and a lead-glass module can be found, respectively, in fig. 2.12 and fig. 2.11.

The LAV stations provide angular coverage from 8.5 to 50 mrad for particles emitted in decays that take place in the fiducial volume on the longitudinal axis. The sub-detector's

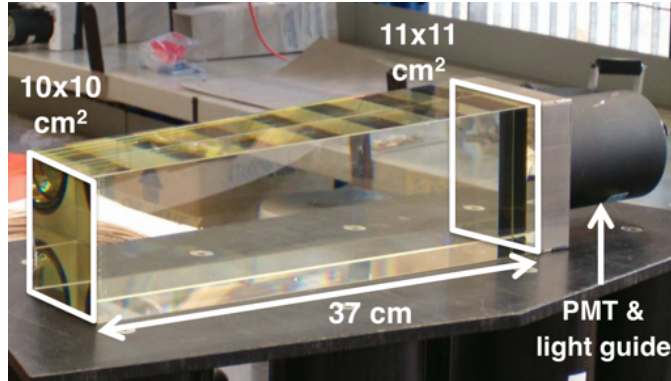


Figure 2.11: A lead-glass block coupled to a photomultiplier tube (PMT) via optical fiber. Originally used for the OPAL calorimeter, these modules are arranged in rings, and the rings grouped together to form the LAV sub-detector stations.



Figure 2.12: Fully assembled LAV1 (left) and LAV12 (right) stations.

time resolution is of the order of 1 ns and an energy resolution of 10% for photons with 1 GeV energy. Each particle reaching a LAV station is detected by at least three rings, which thus provide a minimum effective depth of 21 radiation lengths.

## The LKr

NA62 uses the liquid krypton (LKr) quasi-homogeneous calorimeter previously employed by the NA48 experiment at CERN [54]. The choice of a liquified noble gas is motivated by the stability of the produced signals, and its good correlation to the energy of incoming particles. The quasi-homogeneous configuration allows for the full containment of the electromagnetic showers within the sub-detector's cylindrical volume of 5.3 m<sup>2</sup> cross section and 127 cm length; this corresponds to  $\approx 27$  radiation lengths. The calorimeter is filled with 9000 litres of liquid krypton cooled to 120 K by a cryostat. The active volume is segmented in 13248 cells of dimensions  $2 \times 1 \times 127$  cm aligned with the longitudinal axis, each constituting a double ionization chamber, and read-out by electrodes made of thin Cu-Be ribbons. These are arranged in a zig-zag shape to avoid inefficiencies in case of high proximity of showers to the anodes. A shower produces ionization in  $\approx 120$  cells. A schematic representation of the LKr cells structure can be found in fig. 2.13. The electrodes are connected to preamplifiers inside the cryostat, which collect the signals produced by particles releasing energy in the calorimeter cells. The preamplifiers are directly attached to the calorimeter strips.

The LKr calorimeter provides angular coverage for particles produced on the beamline in the fiducial region between 1 and 8.5 mrad. The energy, space and time resolution of the LKr are the following:

$$\frac{\sigma_E}{E} = \frac{0.032}{\sqrt{E}} \oplus \frac{0.09}{E} \oplus 0.0042 \quad (2.2a)$$

$$\sigma_{X,Y} = \frac{0.42}{\sqrt{E}} \oplus 0.06 \quad (2.2b)$$

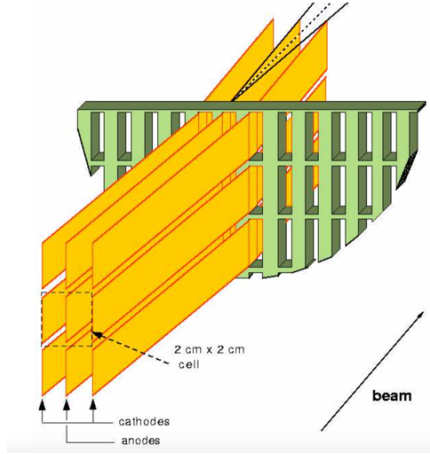


Figure 2.13: Structure of LKr calorimeter cells. For each cell, the central Cu-Be ribbon acts as anode, while the two side ribbons form the cathodes. [54]

$$\sigma_t = \frac{2.5}{\sqrt{E}} \quad (2.2c)$$

where the energy  $E$  is expressed in units of GeV, and the time and space resolutions in ns and cm. In eq. (2.2a) the first term is stochastic, and it represents the signal's statistical fluctuations; the second term accounts for noise and pile-up, whereas the last term accounts for additional effects such as longitudinal leakage and imperfect intercalibration between cells. The LKr's design inefficiency is at the level of  $10^{-3}$  for photons with energy larger than 1 GeV, and of  $10^{-5}$  for photons with energy larger than 10 GeV.

### The IRC and the SAC

The IRC and SAC, forming the Small Angle Veto (SAV) system, provide angular coverage for photons emitted at angles lower than  $1^\circ$ . Both detectors are of Shashlyk type, alternating lead and plastic scintillator plates, and read-out via wavelength-shifting fibers (WSF).

In the SAC, which is the last sub-detector before the beam dump, the plates are stacked into a block, providing a total depth of  $\approx 19$  radiation lengths; the optic fiber ends are arranged in four groups all optically connected, thus making the SAC a single-channel system. In the IRC, which is located before the LKr, ring-shaped layers, composed each of a 1.5 mm thick lead absorber and 1.5 mm thick scintillator plate, are assembled to form

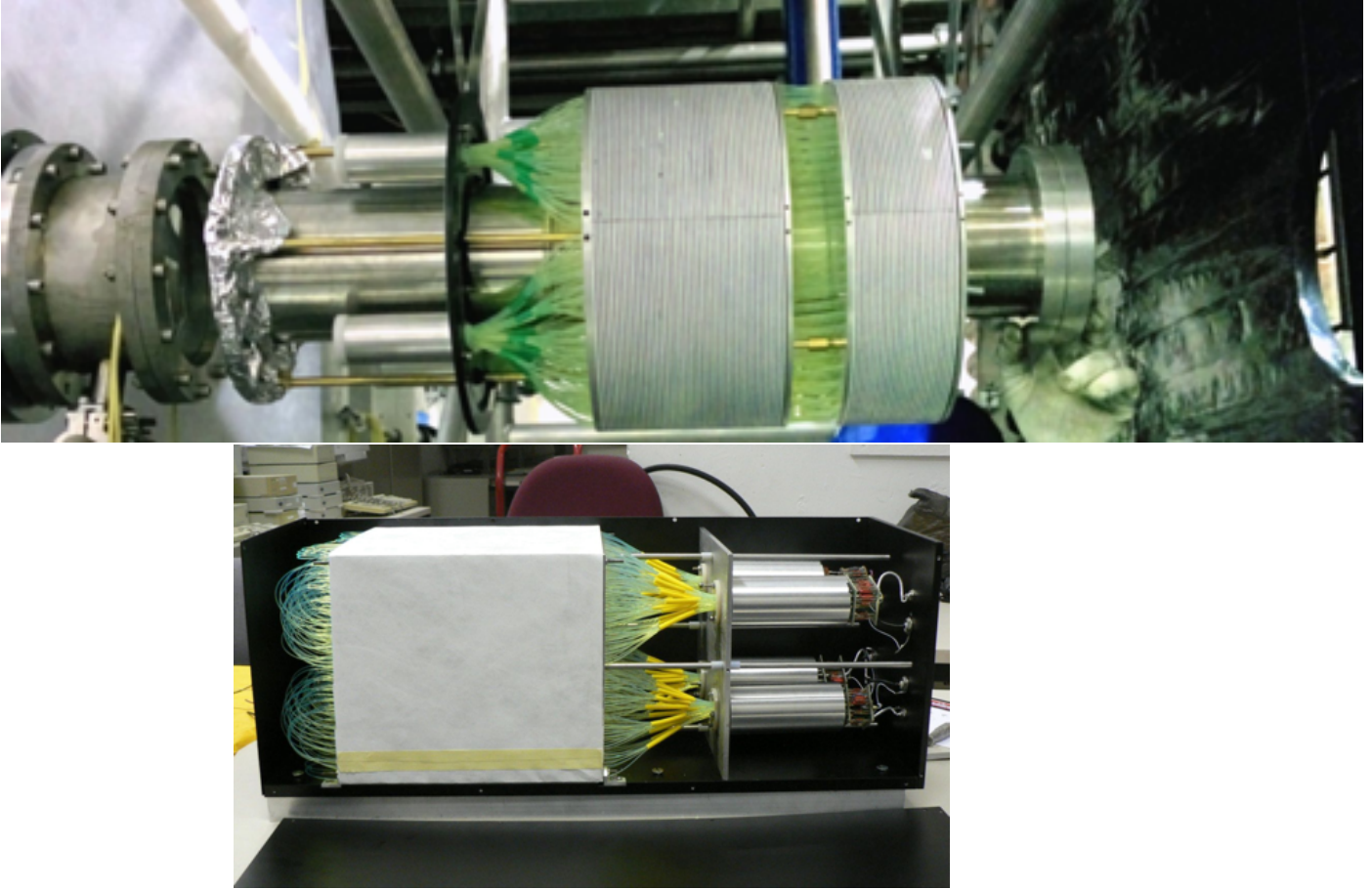


Figure 2.14: Fully assembled IRC (top) and SAC (bottom).

two modules, placed at a distance of 40 mm. The upstream one contains 25 layers, while the downstream is made up of 45 layers. The downstream module has a radius that is  $\approx 2$  mm larger than the upstream one in order to maximise the acceptance for photons from kaon decays in the FV. The IRC is wrapped in black paper in order to make it light-tight, and, as the SAC, it provides a total depth of  $\approx 19$  radiation lengths.

The design inefficiency of both sub-detectors, for photons energies larger than 5 GeV, is of the order of  $10^{-4}$ . On top of 1 MHz of photons, received by both sub-systems, at nominal beam intensity the IRC is also exposed to  $\approx 10$  MHz of muons, concentrated in a spot outside the beamline in the negative  $x$  direction.

The fully assembled sub-detectors can be seen in fig. 2.14 before being installed in the setup.

### 2.3.6 The RICH

NA62 employs a RICH (Ring-Imaging Cherenkov detector) to perform particle identification (PID) for the purpose of separating between pions and muons with 15 to 35 GeV/ $c$  momentum. The detection principle is similar to that of the CEDAR/KTAG's sub-detector; here as well, particles with the same speed (or  $\beta$ ) produce Cherenkov light cones with the same angle, and the light cones are projected onto the focal plane by spherical mirrors. If one knows the momentum of the particle, it is thus possible to discriminate between different mass hypotheses. The RICH's radiator is neon gas, at room temperature and atmospheric pressure to ensure high efficiency for pions in the desired momentum range, housed in a 7.5 m long cylinder made of steel. It is divided in four sections with decreasing radius and uneven lengths, and it houses the photo-detection system, consisting of  $\approx 2000$  Hamamatsu R7400 U-03 PMs placed at its upstream end, where the beam enters the radiator, and a matrix of 20 spherical mirrors at its downstream end. The spherical mirrors, that are made of a 25 mm aluminium coated glass plate, reflect the Cherenkov photons into a ring image on the focal plane, where the PMs are located. The beam passes at the center of the vessel in an aluminium tube. The mirrors belong to two groups: half of them have their centres of curvature on the left, and half on the right of the beampipe, to avoid light being reflected by the latter.

The structure of the NA62 RICH is illustrated in fig. 2.15.

With the RICH, it is possible to achieve muon rejection of at least two orders of magnitude. The RICH also provides the pion's crossing time with 100 ps precision, and is therefore suitable to be used as a reference time for charged tracks.

The RICH is used in the L0 trigger for collecting samples used in my analysis of the  $K^+ \rightarrow \pi^+ \gamma \gamma$  decay (see chapter 5).

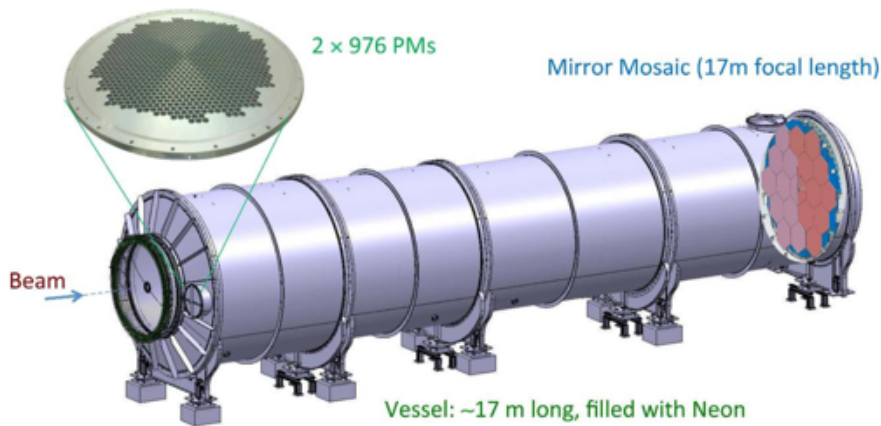


Figure 2.15: Structure of the RICH sub-detector. At the upstream end of the vessel, the beam passes through the volume inside an aluminium tube. At the downstream end of the vessel, a matrix of spherical mirrors reflect back the emitted Cherenkov light into a ring on the focal plane upstream, where the light is collected by a mosaic of PMs.

### 2.3.7 The CHOD and the OldCHOD

The NA62 experiment makes use of two sub-systems for the fast detection of charged tracks to be used to form a trigger decision. These are two hodoscopes for charged tracks (CHODs).

The first one, from the NA48, consists of two planes each containing 64 slabs of plastic scintillator; the the slabs in one plane are orthogonal to the slabs in the other, and are read-out individually and provide independent time responses for charged particles hitting both planes. The slabs have lengths varying between 1210 and 600 mm and widths varying between 65 and 99 mm, with the narrower slabs located in the region closer to the beam. The slabs are arranged to form an octagon, as visible in fig. 2.16;

The second one was designed and built on purpose to provide high performance with the particle rate at NA62; it consists of a matrix of 152 tiles, with finer granularity in the region surrounding the beampipe. The tiles are made of plastic scintillator and are 30 mm thick, with all tiles except those near the edge having 108 mm height, and widths of either 134 or 268 mm. The tiles are arranged in the shape of an octagon with 1550 mm apothem.

The geometric acceptance of the two detectors, located respectively upstream and

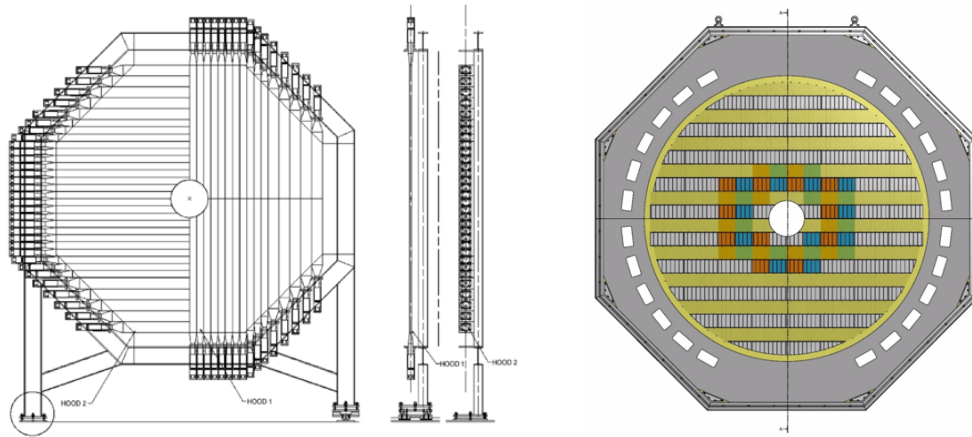


Figure 2.16: The charged hodoscopes used in the NA62 trigger to quickly detect the passage of a charged track. On the left, the NA48 CHOD, consisting in two planes of scintillator slabs; on the right, the CHOD, consisting in a matrix of scintillator tiles, with finer granularity near the beam passage region.

downstream of the LAV12 station, covers the area between the IRC outer radius (145 mm) and the LAV12 inner radius (1070 mm).

Both the NA48 CHOD and the CHOD are used in the L0 trigger decision for selecting samples used in my analysis of the  $K^+ \rightarrow \pi^+ \gamma \gamma$  decay, which will be described in chapter 5.

The time resolution of the charged hodoscopes is of the order of 200 ps.

### 2.3.8 The MUV1 and MUV2

Two hadronic sampling calorimeters, MUV1 and MUV2, located downstream of the LKr calorimeter, perform  $\pi/\mu$  separation. The two modules are composed of alternating layers of iron and scintillator material. The total number of interaction lengths provided is 8.

The MUV2 was inherited from the NA48 experiment, and it consists of 24 plates of 25 mm iron alternating with layers of plastic scintillators. Each scintillator plate is made of 44 strips that have dimensions  $1300 \text{ mm} \times 119 \text{ mm} \times 4.5 \text{ mm}$ , and are aligned in planes with orthogonal orientations. The detector is read-out by PMs via WSF, with each fiber reading-out strips in the same plate with the same orientation.

The MUV1 was built on purpose for use in NA62; it is endowed with finer granularity in order to better separate between the electromagnetic and hadronic components in

showers. In this case as well, the sub-detector consists of 24 layers of iron alternated to plastic scintillator. The scintillator plates are made of strips with 9 mm thickness and 60 mm width. Similarly to the MUV2, the strips are read-out by PMs via WS fibers.

### 2.3.9 The MUV3

The MUV3 is a muon veto detector. It follows MUV1 and MUV2, and it is located behind an 80 cm thick iron wall. Its task is that of vetoing muons, that make up most of the rate of charged particles surviving the passage through the calorimeters and the iron wall, and therefore it is used to make trigger decisions. One of the samples used for my analysis of the  $K^+ \rightarrow \pi^+ \gamma \gamma$  decay uses the MUV3 in the L0 trigger (for more details see chapter 5). The rate of muons travelling through the detector at nominal beam intensity is 13 MHz. The MUV3 is built from 50 mm thick scintillator tiles, and has a surface of  $2640 \times 2640 \text{ mm}^2$ . Each tile is read-out by a PM located behind it. The MUV3 has a time resolution in the range 0.4 - 0.6 ns.

### 2.3.10 The MUV0 and the HASC

The MUV0 and the HASC are used to detect pions coming from  $K^+ \rightarrow \pi^+ \pi^+ \pi^-$  that are not covered by the lateral acceptance of the STRAW spectrometer. The main motivation for the installation of these sub-detectors is to reduce the background to  $K^+ \rightarrow \pi^+ \nu \bar{\nu}$  decays. The two sub-detectors are designed to perform the following tasks:

- The MUV0 detects negatively charged pions with momenta below  $10 \text{ GeV}/c$ , deflected by the MNP33 magnet towards the positive  $x$  direction;
- The HASC detects positively charged pions with momenta above  $50 \text{ GeV}/c$  that escape STRAW chambers detection through their central beam holes, and are successively deflected by the BEND magnet towards the negative X direction.

The MUV0 has an active area of  $1.4 \times 1.4 \text{ m}^2$  and it is mounted on the downstream face

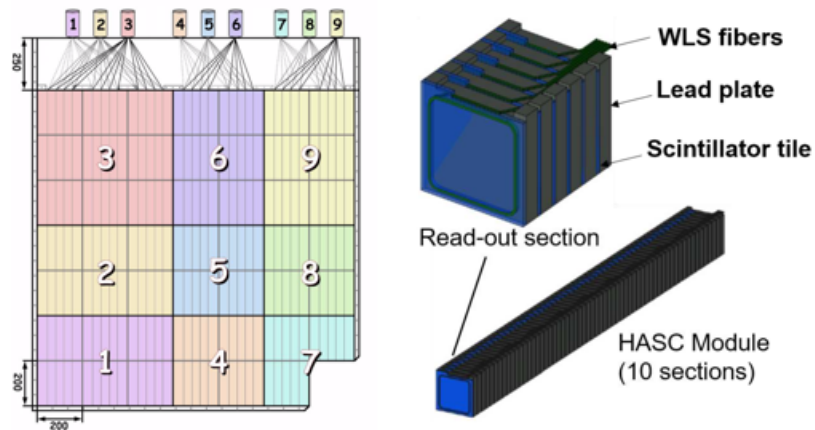


Figure 2.17: On the left-hand-side, the MUV0 sub-detector’s active area with the arrangement of tiles in 9 super groups; on the right-hand-side, a HASC module.

of the RICH. It consists of 48 tiles of plastic scintillator arranged in nine groups or super-tiles (see left-hand-side of fig. 2.17), each read-out via WSF coupled to Hamamatsu R7400 PMs. The HASC consists of 9 identical modules, inherited from the NA61 experiment, that are made alternating 60 plates of lead and 60 plates of scintillator material. Each tile, containing 6 scintillator plates, is read-out by a WSF coupled to a Hamamatsu silicon photomultiplier (SiPM) and an amplifier and bias board. The structure of a module can be found in the right-hand-side of fig. 2.17.

### 2.3.11 Summary

In this chapter, the NA62 beamline and experimental set-up have been described. While all sub-detectors are used in the analysis of the  $K^+ \rightarrow \pi^+ \nu \bar{\nu}$  decay, the analysis of the  $K^+ \rightarrow \pi^+ \gamma \gamma$  makes use of a sub-set of them, either in the trigger streams or in the signal and normalisation selections. The measurement of  $K^+ \rightarrow \pi^+ \gamma \gamma$  with NA62 data is fully described in chapter 5.

## CHAPTER 3

# THE NA62 DATA-ACQUISITION, TRIGGER AND SOFTWARE

The analogue signals produced in the various NA62 sub-detectors are converted to digital signals by front-end electronics (FEE) and successively read-out by data-acquisition (DAQ) boards. Not all the information collected, though, can be permanently stored. The amount of necessary data reduction is dictated by considerations on the particle rate and the available bandwidth.

In NA62, data reduction is performed by a multi-level trigger system [52]. The system must allow flexibility of the trigger conditions, in order to suit the experimental needs driven by the adoption of a novel technique, and in order to be able to expand the scope of the possible physics studies.

The TDAQ system, designed and used by the NA62 experiment, is described in the present chapter. Particular emphasis will be placed on the high-level trigger (HLT) system, as I have contributed to its development by producing software tools necessary for running trigger algorithms for the STRAW sub-detector.

### 3.1 The trigger system

NA62 is a fixed target experiment which makes use of a beam of protons produced by the CERN SPS. The primary proton beam, impinging on T10 target, is delivered in *spills*

or *bursts* each lasting  $\approx 3.5$  s, and separated from one another by a  $\approx 10$  s long time interval. As mentioned before, not all of the data recorded by the sub-detectors during an SPS spill can be stored for analysis; the available bandwidth for permanent data storage corresponds to a rate of the order of 10 kHz. To cope with these limitations, the NA62 experiment makes use of a multi-level trigger chain, consisting of a hardware stage (level-0, or L0) and a software stage (the High Level, or HL).

The rate of particles from the secondary beam on the NA62 sub-systems varies across the length of the apparatus. At nominal beam intensity, that is  $\approx 10^{12}$  SPS protons per burst, the rate of beam particles is of the order of 1 GHz [55]. The rate of beam particles on the upstream sub-detectors is of the order of 750 MHz, of which  $\approx 50$  MHz is due to kaons; as a result the rate of  $K^+$  decays in the fiducial volume (FV), which extends across approximately 65 m starting from  $\approx 115$  m from the target, is  $\approx 10$  MHz. The downstream sub-detectors are, therefore, the most suitable to consult when making a quick decision on whether the event is of interest.

The first trigger stage, the L0, is hardware-based and must reduce the rate from 10 MHz down to 1 MHz. Altogether, the HLT, designed to contain up to two levels, must achieve a reduction factor of at least one order of magnitude. In the 2015-to-2018 data-taking, the HL contained a single level (L1). The verdict of HLT is the result of the execution of trigger algorithms running on a dedicated network of computers (the PC-farm).

In table 3.1 one can find the rates and bandwidths at each stage of the trigger system. In the following paragraphs, the data reduction at every step of the trigger chain is summarised, and the full flow of data from sub-detectors to permanent storage is described.

### 3.1.1 The data flow from detection to storage

The NA62 DAQ system is designed to collect data between two times delimiting the burst duration: the Start-of-Burst (SOB) and End-of-Burst (EOB). SOB and EOB signals are sent to the read-out systems of every sub-detector. Moreover, the same synchronisation

output of:	L0	L1
rate	1 MHz	100 kHz
bandwidth	6 GB/s	2 GB/s

Table 3.1: Rates and bandwidths for each stage of the NA62 trigger system. The bandwidth reduction between L0 and L1 output is smaller than a factor 10 because at this stage data from the GTK and the calorimeters is requested by the PC-farm. An SPS spill lasting  $\approx 3.5$  s produces 6 GB of data for permanent storage.

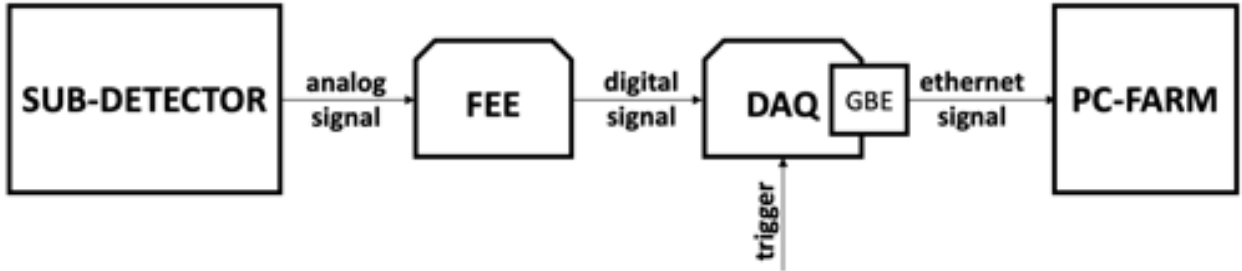


Figure 3.1: From left to right: analog signals are produced by each sub-detector and sent to FEE boards; here, they are converted in digital form as a series of edges. These are successively transferred to DAQ boards, where a timestamp is assigned to each edge, to be transmitted to the PC-farm via ethernet upon request from the Level-0 Trigger Processor (L0TP).

and timing, in units of approximately 25 ns, is provided to each sub-system participating in the data acquisition.

The signal transformation from analog to digital form and its transmission to the PC-farm is shown in fig. 3.1. The analog signals produced by each sub-system between SOB and EOB are converted by FEE into digital form as a sequence of *edges*. These can be of two types: *leading*, indicating the time of rise of the signal above a threshold, and *trailing*, indicating the time of falling below the threshold. The TDCs settings can be changed to produce one or both types of edge. Every sub-detector uses FEE boards that best match its characteristics.

The digital signals provided by the FEE boards are then transferred to the DAQ boards, which produce timestamps from the leading and trailing edges signals. As it is the case for the FEE boards, different DAQ boards are used by different sub-systems, based on their characteristics and the desired performance; they are briefly discussed in

section 3.2. Most sub-detectors use boards with a common architecture, called TEL62s; the other ones use custom-designed read-out boards.

For the STRAW spectrometer, which has a poorer time resolution compared to other sub-detectors (track time resolution  $\approx 5$  ns), less precise TDCs are necessary; at the same time, its number of channels is the largest among the TDC-based sub-detectors. Considering these characteristics, a cost-effective, custom read-out system has been designed for this sub-detector.

More detail about the Spectrometer read-out boards (SRBs), which I worked on while writing tools for the STRAW sub-detector's online trigger system, and about the TEL62s, will be provided in section 3.2. Custom-designed read-out systems are also used for the GTK and the calorimeters.

The data, in the form of timestamps, is temporarily stored in buffers in the DAQ boards, and it is transferred to the PC-farm only when prompted by the L0TP. A flow diagram with all the steps from the L0 trigger verdict to permanent storage is shown in fig. 3.2.

The L0 trigger decision is performed based on fast information provided by the detector. To this end, a number of sub-systems, as described in the rest of the present section, continuously send to the L0TP trigger *primitives* during a burst. Primitives are reduced data-packets in the form of 32-bit data words. The nature of primitives depends on the sub-detector's characteristics.

The specific sequence of operations from primitives transmission to storage and the TDAQ elements that carry out each task are shown in fig. 3.3. When prompted, the CHOD, RICH, LAV, MUV3, NA48 CHOD and the calorimeters send primitives to the L0TP (n.1 in fig. 3.3) through a dedicated network. In order for the L0TP to accept an event as potentially interesting, this must satisfy at least one of a set of conditions, called *trigger masks*. Each mask consists of a combination of requirements on detector primitives. In the L0TP, up to 16 different trigger masks can be defined. Once a mask condition is satisfied, the L0TP sends to the PC-farm a packet of data containing information about

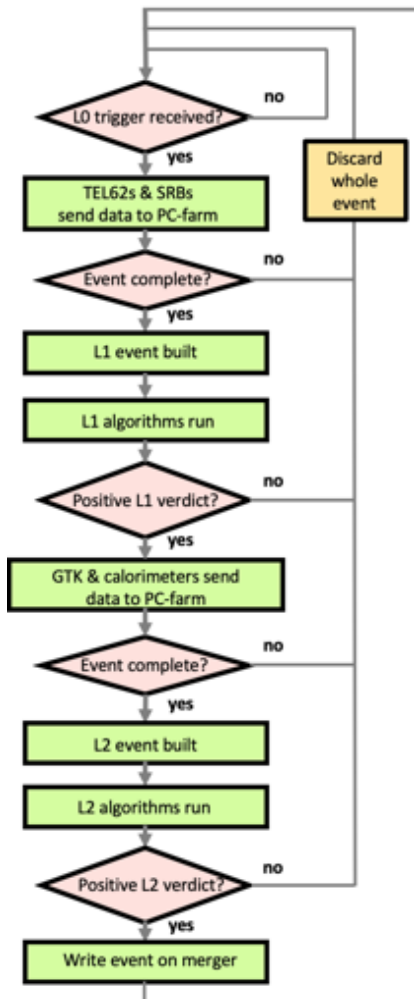


Figure 3.2: Flow chart of event building and trigger execution, from a L0 positive verdict to permanent storage, in case of a HLT system containing two levels. From top to bottom: upon receiving a signal from the L0TP, TEL62s and SRBs send their data-packets to the PC-farm, which combines them into a L1 event and the runs L1 trigger algorithms. If the outcome of the latter is positive, the farm requests data also from the GTK and the calorimeters, and runs L2 trigger algorithms. If the verdict of L2 is positive as well, the full event is built and written to merger for temporary storage before being transferred to CASTOR machines.

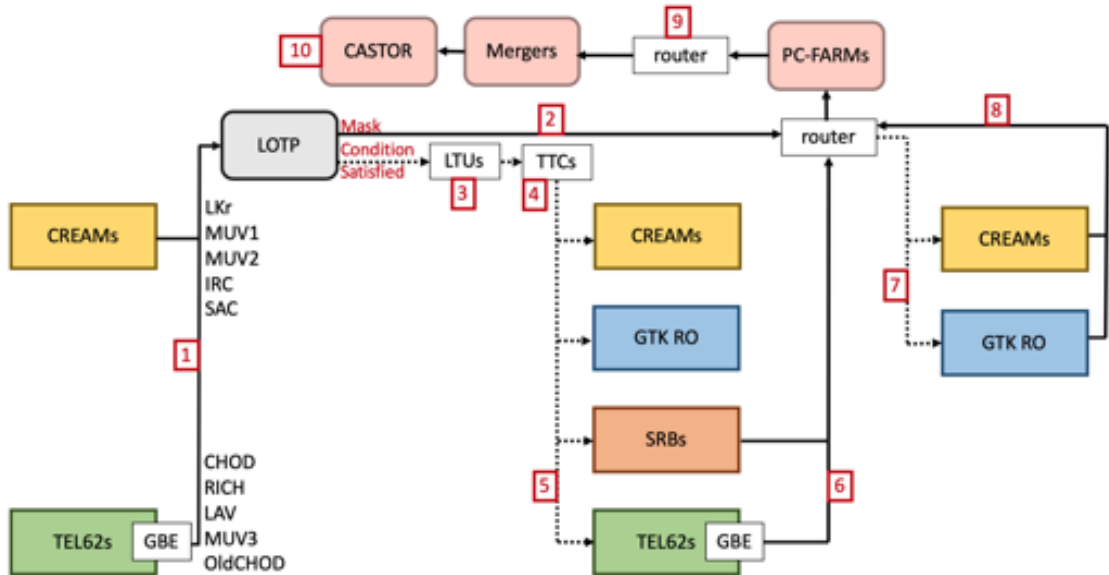


Figure 3.3: Scheme of the TDAQ elements involved in each step of the trigger execution, event building and storage. The TEL62- and CREAM-based sub-detectors send primitives to the LOTP (1); based on this information, the latter decides whether to keep or discard the event. In case of a positive response, it sends a signal to the DAQ boards of all sub-systems via Logic Trigger Units or LTUs (3), that use the Timing, Trigger and Control (TTC, 4) to transfer the signal through optical fibers, and at the same time transfers a data-packet with primitives and trigger masks information to the PC-farm (2). All the TEL62-based sub-detectors, and the SRBs, send their data to the PC farm at this stage (6). The farm then executes L1 trigger algorithms, and, only in case of a positive L1 verdict, the GTK and the calorimeters send their data packets. This decision is led by the large amount of data coming from the latter sub-detectors. Once the farm has collected data-packets from all the sub-systems, in case L2 algorithms are implemented, its algorithms can be executed; if the event is successfully selected also at this stage, the packets reach one of the three merger computers, where they are combined together. The event is then sent to CASTOR for permanent storage.

the trigger primitives and the mask (n.2 in fig. 3.3); it also sends a trigger signal to the sub-detectors via Logic Trigger Units or LTUs (n.3 in fig. 3.3) that make use of a TTC system (n.4 in fig. 3.3) to transfer the signal through optical fibers (n.5 in fig. 3.3).

Upon a positive verdict of the L0 trigger based on sub-detectors' primitives, data packets are requested from all TEL62-based systems and from the SRBs (n.6 in fig. 3.3). Because of their large volume, data packets from the GTK and the calorimeters are not requested yet at this stage. If the data is correctly transferred to the PC-farm, the L1 event, based on this reduced set of sub-detectors, is built, and the L1 algorithms are executed.

At L1, it is possible to define up to 16 trigger masks, in an analogous way to the L0 case. If the L1 gives a positive response, then data from the remaining sub-detector's read-out boards is requested (n.7 in fig. 3.3), and the PC builds the full event based on information from all sub-systems (n.8 in fig. 3.3). For future data-taking, L2 trigger algorithms might be implemented to run at this stage. In case all the HLT stages have accepted the event, the latter is sent to one of three merger PCs and temporarily stored there (n.9 in fig. 3.3), until transfer to permanent storage to CASTOR, the CERN hierarchical mass storage system (n.10 in fig. 3.3), via the Central Data Recording service (CDR). The output rate is limited by the available network bandwidth (10 Gb/s) and by the writing speed of the CDR, which is  $\sim 200$  MB/s.

For testing purposes, at the end of each burst the trigger system sends special signals to the system, upon which all sub-detectors boards are prompted to deliver monitoring data via the same streams of the standard data. During offline analysis it is therefore possible to access this monitoring information alongside with the data.

## 3.2 The NA62 DAQ system

The DAQ boards used by the various sub-systems are listed in the following:

- CREAM: used by the calorimeters (LKr, MUV1 and MUV2);

- SRB: used by the STRAW spectrometer;
- GTK RO boards: used by the GTK spectrometer;
- TEL62: common to all other sub-detectors.

The TEL62 boards, also used by the KTAG sub-detector, and the SRBs, for which I developed encoding and decoding tools in the software framework as part of my PhD work, are discussed in the following paragraphs.

**The TEL62s** The TEL62 is the RO board used by most of NA62 sub-detectors. Its architecture is based on the TELL1 board that was originally developed for the LHCb experiment; the design has, though, been largely modified and adapted to increase its computational, storage and inter-communication capabilities for use in NA62.

TEL62s are equipped with TDC mezzanine boards (TDCBs), each of them housing 4 High Performance TDC (HPTDC) chips controlled by an FPGA (PP). Each TDCB can digitize leading and trailing edge times from 128 channels. A TEL62 board, which is equipped with 4 TDCBs and a central FPGA (SinkLink or SL) that combines information from the TDCBs, can therefore read-out up to 512 channels.

In the HPTDCs, the digitized data is arranged in  $6.4 \mu\text{s}$  long *frames*, which are later matched and merged by the FPGA in 25 ns wide time slots, in the format requested by the read-out after a positive L0 trigger verdict. The data is subsequently arranged in blocks of adjacent data words and stored in large time-slot memories in each TDCB with a maximum latency of several ms.

In each TEL62, data from the various PPs is combined by the SL into a *fragment*. Several fragments are packed together to form multi-event UDP packets (MEPs), and sent via Gigabit Ethernet links to the PC farm. Copies of the data are sent to the firmware in both the PP and SL for monitoring purposes, and for the production of L0 trigger primitives. A four-port Quad Gigabit Ethernet card (QGBE) sends trigger primitives to the L0TP and data to the PC farm after a positive L0 trigger response.

**The STRAW Read-out Boards (SRBs)** The read-out system of the STRAW sub-detector is based on the CARIOCA chips, developed for the LHCb experiment, and follows the modularity of the straw tubes. The chips are capable of reading both leading and trailing edges information, the former providing information on the radial crossing position of the particle in the tube, and the latter used to group hits belonging to the same tracks. Each group of 16 straws is served by a FE board consisting of two CARIOCA chips (corresponding to 8 straws each), one chip with 16 Digital-to-analog (DAC) converters used to set discriminator thresholds, and one FPGA controlling 32 TDCs. Data and FE boards controls are transmitted via ethernet cables.

16 FE boards are managed by a custom-made board, the SRB; one STRAW chamber is read-out by 8 SRBs housed in the same crate, located at a distance of  $\sim 10$  m from the detector. Upon a positive verdict from the L0 trigger, data is sent to the PC farm via Ethernet connection.

### 3.3 The NA62 L0 trigger

Detector primitives are encoded in 64-bit data blocks containing information about time and the satisfied conditions; up to 16 trigger masks can be defined based on the different detector primitives. The detectors involved in L0 trigger decision-making and the type of primitives they provide are listed below:

- NA48 CHOD: provides primitives for charged tracks in the form of multiplicity of coincidences between slabs;
- CHOD: provides primitives for charged tracks in the form of coincidences between two PMTs on the same tile;
- RICH: provides primitives for charged tracks above the Cherenkov threshold, in the form of hit multiplicity;

- LAV, station 12: provides primitives for photon and halo muon vetoing in the form of multiplicities in adjacent lead-glass blocks;
- MUV3: provides primitives in the form of tile multiplicities, and can be used both in positive and veto logic;
- Electromagnetic (LKr) and hadronic (MUV1 and MUV2) calorimeters: they provide primitives in the form of energy deposits and cluster multiplicity to perform pion identification; they can also be used in negative logic as a veto, using cluster multiplicity.

The NA48 CHOD, the CHOD and the RICH also provide high quality reference times, with a resolution of the order of respectively  $\approx 200$  ps,  $\approx 1$  ns and  $\approx 100$  ps.

Two special roles exist in the L0 trigger:

- the *control* detector is used to collect a sample of minimum-bias data. This role is typically taken by the NA48 CHOD;
- the *reference* detector is the one that is used for the fine time of the trigger, and must be present with positive logic in every trigger mask. This role is typically taken by the RICH or the CHOD.

Alongside the physics trigger streams, minimum bias samples, which are data samples collected using minimum cuts, with control trigger and other dedicated masks, are collected. With these samples, that typically occupy  $\approx 30\%$  of the total bandwidth, one can perform efficiency studies for the other trigger lines. Furthermore, using minimum bias data one can pursue physics studies for which it is not feasible to add a dedicated trigger chain in order not to reduce the available bandwidth for the main physics goals. An example is the measurement of background channels affecting the decays under study.

**The L0TP** The L0TP is an FPGA-based system which has the task of collecting trigger primitives, ordering them in time, and checking if they satisfy any of the trigger

mask conditions. The ordering is performed based on information included in the primitives, namely a coarse timestamp (with 25 ns precision) and a fine time (with 100 ps precision). Primitives are sent to the L0TP every 6.4  $\mu$ s. A downscaling factor can be applied to the L0TP generation, reducing the number of events that are passed to the HLT by a programmable factor.

For each sub-detector involved in the L0 trigger, two mechanisms, the CHOKe and the ERROR, ensure that the L0TP is able to stop, signal and resume at the appropriate time the trigger dispatching in case of critical flow or a loss of data.

## 3.4 The NA62 HLT

The previously introduced HLT is a software-based trigger that performs data reduction from the L0 output rate (1 MHz) down to the available bandwidth and storage capacity. It can accommodate for up to 2 separate levels, L1 and L2, although during the 2015-to-2018 data-taking only L1 algorithms have been implemented. The HLT, part of the Online System in the NA62 software framework, employs a series of C++ algorithms running on a dedicated farm of computers in order to decide whether to store or discard the event.

### 3.4.1 The NA62 software framework

The NA62 software consists of an offline framework and an online framework, both written in the C++ language. The offline framework, or NA62fw, consist of three main components: a MonteCarlo simulation framework (NA62MC), a detector reconstruction framework (NA62Reconstruction), and an analysis framework (NA62Analysis). Once data-packets, in the form of raw binaries, are sent from the merger PCs to permanent storage, they are ready to be read and reconstructed by the NA62fw. NA62Reconstruction has been designed to work in a completely parallel way on both MC-generated events and data. This is achieved through intermediate objects, *digis*, containing information such

as edge types and times, that can be built either starting from data by an *offline decoder*, or starting from MC by a *digitizer* (refer to fig. 3.4). The online framework consists of the code running on the PC-farm and responsible for event building and HLT algorithms execution, and it is described in more detail in the following sub-sections.

### 3.4.2 The NA62 Online System

A raw data packet stored by a specific DAQ board and corresponding to a specific event is called a *fragment*. Fragments, that are blocks of binary data, are not sent one by one by DAQ boards to the PC-farm upon a positive L0 trigger decision; they are, instead, arranged in Multi Event Packets (MEPs). Each MEP contains fragments corresponding to a number of events, called *MEP factor*, dispatched all at once to specific network nodes, so that fragments produced by the various sub-detectors and corresponding to the same event are delivered to the same computer. Each sub-detector dispatches at the same time a number of MEPs equal to the number of the DAQ boards it employs. Different formats of MEPs are adopted by different types of read-out boards.

The PC-farm waits to receive MEPs from all the sub-detectors participating in the L1 trigger decision; once all fragments have been received for a specific event, they need to be decoded from their binary board-dependent format into variables suitable to be used by the HLT algorithms.

These contain information such as hit times, types, readout board and channel IDs. A dedicated tool for each type of DAQ boards performs the decoding in the online framework. All the HLT algorithms can then be run without any further transfer of data.

### 3.4.3 The testing environment

Besides the standard operations described above, that belong to the normal processing and transmission of data, the Online System is equipped with a testing framework. The latter can be accessed from any personal machine, and it simulates the software running

on the farm, thus allowing the development and testing of HLT algorithms before they are deployed on the PC-farm.

The data is sent by the sub-detectors as input to the PC-farm via ethernet in the form of binary packets. The input format for the testing framework, instead, consists of a file containing binary data packets, and a header file containing the recipe necessary to interpret the data file. The formats of the input packets read by the PC-farm and the testing environment are therefore different. In order to write the raw data into a format suitable for the testing framework, one needs to transform it into digis with the NA62Reconstruction offline decoder, and then to convert it to the appropriate binary format via an encoder in the offline system, which gives as output both the binary file and the header file. This sequence of operations is shown in fig. 3.4. As the offline encoder uses digis as its input, it is possible to run and test HLT algorithms on MC as well.

The Online System reads the binary and header files produced by the offline encoder; it then uses the online decoder described in the previous chapter to derive sub-detector-specific information used as input by HLT algorithms.

### **3.5 The Online System software framework**

The three tasks performed by the NA62 Online System are coded in three C++ projects that share a common set of libraries; they are listed below:

- na62-farm: it runs on a cluster of 30 PCs, and its tasks are event building, running HLT algorithms, and sending the event that pass all trigger levels to the merger PCs for storage;
- na62-trigger-test: it can be accessed from any machine, and its task is reproducing the behaviour of na62-farm trigger algorithms, allowing studies of the performance of any of its components;
- na62-merger: it runs on a cluster of 3 PCs, it receives data corresponding to events

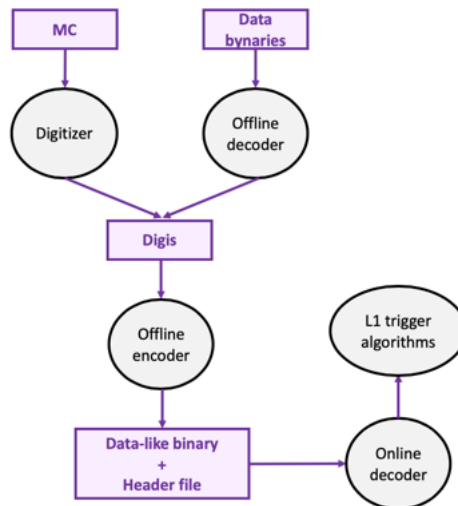


Figure 3.4: Data binaries and MC are transformed into digis, objects that contain information such as edge types or times, by dedicated tools in the NA62Reconstruction framework. Starting from MC, digis are produced by a digitizer, whereas for raw data such task is performed by an offline decoder. One can then use digis to produce data-like binary packets in a format suitable as input to the online testing framework; this consists of a binary file accompanied by a header file, which contains instructions for the PC-farm to interpret the binaries. In the Online System, running on the PC-farm, binary and header file are used by an Online Decoder to extract information necessary to run HLT algorithms.

that have been accepted by the HLT and writes them to file burst by burst; it then stores them temporarily before sending them to the CDR for permanent archiving.

The additional components in the Online System that are used by the main projects are:

- na62-trigger-algorithms: it performs the decoding of MEP packets, and contains the HLT algorithms and processes;
- na62-farm-lib na62-farm-lib: it is a general static library that stores data types and useful helper classes for all na62-farm components;
- na62-farm-lib-networking: it is a library used for network communications;
- na62-dim-interface: it handles communication between na62-farm and na62-merger projects, and allows the PC-farm and the PC-merger to send and receive status updates.

During my PhD I have contributed to the na62-trigger-test and na62-trigger-algorithms projects, by developing the components described below.

### 3.5.1 Tools for running HLT algorithms for the SRBs

The data flow described in fig. 3.4 has as its final output a file of binary data-like packets and a header file that can be read by the online testing framework. All detectors participating in the L1 trigger except the STRAW spectrometer have read-out systems based on TEL62 boards, and therefore send data packets with a common format. The same tools in the offline and online systems are used for digitization, encoding, and decoding of data.

The STRAW spectrometer, that also participates in the L1 decision, uses a different read-out architecture based on SRBs, and sends data in a different format from the other sub-systems. It thus requires dedicated tools in the software frameworks.

At the time I started my PhD, the following tools had not yet been implemented for the STRAW spectrometer:

- An encoder in the offline system, to produce a data-like binary and a header file for the testing framework starting from digis;
- A decoder in the online system, to extract from those files the information necessary for running HLT algorithms.

As my first PhD task, I implemented the above tools in the software frameworks. As shown in fig. 3.4, the Offline Encoder reads digis from the STRAW spectrometer and writes them into MEP format. This consists of a header with the number of the first event, the total number of events, the sub-detector ID and sub-ID of the read-out board that sent the data, and the total length of the packet. The MEP header is followed, for each group of events, by an event header and a series of event data blocks. The former contains information such as the board ID and the L0 trigger type, while the latter consist of a series of time-ordered data words containing the edge time and type and the

ID of the specific STRAW. The task of the offline encoder is that of writing header and binary files according to the MEP format. The Online Decoder running on the PC-farm successively re-extracts edge times and types from the binary file, for them to be used as input in HLT algorithms. The development of the above tools allowed the development of a L1 algorithm for the STRAW, which is based on the full reconstruction of tracks through pattern recognition after two hit-clustering steps. The algorithm is designed to identify charged tracks from the decays of interest while ensuring that accidental tracks are removed; to this end, various trigger conditions can be set on the track's quality and its longitudinal momentum, and the vertex can be requested to be within a specified fiducial volume.

### **3.5.2 HLT output structures**

Events that have been accepted by the HLT, coming from all sub-systems, are written in packets and sent to storage, at the same time as information on the trigger configurations. These are arranged in specific output C++ structures. As part of my work, I have developed such structures in the online framework.

### **3.5.3 Summary**

In the present chapter, the NA62 data-acquisition and trigger system have been outlined. In particular, the HLT system, which I contributed to develop, has been discussed. The tools I provided for the STRAW spectrometer, performing the encoding and decoding of data and MC and allowing testing trigger algorithms for this sub-detector, have been discussed.

## CHAPTER 4

# THE CEDAR/KTAG SUB-DETECTOR

As discussed in the previous chapters, the NA62 experiment makes use of a 400 GeV/c proton beam from the SPS accelerator. A 75 GeV/c beam of secondary hadrons, consisting of 6%  $K^+$  and about 70%  $\pi^+$  and 20% protons, is produced by colliding the protons with a Beryllium target (T10) in the CERN North Area.

As a beam pion can scatter in the vacuum tank's residual gas and travel through the downstream detectors mimicking an event of  $K^+ \rightarrow \pi^+ \nu \bar{\nu}$ , in order to reduce background it is necessary to efficiently identify, or *tag*, kaons in the beam. This task is performed, in NA62, by the CEDAR/KTAG, the first sub-detector in the NA62 beamline, located about 70 m downstream of the target.

The sub-detector is composed of two sub-systems, a CERN CEDAR and a photon detection and read-out system, the KTAG. The CEDAR is a Cherenkov Differential Counter with Achromatic Ring Focus. CEDARs were designed by CERN in the late 1970s with the aim of separating kaons, pions and protons in secondary beams of charged particles extracted from the SPS accelerator. Their original optics, though, are unable to cope with the NA62 rate of particles. For this reason, a new optics and read-out system, the KTAG, has been developed on purpose for use in NA62.

During my PhD, I have worked on several aspects of the detector's operation. I have served as detector expert for several data-taking periods and I produced the very first version of the *KTAG expert handbook*, a manual meant as support to experts for the

setting-up, problem-solving and monitoring procedures to be carried out at data-taking time and beyond. I have furthermore studied the sub-detector's performance for the main data samples from 2016, 2017 and 2018, and have contributed to improvements in the software tools used to assess its efficiency.

The CEDAR/KTAG was designed to meet high performance requirements. The necessary time resolution for kaons tagged by the sub-detector is of the order of 100 ps, while the desired mis-tagging rate for pions is of the order of  $10^{-4}$ . At the same time, a kaon tagging efficiency above 95% is desired.

The CERN CEDARs principles of operation and the NA62 CEDAR/KTAG sub-detector are described in full detail in the present chapter, together with the preliminary procedures undertaken to ensure efficient data-taking, and the studies carried out in order to assess its performance after the data is collected.

## 4.1 CERN CEDARs principles of operation

The CERN CEDAR used in NA62 can separate kaons from pions up to 150 GeV/ $c$ , and can detect protons down to 12 GeV/ $c$ . [56]

The CEDAR is a Cherenkov detector; it thus exploits the physical phenomenon of emission of radiation by particles travelling through a medium at a speed larger than the one of light in the same medium. It is, moreover, a differential counter. This means that it is only sensitive to a specific range of angles of the emitted radiation by means of a mechanical diaphragm of fixed radius and variable annular aperture. In this way, light produced by particles of the desired mass can be selected. A Mangin mirror, as explained in section 4.2, focuses the Cherenkov light into a ring image at the diaphragm plane, regardless of the point of light emission along the particle's track. The diaphragm opening has variable size  $a_d$ ; any two rings can be separated if their radii are distant more than  $a_d$  from each other.

If one indicates by  $n$  the refractive index of the medium and by  $\beta$  the velocity of the

particle, the radiation is emitted in a cone described by an angle  $\theta$  which satisfies the relation:

$$\cos\theta = \frac{1}{n\beta} \quad (4.1)$$

where  $\beta$  is related to the mass  $m$  and momentum  $p$  of the particle according to the following expression:

$$\beta = \frac{p}{E} = \left[ 1 + \left( \frac{m}{p} \right)^2 \right]^{-\frac{1}{2}} \quad (4.2)$$

Therefore, in a monochromatic beam of momentum  $p$ , by tuning the pressure of the gas in the tank one can set the detector to be sensitive to particles of specific mass  $m$ , as the ring they produce can be set to be within the acceptance of the diaphragm.

The relation between a difference in the mass of the particles that produce the ring and the difference in the ring's radii can be derived as follows. Given two particles with different masses  $m_1$  and  $m_2$ , the relative difference in their velocity is:

$$\frac{\Delta\beta}{\beta} \approx \beta_2 - \beta_1 = \left[ 1 + \left( \frac{m_2}{p} \right)^2 \right]^{-\frac{1}{2}} - \left[ 1 + \left( \frac{m_1}{p} \right)^2 \right]^{-\frac{1}{2}} \approx \frac{m_2^2 - m_1^2}{2p^2} \quad (4.3)$$

By differentiating eq. (4.1) one finds:

$$\Delta\theta = \frac{1}{\tan\theta} \frac{\Delta\beta}{\beta} \approx \frac{1}{\theta} \frac{\Delta\beta}{\beta} \quad (4.4)$$

Indicating the focal length of the system by  $f$  and using the above results, one comes to the expression of the difference in the produced ring radii:

$$\Delta R = f\Delta\theta \approx \frac{f}{\theta} \frac{m_2^2 - m_1^2}{2p^2} \approx \frac{f^2}{d_r} \frac{m_2^2 - m_1^2}{2p^2}, \quad (4.5)$$

where the approximation  $\theta \approx d_r/f$  has been used, and  $d_r$  is the diaphragm radius.

Two particles can be separated if the rings they produce have radii differing by a quantity  $\Delta R$  larger than the diaphragm aperture  $a_d$ .

In NA62, the particles of interests are positive kaons and pions; therefore,  $m_1 = m_{K^+}$  and  $m_2 = m_{\pi^+}$ . The NA62 CEDAR has focal length  $f = 3.24$  m and diaphragm radius  $d_r = 100$  mm. Particles in the NA62 beam have average momentum  $p = 75$  GeV/ $c$ , with a root mean square (RMS) or *momentum bite*  $\Delta p/p \approx 1\%$ , which leads to  $\Delta R \approx 2$  mm.

**Temperature stability** The refractive index of a gas, and therefore the aperture of the Cherenkov cones of particles traversing it, varies with its density. The volume  $V$  of the gas in the CEDAR is fixed, and, as the tank is sealed, the number  $n$  of gas particles is fixed too. From the equation of perfect gases:

$$P = \rho RT, \tag{4.6}$$

where  $\rho = \frac{n}{V}$  is the gas particles density, it follows that, by keeping the pressure  $P$  and the temperature  $T$  constant across the whole gas tank, the gas density in the radiator will be uniform; therefore, the refractive index, and thus the aperture of Cherenkov cones for particles with the same  $\beta$ , will be fixed. Carefully monitoring these parameters is of primary importance in order to be able to effectively separate particles of different mass.

#### 4.1.1 Ring broadening effect

Ideally, particles of specific mass and momentum produce in the detector a narrow ring; in this case, one could minimize the light produced by undesired particles by setting a very small aperture for the diaphragm. In reality, Cherenkov rings are broadened through several mechanisms; therefore, using small diaphragm apertures results in loss of detection efficiency for the desired particles. Such mechanisms include chromatic dispersion, multiple Coulomb scattering, and beam divergence; they are described below. The CEDAR uses an Achromatic Ring Focus to correct for the majority of these effects. Poor alignment, described in section 4.1, causes a shift in the ring position rather than its broadening, as seen in fig. 4.13.

**Chromatic dispersion** Chromatic dispersion is the largest effect ascribable to the CEDAR that can broaden Cherenkov light rings, and it is due to the variation of the refractive index  $n$  with the light's wavelength.

The spread of the ring is:

$$\Delta R = f\theta \frac{1}{2\nu} \left( 1 + \frac{1}{\theta^2 \gamma^2} \right) \quad (4.7)$$

In the above expression,  $\nu$  is the Abbe number<sup>1</sup>, which is related to the gas dispersion, and the relativistic parameter  $\gamma$  contains the dependency on the speed of the particle. In particular conditions, for example for the purpose of separating kaons from pions, the dependence on the  $\gamma$  parameter can be neglected. It follows:

$$\Delta R \approx \frac{a_d}{2\nu} \quad (4.8)$$

Nitrogen at a pressure of 1.7 bar has an Abbe number  $\nu \simeq 35$ , leading to an increase in the root mean square (RMS) of the ring of  $\Delta R \approx 1.4$  mm.

Chromatic dispersion can be compensated through the use of a pair of chromatic correctors. The optical elements used by the CEDAR reduce  $\Delta R$  to approximately 0.13 mm. They are described in section 4.2.

**Multiple Scattering** One more ring-broadening effect, due to the CEDAR's material, is multiple scattering of beam particles travelling through the radiator gas. A charged particle travelling through a medium undergoes scattering from nuclei due to Coulomb interactions with them, and thus it is deflected many times on its path. For small deflection angles, multiple scattering is approximately Gaussian; it does not change the average direction of the particle, but, as the latter is varied at every collision, the emitted photons will have different direction, and as a consequence the Cherenkov rings will not be concentric. This results in a broadening of the latter. The broadening is given

---

<sup>1</sup> $\nu = \frac{n_D - 1}{n_F - n_C}$ , where  $n_D$ ,  $n_F$ ,  $n_C$  are the refractive indices of the gas at the reference wavelengths  $\lambda_D = 589.3$  nm,  $\lambda_F = 486.1$  nm,  $\lambda_C = 656.3$  nm.

by:

$$\sigma_R = f \frac{13.6 \text{ MeV}}{\beta c p} \sqrt{\frac{LP\rho_0}{3X_0P_0}} \quad (4.9)$$

In the above formula,  $L$  is the length of the radiator,  $P$  is its pressure, and  $P_0$ ,  $\rho_0$  and  $X_0$  are, respectively, the gas atmospheric pressure, and the corresponding density and radiation length. In the KTAG/CEDAR sub-detector  $\sigma_R = 0.06$  mm. The effect's size is fixed at this value if the CEDAR working parameters are homogenous.

**Beam divergence** An additional ring-broadening effect is not ascribable to the CEDAR; instead, it results from the divergence of the beam, and it is expressed as an average over a number of particles rather than affecting individual particles. The x and y divergence  $\sigma_{\theta_x}$  and  $\sigma_{\theta_y}$  are of the order of  $70 \mu\text{rad}$  [52], and thus contribute to increasing the ring RMS by a factor  $\sigma_R = f\sigma_{x,y} \approx 0.45$  mm.

## 4.2 The NA62 CEDAR/KTAG sub-detector's description

The CEDAR used in NA62 selects kaons in the  $75 \text{ GeV}/c$  momentum beam and can be filled either with nitrogen or hydrogen, although it is optimised for the former. [57]

Being a differential counter, the CEDAR collects light within a circular diaphragm of fixed radius. One can vary the pressure of the gas and thus its refractive index, changing the radius of the Cherenkov rings produced by beam particles of given mass and fixed momentum. By varying the pressure one thus effectively selects which particles and momenta will produce rings within the diaphragm acceptance, and therefore which particles the CEDAR is going to be sensitive to.

Beam particles coming from the target, assumed to be on the left in detector layout in fig. 4.1, enter the radiation vessel of the CERN CEDAR. The vessel is made of steel

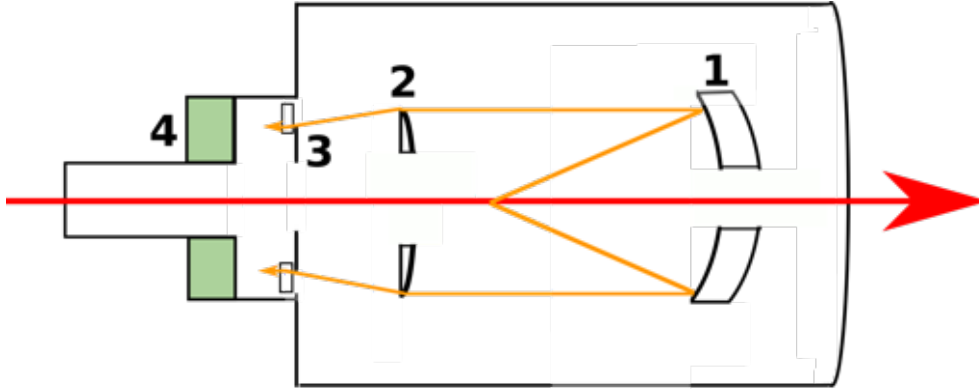


Figure 4.1: Schematic representation of a CEDAR vessel. The secondary beam, coming from downstream of the target, travels from left to right in this picture. The Cherenkov radiation, emitted by beam particles in the shape of a cone, first encounters a Mangin mirror (1), where it is reflected backwards in the form of rings onto the mirror’s focal plane passing through a corrector lens (2), used to correct chromatic dispersion. A diaphragm then selects light in a circular window. The latter is successively focused by 8 condenser lenses (4) onto 8 quartz windows. In the original CERN design, a photomultiplier tube (PMT) would be located at each quartz window (4). The photon detection and read-out system was upgraded for use in NA62.

and it is sealed at the ends by aluminium windows. The vessel’s length is  $\approx 5.5$  m and its external diameter is 55.8 cm, while the thickness of the aluminium windows is  $150\ \mu\text{m}$  for the upstream one and  $200\ \mu\text{m}$  for the downstream one.

Figure 4.1 illustrates the path in the CEDAR of Cherenkov light emitted by beam kaons. The beam particles traveling inside the gas emit cones of Cherenkov radiation. The produced light is reflected back, at the opposite end of the CEDAR, by a Mangin mirror, which design is based on a spherical mirror, improved to correct for spherical aberration; the mirror focuses the Cherenkov light into a ring image at the diaphragm plane, and it has a 30 cm diameter and a central 10 cm diameter hole for the beam.

As the photons travel back towards the upstream end of the CEDAR, they pass through a corrector lens, which has the same optical axis as the Mangin mirror and has a 15 cm diameter hole that allows the passage of light emitted at the upstream end of the vessel.

The combination of the Mangin mirror and the corrector lens are designed to correct chromatic dispersion in the rings. Once light has passed through the corrector lens, it

reaches the diaphragm. By construction, it is possible to vary its width from 0.03 mm to 2 cm with steps of 0.01 mm by moving both an inner and an outer set of 8 segments that describe eight elongated apertures.

The light that has passed the diaphragm is successively focused by 8 condenser lenses in spots onto a quartz window.

By design, in the CERN CEDAR, a PMT would be located in correspondence of each of these light spots. The number of photons emitted by a particle travelling in the radiator is given by the Frank-Tamm formula described in 4.2.3; for the CEDAR, in the range of wavelengths the sub-detector is sensitive to, and keeping into account the amount of light transmitted by the CEDAR optical elements, each kaon yields approximately 20 photons. 45 MHz of kaons therefore yield  $\approx 1$  GHz detected photons. As the maximum rate of photons that a single PMT can sustain is of the order of 5 MHz, it is clear that the photo-detection system used in the original CEDAR design, consisting in 8 PMTs, is unable to cope with such a high rate of particles and does not provide time resolution at the required level of 100 ps. A new photodetector and read-out module, the KTAG, that makes use of  $\approx$  hundreds light detection units, has therefore been designed and developed to be used in NA62 together with the CEDAR.

A schematic representation of the KTAG is provided in figure fig. 4.2.

The exact number of PMTs was chosen via MC simulations to be 384, to ensure the desired rate and resolution requirements were met. Because of their size, they need to be evenly distributed in eight groups, located around the beampipe and corresponding to the positions of the previous 8 PMTs; light then needs to be directed radially towards them. Simulations concluded that the best radial distance of the PMTs from the beampipe, that minimises radiation from muons and neutrons, is between 30 and 50 cm [57].

The Cherenkov radiation travels from each quartz window to an *optical cap* lens. It is successively focused onto a set of spherical mirrors held by a cylindric surface, where it is reflected radially. It eventually reaches eight *light boxes* or *sectors*. Between the light boxes and the mirrors there is a lightweight aluminium cylinder with holes to allow

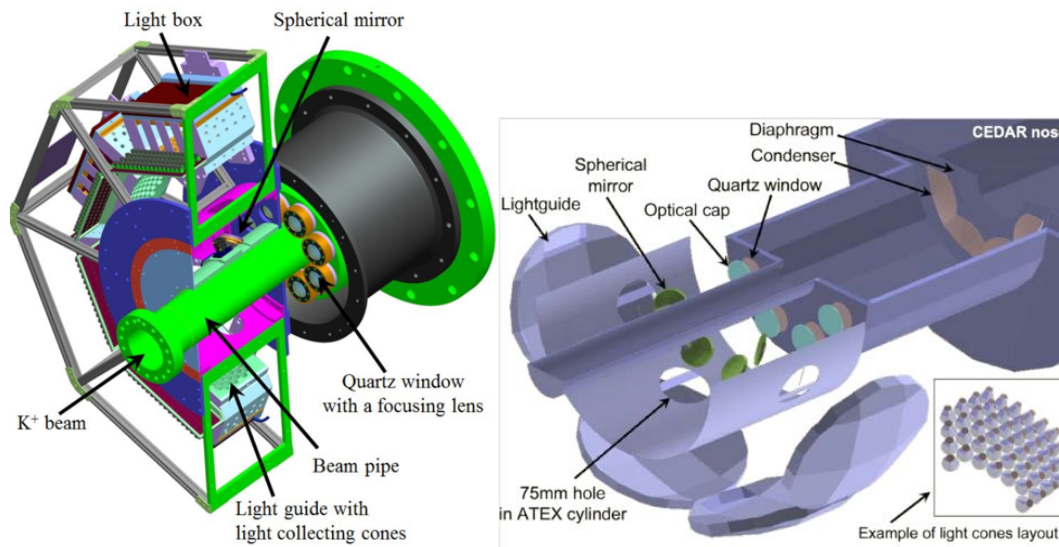


Figure 4.2: The light detection system of the KTAG sub-detector (left) and a detailed view of the KTAG upgrade (right), from Geant4 simulations performed by the CEDAR/KTAG group during the read-out and photo-detection upgrade. The original CEDAR light detection system with eight PMTs each located on one of the eight quartz windows has been replaced with the above system, which makes use of 384 PMTs, to cope with the particle rate at NA62.

the passage of light, which is matt black to absorb any scattered radiation and protects against optical cross-talk between different sectors. The radiation reflected by the mirrors reaches a light guide consisting in a 17 mm thick aluminium surface with a spherical section, on which 64 conical sections are evenly distributed to form a matrix. The centre of curvature of the aluminium plate matches the virtual focus of the light reflected in the spherical mirror. Each light guide can thus house a maximum of 64 cones; nonetheless, the number of cones per octant instrumented with PMTs has been fixed to 48, as this number already ensures that the KTAG reaches the desired performance. The total number of read-out channels is 384, the same as the total number of PMTs. Each of them counts photons at a rate of  $\sim 5$  MHz. The PMTs are placed into the outer curved surface of the light guide, matching the cones. The distribution of PMTs within a light guide is illustrated in fig. 4.3.

The optical cap lenses and the spherical mirrors distribute light across the PMTs in each lightguide. The shape of this distribution is affected by the optical characteristics of these elements. The optical caps are plano-convex lenses made of fused silica. The optimal

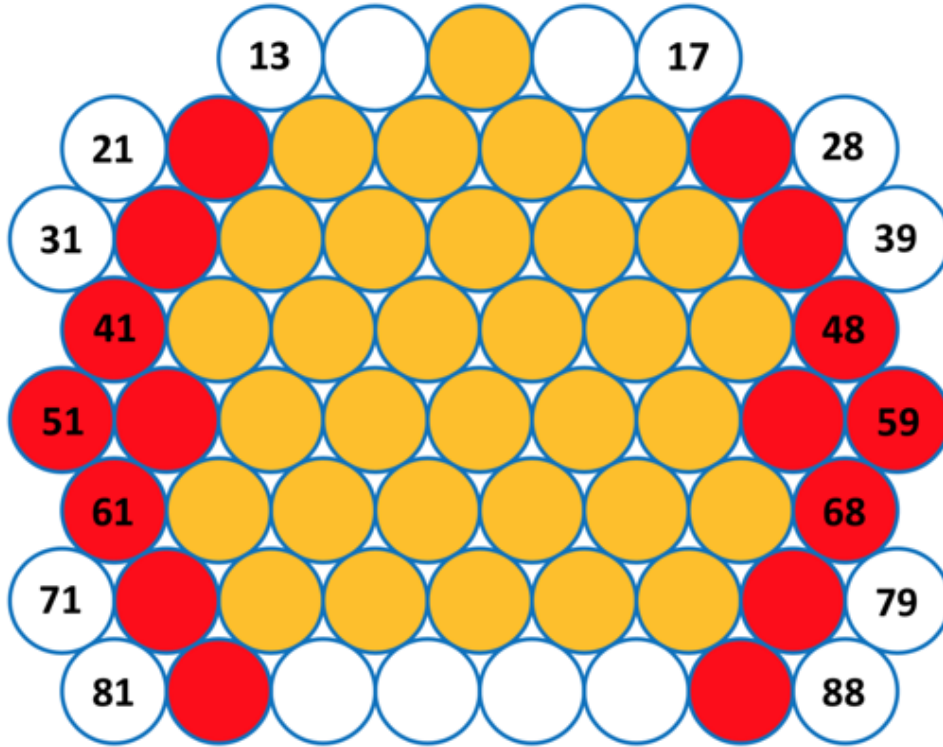


Figure 4.3: Distribution of PMTs (Hamamatsu R7400U-03 modules in red, R9880U-210 modules in yellow) in a light guide. [58]

focal length has been found, through simulating its impact on the light distribution for several different options, to be 250 mm. The optimal radius for the spherical mirrors has been found, through similar considerations, to be 114 mm.

The KTAG is constructed in two halves in order to facilitate its installation around the beamline; each half contains 4 light boxes. The two halves of the KTAG are supported by a cylinder, which is attached to the CEDAR end flange. The whole system is enclosed in an aluminium chamber which acts as a Faraday cage and is continuously flushed with nitrogen gas in order to keep all components free from dust and oxidation and preventing any hydrogen leak, should the sub-detector be filled with it, turning into a hazardous build-up.

The detector is operated at room temperature, and the pressure can be set to any value between vacuum and 5 bar. For the 2015 - 2018 data-taking periods, the NA62 CEDAR has been filled with nitrogen gas ( $N_2$ ) at 1.75 bar, which corresponds to  $3.5 \times 10^{-2}$  radiation lengths of material to be traversed by beam particles. As an alternative, it is possible

to use hydrogen gas ( $H_2$ ) at 3.9 bar. In the latter case the number of radiation lengths decreases to  $7 \times 10^{-3}$ . The illumination of the diaphragm, as a function of the radius across its aperture, and the light's wavelength, is shown, for  $N_2$  and  $H_2$ , in fig. 4.4. Light dispersion has been corrected for use with  $N_2$ , therefore ensuring, as it can be seen, a sufficient separation between kaons (left hand side of the distribution) and pions (right hand side). Worse discrimination is achieved with  $H_2$ . In the plots, the dashed vertical line indicates the fixed diaphragm radius, whereas the solid lines indicate a diaphragm aperture of  $\approx 1.5$  mm; when operating the sub-detector with hydrogen gas, the loss of light from kaons at this aperture is  $\approx 30\%$ . In the 2016-2018 data-taking periods, the diaphragm aperture was set to 1.3 mm. In order to achieve the required level of pion contamination in hydrogen, one must reduce the diaphragm aperture, undergoing a loss of 40% of the Cherenkov light from kaons. This would not affect the time resolution to a large extent, as it will still be below the desired value, but may significantly impact detection efficiency. Enlarging the diaphragm to increase the light yield from kaons would result in a pion contamination above the accepted level. Both parameters are discussed in section 4.2.3. Performing a pressure scan (the procedure, described in section 4.3, to set the optimal pressure point that maximises light yield for kaons) has also been proved, via MC simulations [59], to be particularly difficult when using hydrogen, as the kaon and pion peaks will not be well separated. Furthermore, much stricter safety procedures would need to be carried out in case of usage with hydrogen.

The KTAG is equipped with a blue LED which can illuminate a set of optical fibers directed each onto one of the spherical mirrors. The LED, which has an adjustable light intensity and a variable input current, is meant to be used to perform tests without the particle beam. The sub-detector makes use of a chiller which flushes distilled water under pressure through the heat-sinks on the outside of each light box. Furthermore, both the CEDAR and the KTAG are protected by insulating covers against the occurrence of fire.

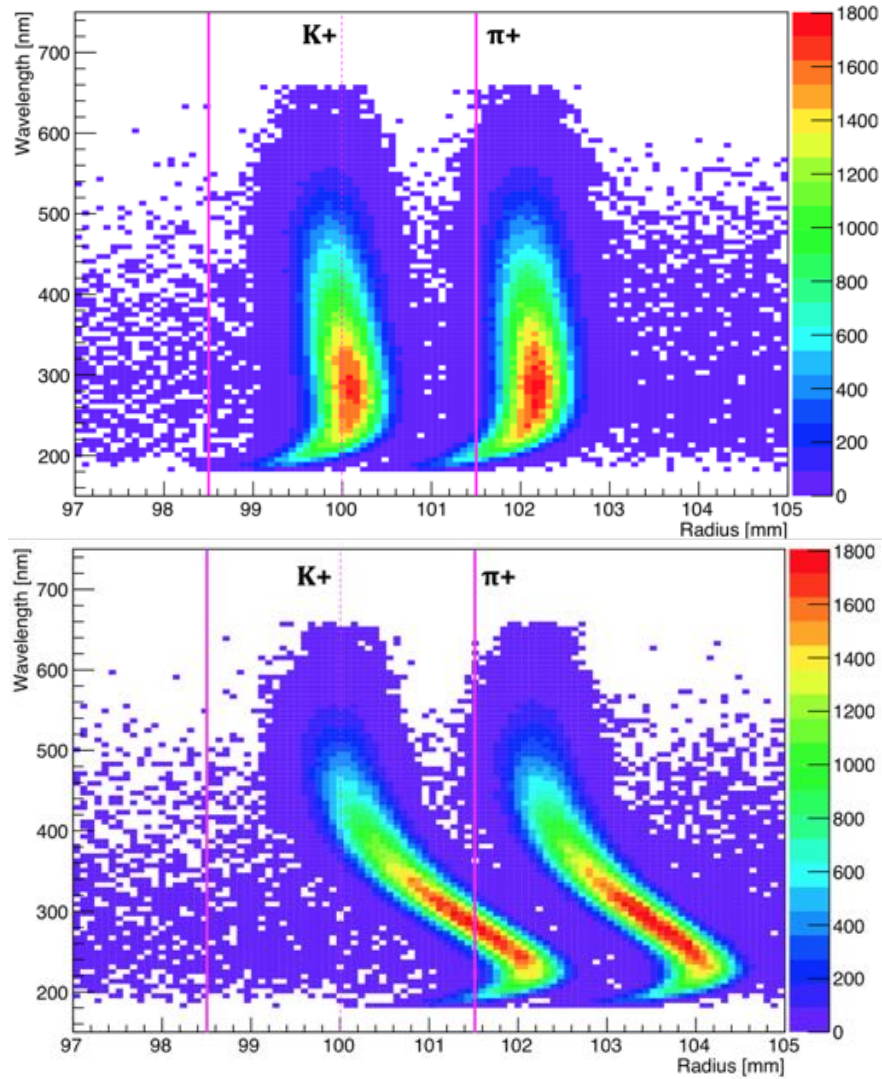


Figure 4.4: Diaphragm illumination for all wavelengths and for a radius varying across the aperture for  $N_2$  (top) and  $H_2$  (bottom) for a CERN CEDAR W. The left hand side of the distributions is mostly produced by kaons, whereas the right side is mostly produced by pions. The dashed line indicates the (fixed) diaphragm radius, whereas the solid lines indicate a reference aperture of  $\approx 1.5$  mm. Because the CEDAR is optimised for use with  $N_2$ , in this case better separation between pions and kaons is achieved; at the indicated aperture, about 30% of light from kaons is lost when using hydrogen gas. [57]

### 4.2.1 The KTAG's PMTs

The KTAG uses two different types of PMTs, both manufactured by Hamamatsu<sup>TM</sup>, and capable of detecting a single photon while being exposed to a high rate of particles. In each sector, thirty-two modules are of R9880U-210 type and sixteen are of R7400U-03 type. The R7400U-03 modules were used first in 2012 Technical Run, whereas the R9880U-210 modules were instrumented for the first time in the 2014 data-taking. Both tubes have cylindrical shape of 16 mm  $\times$  12 mm dimensions, a time resolution of the order of 300 ps and a dark count rate of a few Hz, while they differ in their quantum efficiency and gain. The former model has a 20% peak efficiency and 8 dynodes, resulting in a gain of  $1 \times 10^6$ ; the latter has a 40% peak quantum efficiency and 10 dynodes, resulting in a gain of  $2 \times 10^6$ . For the position of the two types of PMTs within a sector one can refer to fig. 4.3, where the R9880U-210 type is coloured in yellow and the R7400U-03 type is coloured in red. The choice of such distribution is motivated by the fact that most of the light reaches the central region, and therefore higher efficiency is more beneficial in that area. The operational tension is 900 V for both types and the output signal is converted into differential form by a custom printed circuit board (PCB).

### 4.2.2 The KTAG's read-out and reconstruction

The analogue signals coming from each PMT are converted to digital form and read-out by the system described below.

**Front-end electronics** The detection of a photon at the anode of a PMT produces a charge of about 240 fC, corresponding to a voltage signal with a 10 mV amplitude and with a rise time of the order of 1 ns. The voltage analogue signal needs to be converted to a digital signal that provides information about the photon's arrival time. This task is performed by NINO application-specific integrated circuits (ASICs), discriminators with differential input, which have very low jitter ( $\approx 60$  ps) and therefore contribute little to



Figure 4.5: Prototype of a front-end board, with 64 analog differential inputs (indicated by the letter A), 64 differential outputs (indicated by the letter B) and an ELMB (indicated by the letter C), equipped with 8 mezzanines with 1 NINO ASIC each (indicated by the letter D).

the sub-detector's time resolution (discussed in section 4.2.3). NINO circuits are housed on mezzanine boards, designed and constructed by CERN. One mezzanine board is used for each sector or light box. The eight mezzanine boards are housed on a front-end board, designed by the Birmingham NA62 group and constructed at the Rutherford-Appleton Laboratory (RAL); a prototype is shown in fig. 4.5. The threshold can be set remotely and independently for each NINO mezzanine board. The front-end board, which has 64 analog differential inputs and 64 differential outputs, also contains two *Control Area Network* (CAN) bus connectors to communicate with the *Detector Control System* (DCS) through the *Embedded Local Monitoring Board* (ELMB).

The signal fed to the NINO ASICs was derived from a custom-made voltage divider with a differential output which reads the signal from the PMT's anode and its last dynode. The new voltage divider has large noise reduction and increased total resistance, thus reducing heat production. The NINO circuits convert the analogue signal into a *Low Voltage Differential Signal* (LVDS) whose amplitude is proportional to the length of time the voltage signal is above a specified threshold; this is indicated as Time-Over-Threshold

(TOT) mode. The rising time of the signal above the threshold is called *leading edge*, whereas the falling time is called *trailing edge*.

As the gain varies significantly across the different types of PMT, the threshold must be chosen to ensure an inefficiency for each individual PMT below a few percent, at the same time satisfying the requirements on time resolution. The bias voltage of 100 mV has been found to produce, via the relation  $Q = V/f$  with  $f = 4\text{mV/fC}$ , a charge threshold that satisfies the aforementioned criteria. Reflections of the signal along the cable are possible if the input impedance is not optimised. For the NINO mezzanines reflections have been minimised; a single residual reflection is observed 4 ns away from the main signal. This produces a secondary peak in the distribution of the time-over-threshold, corresponding to events for which the signal is above threshold for a longer time because its reflection is above threshold as well. This effect is shown in fig. 4.6 and discussed in more detail later in this sub-section.

**Read-out electronics** The LVDS signals are then transferred to passive splitter boards, which redistribute them over non-adjacent read-out channels in order not to overload single channels and latency buffers shared by groups of channels. In order to ensure a detection inefficiency below a few percent, the rate per channel must, in fact, be kept below 5 MHz, whereas each group of 8 adjacent channels must receive a rate below 30 MHz. To cope with these limitations, in the KTAG only one out of every group of 8 channels is used. The signals are then fed by the splitters as input to 128 channel TDC boards (TDCB), which have been specifically designed for the NA62 experiment, and make use of one ALTERA Cyclone III FPGA and four High Performance Time to Digital Converter (HPTDC) chips to convert both leading and trailing edges into timestamps. The timestamp information allows for offline correction of the effect due to signals of different heights rising above threshold at different times, by employing the correlation between the width and the height of the signal (*slewing corrections*).

The TDCs are housed on TEL62 boards, common to most NA62 sub-detectors, which

are upgraded versions of the TELL1 [60] board used by LHCb. Both the TDCB and the TEL62 boards are described in more detail in chapter 3. Each TEL62 contains 4 TDC boards, and each TDC board contains 4 TDCs, each one corresponding to 32 channels, of which only 1 in each group of 8 are used for the reasons explained above. The total required number of channels, corresponding to all PMTs, is 384, or 48 per sector. In order to accommodate them, one therefore needs 6 TEL 62s:  $6 \text{ (TEL62)} \times 4 \text{ (TDC boards)} \times 4 \text{ (TDCs)} \times 4 \text{ (channels)}$ .

**Reconstruction** The ID of the read-out channel corresponding to the hit PMT, the type of signal (leading or trailing), and the recorded timestamps, in units of 97 ps, are encoded in a *data word*. The CEDAR/KTAG reconstruction, which is part of the NA62 software framework, reads this information, and produces a hit for every signal with both leading and trailing edge times, assigning to the signal a width given by the difference between these two times. Once all hits in a specific event have been produced, kaon candidates are constructed, and their time and number of hits and sectors are evaluated. Each candidate must be built starting from at least one hit, and hits are assigned to different candidates according to the response of a time-clustering algorithm. In the left-hand-side of fig. 4.6, the distribution of the time-over-threshold is shown.

One can notice the presence of a secondary peak, corresponding to the detection of residual reflections (*after-pulses*) produced by large signals. These are shown to not be a cause for concern by the plot on the right-hand-side, where the latency, defined as the difference between reconstructed mean hit time and kaon candidate time, is plotted against the time width.

The plot shows that latencies for large signal widths are negligible and thus do not affect the PMTs' time resolution.

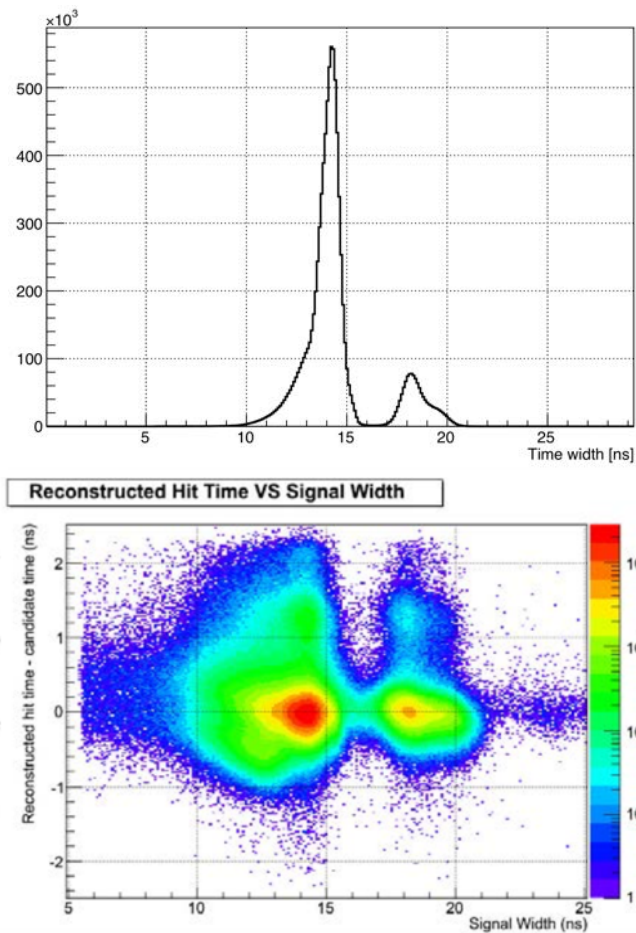


Figure 4.6: In the left-hand-side plot, the distribution of the width of signals recorded by the KTAG's read-out is displayed. [57] The width is defined by the difference of the leading and trailing edge times. In the distribution, one can notice the presence of a secondary peak, due to after-pulses above threshold. These are small enough to not affect time resolution, as shown by the plot on the right-hand-side [61], where the latency is plotted as a function of time width.

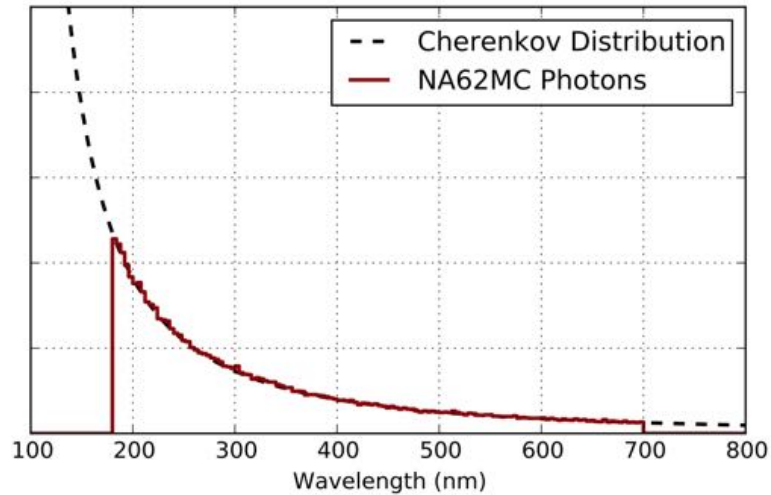


Figure 4.7: Wavelength distribution of the Cherenkov photons as given by the Frank-Tamm equation (dashed line), overlapped to the spectrum of photons produced by GEANT4 in nitrogen for the wavelengths range of interest for NA62 (solid line).

### 4.2.3 Light spectrum, detection efficiency and time resolution

**Light spectrum** If  $\alpha$  is the fine structure constant, the number of Cherenkov photons emitted per unit length  $dx$  and unit wavelength  $d\lambda$  by a charged particle travelling in a medium with refractive index  $n$  is described by the Frank-Tamm equation:

$$\frac{dN}{dx d\lambda} = 2\pi\alpha \frac{1}{\lambda^2} \left( 1 - \frac{1}{\beta^2 n^2} \right) \quad (4.10)$$

In nitrogen, the condition  $n > 1/\beta$ , denoting the regime at which a particle emits Cherenkov radiation (as follows from eq. (4.1)), is satisfied by all wavelengths between 100 nm and 1000 nm. The light distribution predicted by the Frank-Tamm equation over this range is illustrated in fig. 4.7, where it is overlaid with the spectrum of photons that are produced by GEANT4. As the sub-detector is only sensitive to wavelengths between 180 and 700 nm, simulation of photons emitted outside this range is not necessary.

The spectrum of the light reaching the PMTs also depends on the transmittance and reflectivity of the optical components, in particular the eight quartz windows, the optical cap lens and the mirrors. On top of these, one should take into account the quantum efficiency of the PMTs.

**Detection efficiency** The photon detection efficiency by one of the 8 sectors of the KTAG can be found using the Poisson distribution. Indicating by  $\Phi$  the mean number of photons detected by a sector, the probability of not detecting any photon is:  $\frac{\Phi^0 e^{-\Phi}}{0!} = e^{-\Phi}$ . It follows that the efficiency of a sector, that is the probability for a sector of detecting at least one photon, is:  $\eta = 1 - e^{-\Phi}$ .

Thus, if one makes the assumption that the eight sectors are identical, the probability of coincidences in  $n$  sectors ( $n$ -fold) are:

$$P(n\text{-fold}) = \binom{8}{n} \eta^n (1 - \eta)^{8-n} \quad (4.11)$$

The probability of having at least  $n$  coincidences, that is the cumulative efficiency, is:

$$\eta_n = \sum_{x=n}^8 P(x\text{-fold}) \quad (4.12)$$

The kaon detection efficiency depends, through  $\Phi$ , on the diaphragm width; care should be put in the choice of its value, as a larger diaphragm also implies a higher contamination from pions. For a diaphragm width 1.5 mm, the detected light due to kaons and pions is shown in fig. 4.8.

For a kaon travelling through the CEDAR, one expects 2.25 photons to be detected by each sector of the KTAG, or 18 photons in total. It is possible to observe the efficiency  $\eta_n$  for a number of required sectors  $n = 1, \dots, 8$  as a function of the average number of photons per sector  $\Phi$ . In fig. 4.10 the kaon tagging inefficiency is shown as a function of the number of expected photons when coincidences in 5, 6, 7 and 8 sectors are requested.

**Time resolution** The number of detected photons per kaon also plays a role in the time resolution of the detector, which is essential for matching to the downstream decay products. As previously mentioned, photons are emitted as beam particles travel through the radiator, and are reflected backwards by a mirror at the downstream end of

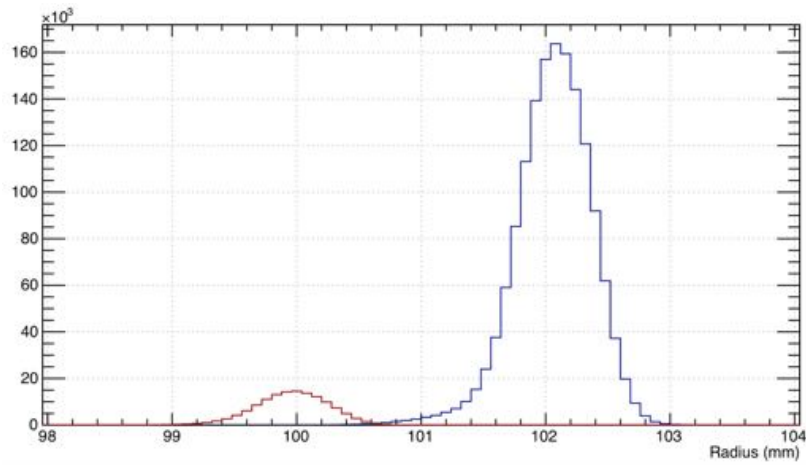


Figure 4.8: MC distribution of the radial position of detected Cherenkov light from kaons (red) and pions (blue) at the CEDAR diaphragm, normalized to the expected flux of kaons and pions in the beam composition. [57]

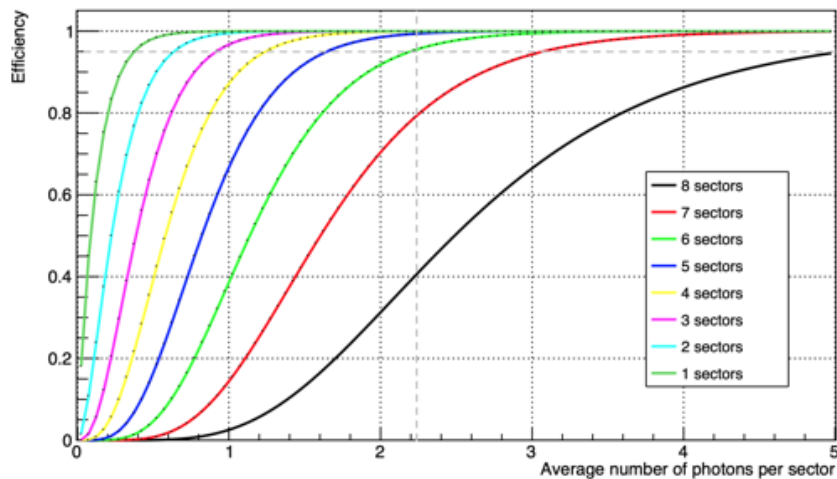


Figure 4.9: Kaon detection efficiency, for varying number of sectors required in coincidence, as a function of the average number of detected photons per sector. The latter number, corresponding to the vertical grey dashed line, is about 2.25. An efficiency of 95% is indicated by a horizontal grey dashed line. It is possible to observe that requiring six sectors in coincidence grants an efficiency above 95%.

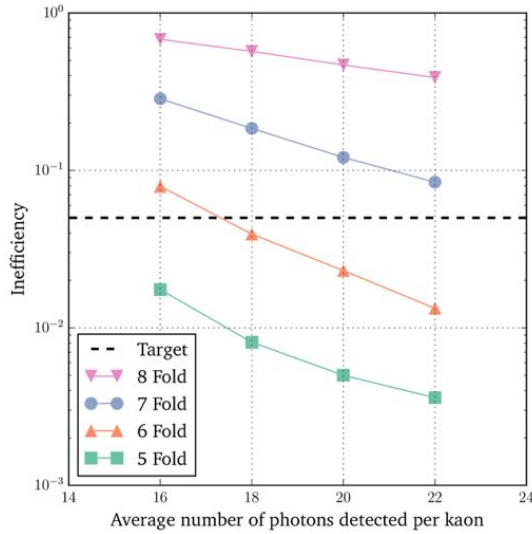


Figure 4.10: Kaon tagging inefficiency as a function of the number of expected photons when 5, 6, 7 and 8-fold coincides are requested. The dashed line indicates an inefficiency of 5%. [62]

the vessel. The photons will reach the light detectors at similar times, with the spread of the distribution, being  $\approx 10$  ps, due to the fact that beam particles travel faster than the emitted light in the CEDAR gas. Assuming the resolution on the arrival time of a photon is  $\sigma_{T,\gamma}$  and the number of detected photons is  $N_\gamma$ , then kaon time resolution  $\sigma_{T,K}$  is:

$$\sigma_{T,K} = \frac{\sigma_{T,\gamma}}{\sqrt{N_\gamma}} \quad (4.13)$$

The time resolution of the Hamamatsu PMTs used in the KTAG, described in section 4.2.1, is of the order of 300 ps. The contribution from the front-end electronics, discussed in section 4.2.2, is of the order of 60 ps. From equation eq. (4.13) it follows that the global time resolution for kaon crossing is  $\approx 70$  ps.

It is useful to study the time response of each PMT, by comparing its hit times with the hit-time distribution produced taking into account all other PMTs. This may be required, for example, in order to determine the most efficient time window for the reconstruction of a single kaon candidate.

The ideal time response of a PMT, containing the majority of the events, is a gaussian peak, which is due to the electrons travelling on different paths from dynode to dynode

according to their different velocities and to where the original photons impinged on the cathode; however, several effects arise that deviate the observed distribution from the ideal case. They include:

- Extreme paths taken by electrons that end up in inhomogeneous regions of the electric field. These undergo a smaller acceleration and result in a delayed Gaussian multiplied by an exponential distribution producing a long tail;
- Elastic forward scattering undergone by some electrons at the first dynode. These will produce an early Gaussian as they will have received a kick giving them a larger velocity and will arrive early on the following dynodes;
- Electrons which are back-scattered at the first dynode and are then accelerated and proceed to produce the normal cascade, results in a delayed pulse. The delay is equal to twice the time it takes an electron to travel between the first and the second dynode.

The timing response distributions discussed above are shown in fig. 4.11. The cumulative effect of the first two of the above mechanisms is to a good approximation a gaussian distribution peaked at the same value as the regular distribution; including in the third mechanisms in the cumulative distribution adds a secondary peak around 1 ns. the main peak and overlap with it to a good extent.

In the CEDAR/KTAG subdetector, it is possible to estimate KTAG's time resolution without the need of an external time reference. The determination of the crossing time for each kaon is based, in the NA62 Reconstruction framework, on the construction of a *candidate* starting from *hits* recorded in all the PMTs; the candidate time is calculated as an average of the hit times participating in its construction. The PMT's time resolution can be therefore estimated from the residuals of hit times with respect to the candidate time. The global time resolution can then be derived from the latter dividing it by the square root of the number of hits. As the average time is found using the individual hit times, this method will be slightly biased; the correction, though, has been estimated to

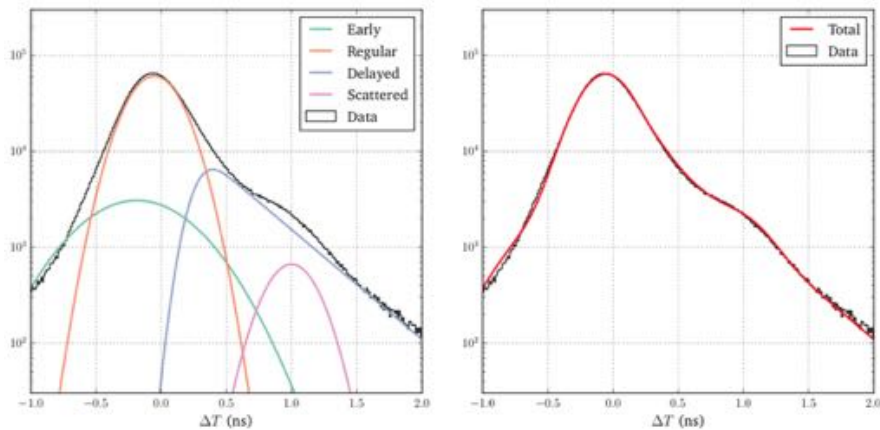


Figure 4.11: Timing response distribution for a single PMT. On the left, the different contributions to the total distribution are shown: in green, the early electrons that have been forward-scattered at the first dynode; in orange, the normal distribution due to electrons taking different paths in the detector; in blue, a delayed Gaussian with a long tail produced by electrons travelling in inhomogeneous regions of the electric field; in pink, the delayed Gaussian corresponding to back-scattered electrons at the second dynode. On the right, the total distribution arising from all of these effects can be observed (red line). In both plots, data is shown as well (black line). [62]

be negligible. The time resolution estimated with this method lies, as expected, in the range between 60 and 70 ps.

### 4.3 Procedures, monitoring and performance assessment

For the CEDAR/KTAG, several procedures need to be performed at different stages of its operation. In particular, the sub-detector must be correctly set-up for data taking; its behaviour must be monitored at run-time to quickly notice and act on any issue; and its performance and the quality of data need to be studied offline once the data has been collected. As part of my PhD work, I have been involved in all these three aspects. I have been in charge, as detector expert, of ensuring a correct set-up and operation of the sub-detector during several data-taking periods across the years 2016-2018. I have moreover been responsible for monitoring the quality of data, and have contributed to improvements in the software tools used to perform this task.

### 4.3.1 Preliminary procedures for data-taking

Before any data-taking periods, one must ensure that the sub-detector is correctly prepared for an efficient and smooth operation. The two leading requirements are an efficiency for positive identification of kaons above 95% and a pion mis-identification probability, that is the probability that an observed KTAG coincidence in 4 sectors at the kaon working pressure is produced by a pion, below a value of  $10^{-4}$ . As shown by simulations, the latter probability in the CEDAR/KTAG is at least two orders of magnitude smaller than the indicated upper limit, so the driving parameter for optimal KTAG settings is the kaon detection efficiency. In order to ensure that the above requirements are met, two main operations need to be carried out; namely, setting the correct gas pressure and adjusting the alignment between the vessel and the beam. Both operations are described in the present section.

#### Alignment

When operating the sub-detector, one must ensure the inefficiency for positive kaon identification is below 5% and the pion mis-identification rate is below  $10^{-4}$ . A mis-alignment between the average beam direction and the optical axis of the CEDAR affects the identification performance. [62]. Angular misalignment, defined by the CEDAR optical axis and the beam axis forming an angle, would decrease the detection efficiency for kaons and would increase the contamination due to pions. A spatial offset between the axes, provided that they are parallel to each other, does not affect the sub-system's performance.

The alignment of the CEDAR is performed by rotation of the vessel. The latter is supported under the quartz windows at the upstream end, and in two more points under the Mangin mirror at the downstream end. The downstream supports are two chariots placed on a V-shaped surface that can be moved through motors in the x and y directions.

A graphic interface hides the control of the motors' movements from the user, allowing then to set directly the position of the downstream end of the CEDAR with respect to a reference point (not corresponding to any specific position). The misalignment is therefore

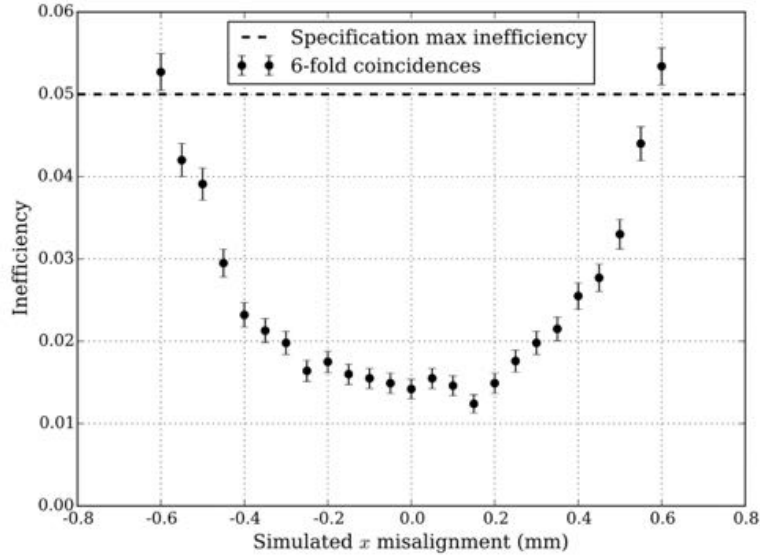


Figure 4.12: The points show the CEDAR/KTAG inefficiency for 6-fold coincidences for MC samples with different  $x$  misalignment. The dotted line shows the maximum tolerated inefficiency. [62]

expressed as a spatial distance from the ideal position rather than the angle formed by the two axes. The relation between the spatial and angular misalignment, making use of the small angle approximation, is the following:

$$\begin{aligned}\Delta x &= L \tan \Delta \theta_x \approx 4.347 \times \Delta \theta_x \\ \Delta y &= L \tan \Delta \theta_y \approx 4.347 \times \Delta \theta_y\end{aligned}\tag{4.14}$$

The motors can move by a maximum of 4 mm on either side for both  $x$  and  $y$  coordinates, with a step size of  $10 \mu\text{m}$  or equivalently  $2.3 \mu\text{rad}$ .

In figure fig. 4.12 one can observe the kaon identification inefficiency for MC samples with varying simulated  $x$  misalignment when requiring coincidences in at least 6 sectors. One can see that a mis-alignment smaller than 0.6 mm is necessary in order to keep the efficiency for 6-fold coincidences above 95%.

The tool used to assess the quality of the alignment is the experiment's Online Monitor (OM), described in more detail in section 4.3.2, which gives fast feedback about the data as it is collected. It is therefore possible to estimate the goodness of any adjustment in real time and iterate the alignment procedure until the desired result is obtained.

The number of steps it takes to reduce the residual misalignment below the desired level depends on how well the true misalignment is estimated; it is important therefore that the chosen procedure is able to provide accurate estimates in order to reduce the number of iterations.

**The traditional procedure** The traditional procedure used to align the CEDAR exploits the distribution of light in the eight sectors of the KTAG. By grouping the sectors in pairs, one ends up with four groups or *quadrants*. One can then define the left/right (L/R) and up/down (U/D) asymmetries as:

$$A_{L/R} = \frac{N_L - N_R}{N_L + N_R}, \quad A_{U/D} = \frac{N_U - N_D}{N_U + N_D}. \quad (4.15)$$

where  $N_L$ ,  $N_R$ ,  $N_U$ ,  $N_D$  represent the number of hits in each quadrant. If one makes the assumption that the PMTs and the quartz windows are identical, in case of perfect alignment the number of hits is the same in each sector, and therefore both asymmetries are exactly null. A non-null value of the asymmetry can be generated by a misalignment of the vessel. A schematic example can be found in fig. 4.13, where a misalignment of the vessel with respect to the beam axis in the  $y$ -direction produces an up/down asymmetry. A misalignment can, though, also arise from the different performance of PMTs or other optical components; the latter effects must be corrected for before using the asymmetries to align the sub-detector.

In order to know in which direction the CEDAR should be rotated in order to improve the alignment, it is sufficient to know the sign of the asymmetry provided by the OM. The magnitude of the necessary correction is derived from calibration curves constructed by fitting the distribution of asymmetry for MC samples with varying simulated misalignments. The curves can be then used to estimate misalignment based on measured asymmetries provided by the OM. The shape of the asymmetry curves depends on the diaphragm shape and aperture. An example of calibration curves for left/right

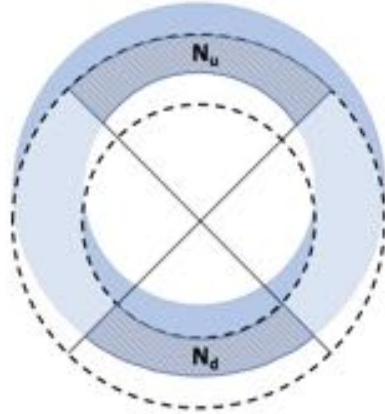


Figure 4.13: Example of misalignment in the CEDAR. In this figure, the beam has a vertical misalignment with respect to the CEDAR optical axis. The diaphragm aperture is represented by the dashed line, whereas the photons emitted by beam particles are coloured in blue. One can see that the number of lost photons is larger for the bottom quadrant than the top one, that is  $N_u > N_d$ , thus leading to a non-null value of  $A_{U/D}$ .

and up/down asymmetries for a diaphragm aperture of 1.5 mm can be found in fig. 4.14. Using these curves, misalignment can be estimated with a precision of a few hundreds of  $\mu m$ .

The procedure that was just described, based on the study of asymmetries, was tested on MC. When null misalignment is estimated by the simulation, the CEDAR detector was found to be perfectly aligned. However, for non-null values of simulated misalignment, the amount of CEDAR misalignment is not always correctly estimated. Several iterations are therefore required to reach a correct alignment. It was furthermore observed that the asymmetries are sensitive to the beam's angular profile, and therefore a method based on information coming from all PMTs within a full simulation framework would yield a more robust estimate.

**Full MC simulation procedure** The full MC simulation procedure was performed by Francis Newson and makes use of all the information available about the distribution of light in the PMTs. It employs the following figure of merit:

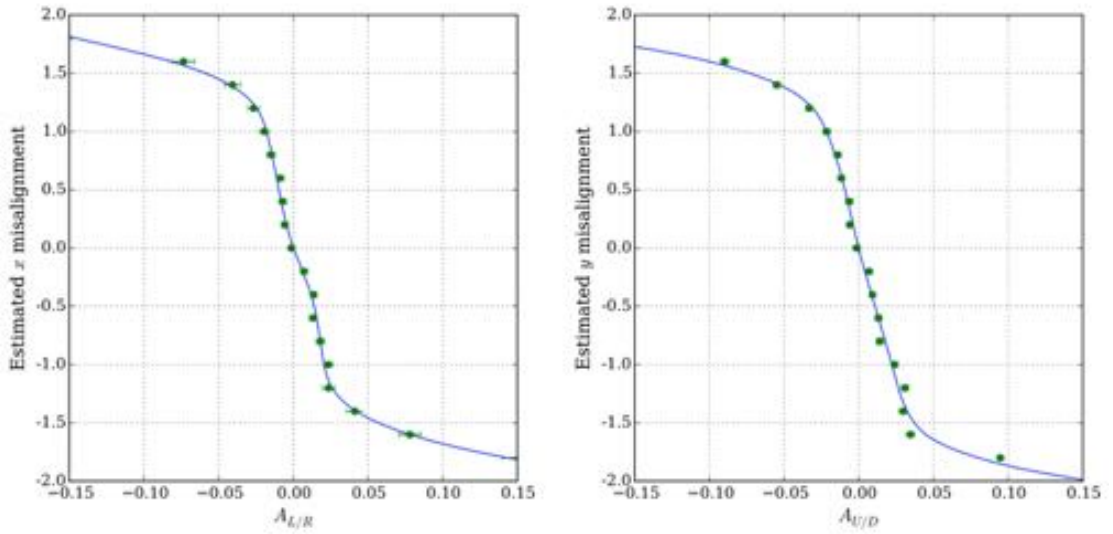


Figure 4.14: The blue lines in the plots are the calibration curves for left/right (left hand side) and up/down (right hand side) asymmetries for a diaphragm aperture of 1.5 mm, constructed from the asymmetries estimated in samples of known misalignment (green dots). Knowing the asymmetries, it is thus possible to obtain from these curves an estimate of the CEDAR’s misalignment. Misalignments are expressed in mm. [62]

$$\chi^2 = \sum_i \frac{(d_i - r m_i)^2}{d_i + r^2 m_i} \quad (4.16)$$

where the index  $i$  represents each of the PMTs, or alternatively a group of them. In the former case  $d_i$  represents the number of photons detected by each PMT in data,  $m_i$  is the number of photons found in MC and  $r$  is a scale factor:  $r = \sum_i d_i / \sum_i m_i$ . In the latter case,  $d_i$  and  $m_i$  are the total number of photons detected by PMTs belonging to the same group, for data and MC.

Given a data sample consisting in the hit distribution in each PMT or group of PMTs, several MC templates corresponding to light distributions for specific values of misalignment can be tested by computing the value of  $\chi^2$  for the (data, MC template) pair. From the template for which  $\chi^2$  is smallest one can thus infer the best estimate of the CEDAR’s misalignment.

The grouping of PMTs for the purpose of aligning the sub-detector must be chosen with the goal of obtaining a trade-off between high granularity of the distribution (achievable by grouping few PMTs together) and small sensitivity to variations in the PMTs efficiency

(achievable by grouping many PMTs together). Before data events are used to estimate the CEDAR's alignment, a selection needs to be applied to clean-up the data samples from background due to other particles in the beam, in particular pions. An efficient criterion is to select events that have in-time hits in the PMTs in at least 5 sectors.

### **Pressure scan**

As discussed at the start of the present chapter, the radii of the Cherenkov rings produced by beam particles depends on the refractive index of the gas, and thus on its pressure. One must ensure that the radii of the kaon rings is such that they pass through the diaphragm slit, thus maximizing the accepted light from kaons and reducing the light from pions and other background particles. The correct pressure value for the CEDAR gas corresponds to the point, in the kaon peak region (approximately between 7.2 and 1.8 bar), at which the number of 5, 6, 7 and 8-fold coincidences is maximum.

A misalignment of the KTAG may translate into an incorrect working pressure estimate. Similarly, an incorrect pressure estimate causes finding the minimum in an alignment procedure to be more difficult. To ensure that both the pressure and the alignment are correct, one must perform several iterations alternating pressure scan and alignment until a good configuration is achieved. The value of pressure in the CEDAR can be set to any value between vacuum and 5 bar. The pressure scans performed during 2015 and 2017 data-taking periods are provided in fig. 4.15 and fig. 4.16. A small change in pressure, of the order of 0.01 bar, does not affect the number of coincidences; for this reason, a pressure scan is only performed again after a period of shutdown, or when the beam parameters are changed.

### **4.3.2 Online data monitoring**

As previously mentioned, the NA62 experiment makes use of an OM that is available, during data-taking, to all shifters and detector experts. The OM, which consists of a

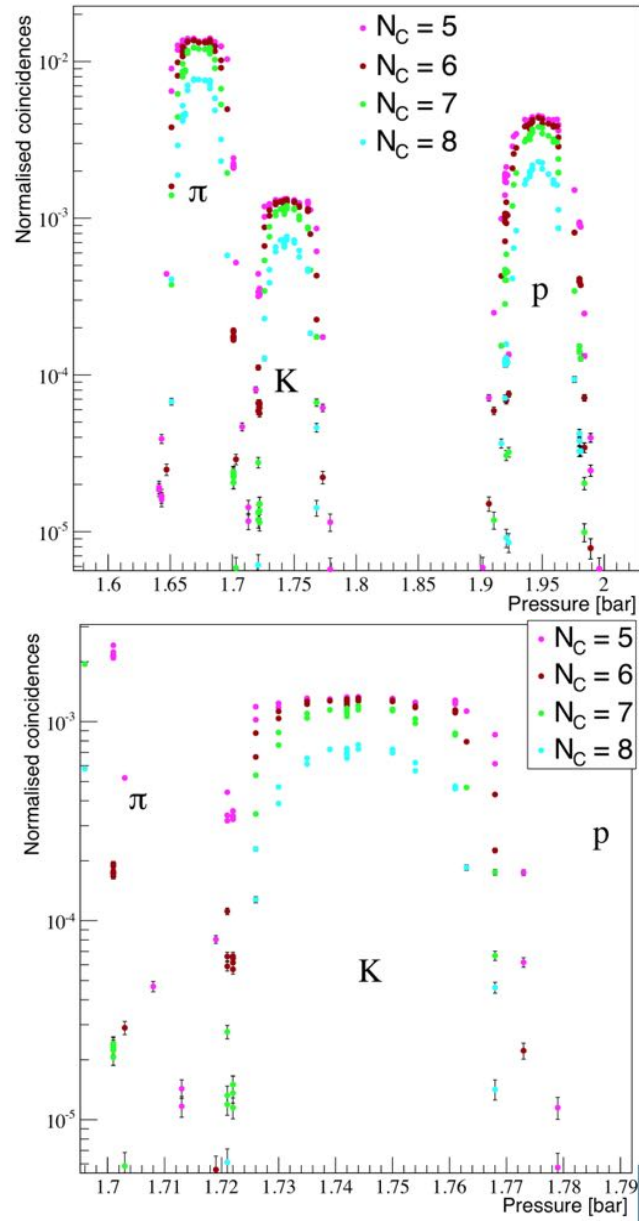


Figure 4.15: Pressure scan plot for 2015 data taking, for a pressure varying between 1.6 bar and 2 bar (top) and zoomed around the kaon peak (bottom), for a number of coincidences in 5-8 sectors. [63]

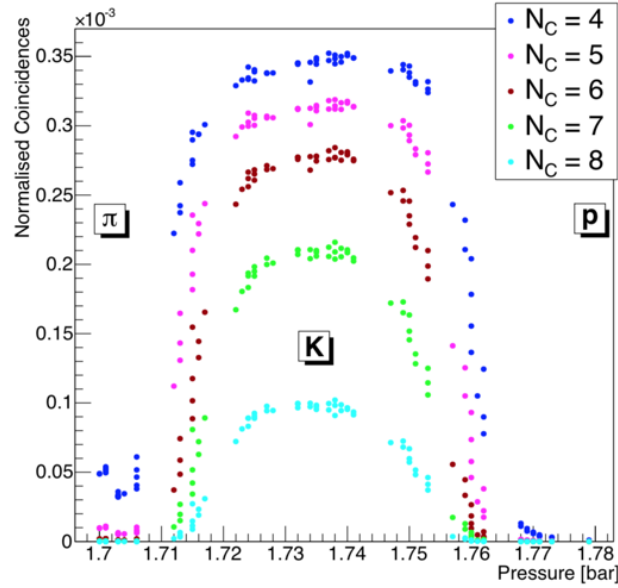


Figure 4.16: Pressure scan plot for 2017 data taking, for a pressure varying between 1.7 bar and 1.78 bar, for a number of coincidences in 5-8 sectors. [63]

collection of tabs containing plots that are updated every few SPS spills, provides information on the status of the hardware and readout of all sub-systems for prompt reaction following any anomalous behaviour. The CEDAR/KTAG monitoring tools are described in this section.

**Channel profile** The channel profile plots on the OM show the illumination of each PMT in each of the eight sectors. Each PMT corresponds to one read-out channel. By looking at the channel profile it is possible to diagnose several problems; for example, a *dead* channel will show itself as a “hole” in the illumination pattern, whereas a channel that is noisy and thus has a very high count rate will be coloured in bright red. It can also occur that an entire read-out board needs to be reset or its firmware reloaded. In this case, several neighbouring channels will appear to be missing from the plot. An example, with both noisy and dead channels, is shown in fig. 4.17.

**DecoderErrors** The OM contains read-out error plots for all the subsystems that make use of TEL62 boards (described in section 4.2.2), like the CEDAR/KTAG, and is

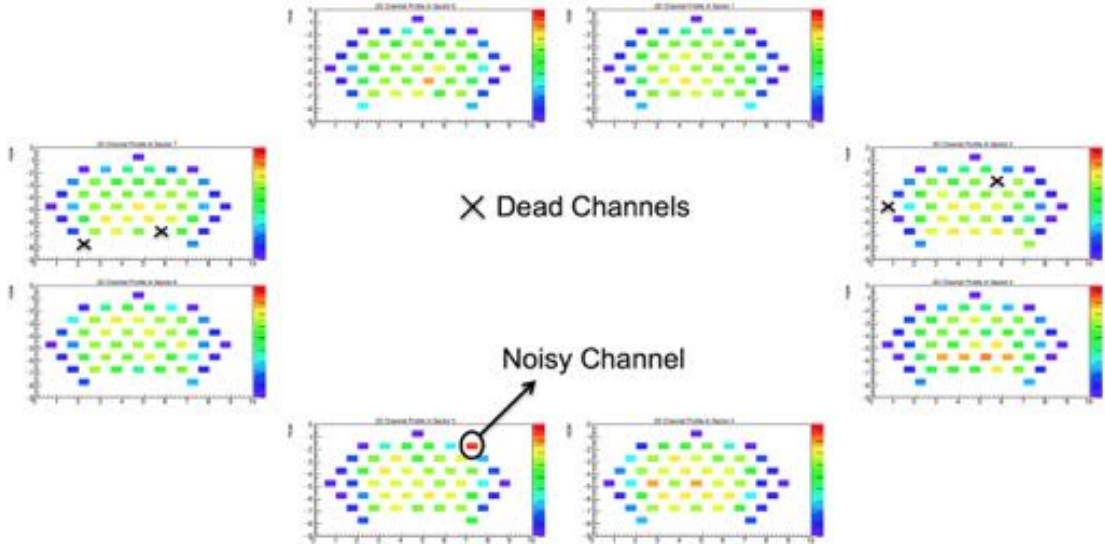


Figure 4.17: Channel profile tab on the CEDAR/KTAG Online Monitor. The plot shows the count rate for each channel or PMT in each one of the eight sectors. From the pattern of illumination one can spot several issues, including dead or noisy channels.

used to diagnose possible issues affecting them. The ideal situation is an empty plot, which corresponds to the absence of any error. In the plot, critical errors are written in red text to distinguish them from non-critical ones. An example in which critical errors are present are shown in fig. 4.18. Very often, in case of sudden and large increase in the rate of particles, a single-event-upset (SEU), that is a bit flip, can occur in the read-out boards, which will then send corrupted data and therefore the plots will be filled with critical errors; in most cases, though, they recover automatically after a few bursts. This is usually observed for many sub-detectors at the same time. These errors are detected by the tool that decodes the raw data, called RawDecoder. For example, in case of a “Bad Trigger Timestamp”, the RawDecoder has found an incompatibility between the timestamps of data and that of the Level-0 Trigger Processor (L0TP). As it is not possible to correct such errors online, a firmware reload is needed. Following some types of critical errors, for example in case of corrupted data with errors in the header of the packet, a whole sector of the KTAG can disappear from the Channel Profile plot and the corresponding events would not be reconstructed.

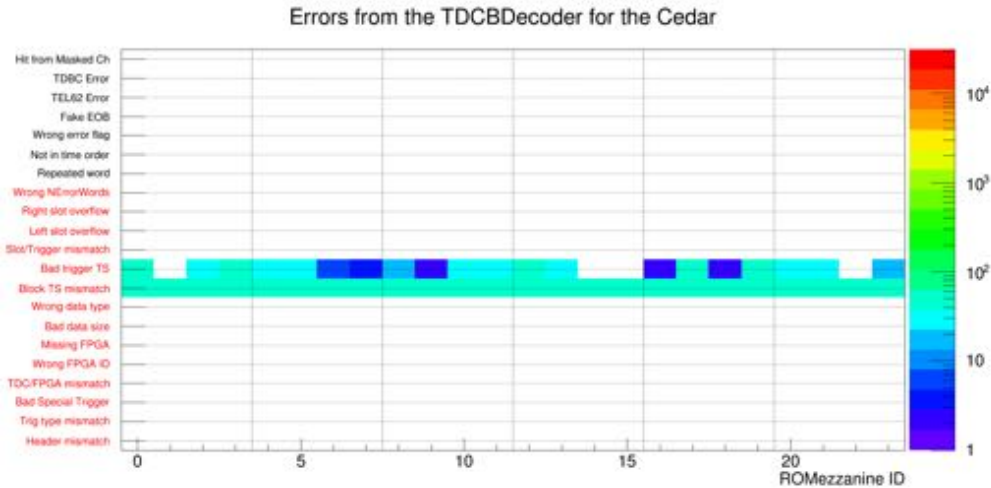


Figure 4.18: Read-out board errors plot on the Online Monitor for TEL62-based (including the CEDAR/KTAG). In case of smooth data-taking, no errors are displayed on the plot. Critical errors, like the ones shown in this picture, require reloading the firmware, and are indicated by red text.

**Fine time Vs Read-out channel number** In order to promptly spot issues as slow time drifts or jumps of a whole read-out board or one or more channels, a plot has been added to the OM to study synchronisation of channels. It displays the fine time of hits vs the read-out channel number. The fine time is calculated as the difference between the hit time and the time of the reconstructed candidate, based on all hits belonging to every read-out board, after the global detector time offset and the TDCB time offsets have been subtracted from the hit time. It therefore represents the residual channel-by-channel time offset. If all time offsets have been corrected for, and no board or channel offset variation occurs, the time difference should be centered at zero for all channels. Such a distribution is shown in fig. 4.19 for a case in which no significant offset is observed, and a case with a time offset for one of the boards, both belonging to the same run. Different TEL62 boards, corresponding to groups of 384 channels, have different offsets, and individual channels can deviate from the global behaviour of the board. As just one in every 8 TDC channels is used by the CEDAR/KTAG sub-detector in order not to overload the buffers, the first TEL62 board will correspond to channel numbers from 0 to 640. A similar reasoning applies to the remaining boards. As will be discussed later, the time offsets are corrected offline on a burst-by-burst basis; only in case the offsets are larger than a few ns is the

L1 algorithm output affected.

**Number of sectors per candidate** The OM allows the monitoring of the distribution of the number of sectors in which a reconstructed candidate has produced hits. In the OM, pion candidates are defined as reconstructed candidates which produce hits in less than four sectors, whereas kaon candidates are defined to have hits in at least four sectors. The number of sectors required for a kaon candidate can, though, be changed by users offline, while performing analyses. An example of this distribution is shown in fig. 4.20; the plot shows a clear separation between kaon (blue) and pion (red) distributions. By fitting the distributions, one finds that the probability of a pion producing 5-fold coincidences in the CEDAR/KTAG is of the order of  $10^{-4}$ .

**Number of reconstructed hits per candidate** The distribution of the number of reconstructed hits per candidate is a useful quantity to monitor to ensure correct data-taking. When the CEDAR/KTAG operates at the standard conditions, for a selected (kaon) candidate, for which hits have been produced in at least 4 sectors, the average number of hits is around 18. In fact, for a kaon travelling through the CEDAR, the average number of photons detected by each sector of the KTAG is 2.25, or 18 photons in total. An example of hits distribution is shown in fig. 4.21.

### 4.3.3 Offline sub-detector performance assessment

Long-term detector performance monitoring is not carried out via online tools at data-taking time, but rather through dedicated tools and within stand-alone studies once a sample of data has been collected. Nonetheless, it can be important to address some of these aspects during a data-taking period, in order to be able to make changes to either the hardware or the software tools. In this section, the performance studies I have carried out during my PhD are described.

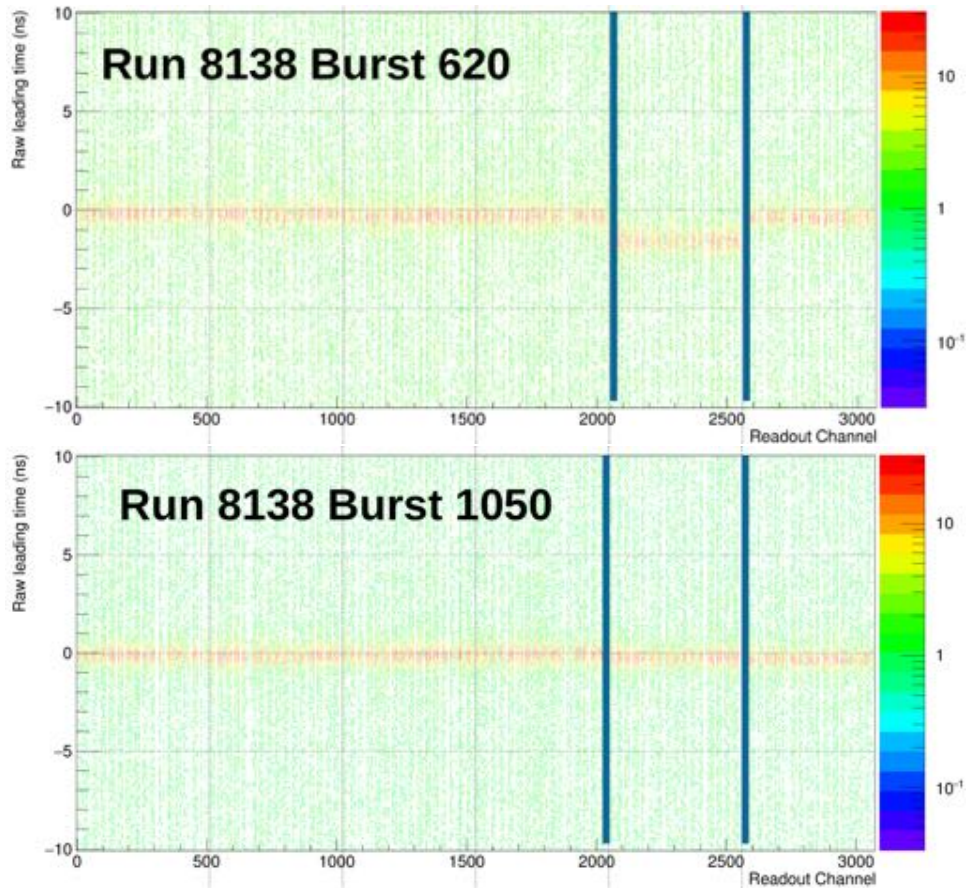


Figure 4.19: Read-out channels fine time vs channel number for all CEDAR/KTAG channels. Just one in every 8 channels is used by the sub-detector; therefore, the first TEL62 board will correspond to channels from 0 to 640. The dashed lines indicate the transition from one TEL62 board to another. From these plots it is possible to diagnose timing issues such as global board or individual channel offsets due to either a slow drift or a jump. The top figure, which is unzoomed, shows a situation with very small board offsets. The bottom plot correspond to a case where large board offsets are present. Small variations can only be noticed by zooming in the plot. The bottom figure shows a zoomed plot corresponding to a situation with both board and channel drifts or jumps.

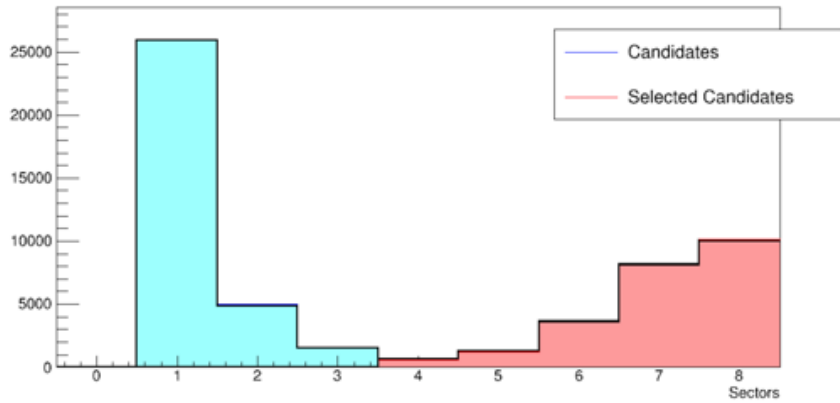


Figure 4.20: Distribution of the number of KTAG sectors where a reconstructed candidate produced hits, for pions (in blue) and kaons (in red). Above 4 sectors the reconstructed candidate is considered to be a kaon in the OM. The black line corresponds to the reference plot, whereas the coloured areas represent the current data distribution.

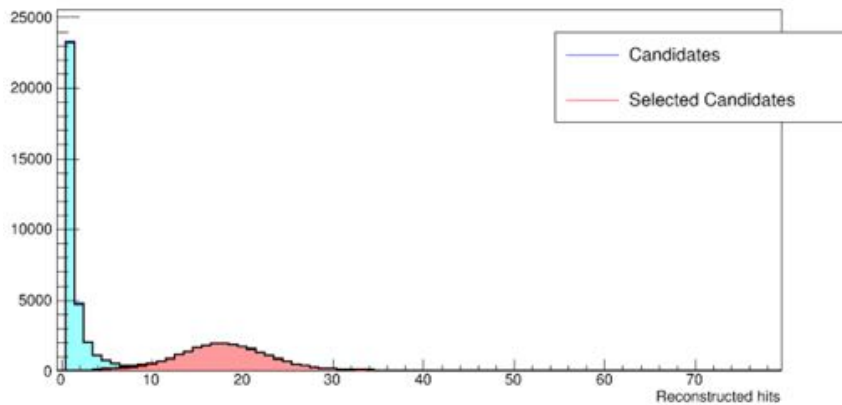


Figure 4.21: Number of reconstructed hits per candidate for non-selected (blue) and selected (red) candidates. At standard operation conditions, the average number of hits per kaon candidate should be  $\approx 18$ . The black line corresponds to the reference plot, whereas the coloured areas represent the current data distribution.

**Read-out electronics performance** Stable performance, radiation-hard read-out electronics are an essential component for smooth data-taking. Occasionally, a board goes into an error state, and it needs a reset or a firmware reload in order to be properly functioning again. The number of firmware reloads needed for each of the boards is recorded by the experiment's Run Control and can therefore be monitored. As the beam intensity was increased from  $\approx 40\%$  of the nominal one in 2016 to  $\approx 60\%$  in 2017, the rate of board failures was observed to increase from 5 to 40 per month; measures have, therefore, been taken in order to reduce the amount of radiation reaching the electronics racks. In fig. 4.23 the number of firmware reloads per day is plotted; the grey bands correspond to periods in which the beam was absent. On 10/04/2017, while I was detector expert, a new  $\gtrsim 1$  m thick concrete wall was installed between the racks and the beamline; this complemented the shielding provided by a previously installed wall, which has been present throughout the whole data-taking. The configuration of walls is illustrated in fig. 4.22, and the newly installed wall is indicated as *first wall* in fig. 4.23. A slight decrease in the number of firmware reloads was observed following this operation, but, as further improvement was desired, the wall was replaced with one that had not previously been exposed to radiation (*second wall* in fig. 4.23). This produced an observable reduction in the number of failures: in the five-day period immediately before the shielding was arranged, 46 failures were observed, whereas only 22 were observed in a five-day period after the shielding was installed. Nonetheless, for the 2018 data-taking, additional shielding was arranged, in the form of a soft case enclosing the rack where the boards are housed.

Another important parameter to monitor is the stability of time offsets. The timestamps provided by the read-out boards for each channel are not absolute time indications; they contain an offset, due to hardware, e.g. the length of cables and the read-out boards, which must be estimated and taken into account in data, and corrected for in case of variations like time drifts and jumps. The corrections are performed at reprocessing time for every burst; I contributed to the implementation of this procedure. As a detector expert in 2017, I studied the variation of timing offsets for the six TEL62s used by the

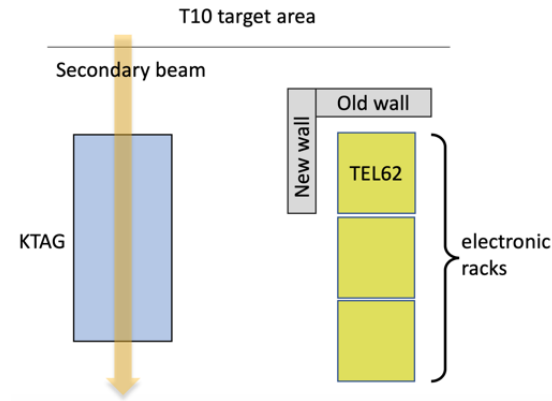


Figure 4.22: Schematic view from above of the KTAG sub-detector and the racks housing its read-out boards and electronic equipment in the TCC8 cavern. A first wall (*old wall* in the diagram) shielding the racks from the T10 target area has been present throughout all the 2016 to 2018 data-taking. A further wall (*new wall* in the diagram) has been installed in 2018 to shield the rack containing the TEL62 boards from radiation reaching the rack from the transverse direction.

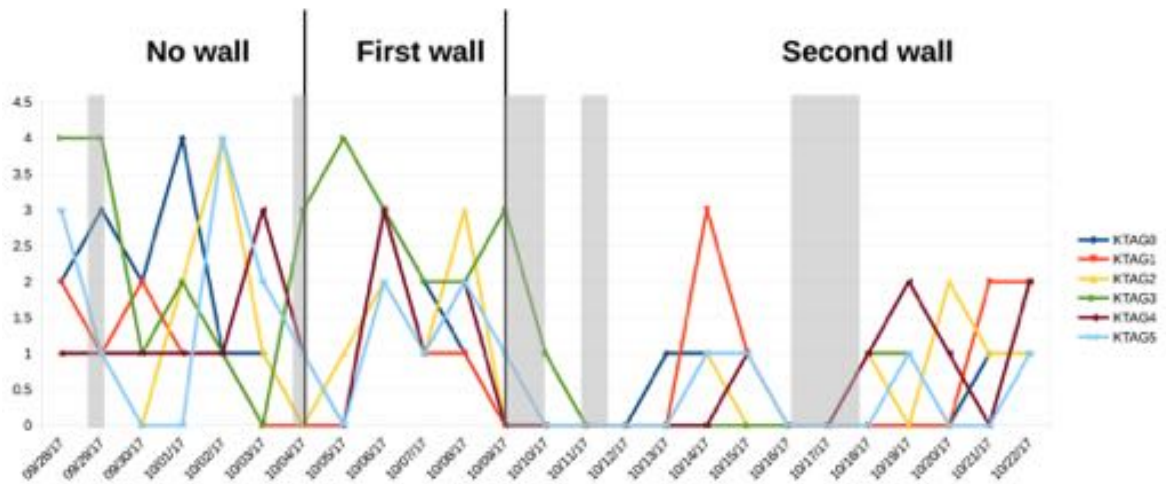


Figure 4.23: Number of necessary reboots of the firmware on each of the six TEL62 boards the KTAG is equipped with for a three-week long data-taking period in 2017. During this time, in order to minimise the rate of failures, concrete walls were installed between the rack where the read-out boards are housed and the KTAG sub-detector. The grey bands correspond to periods when no beam was present.

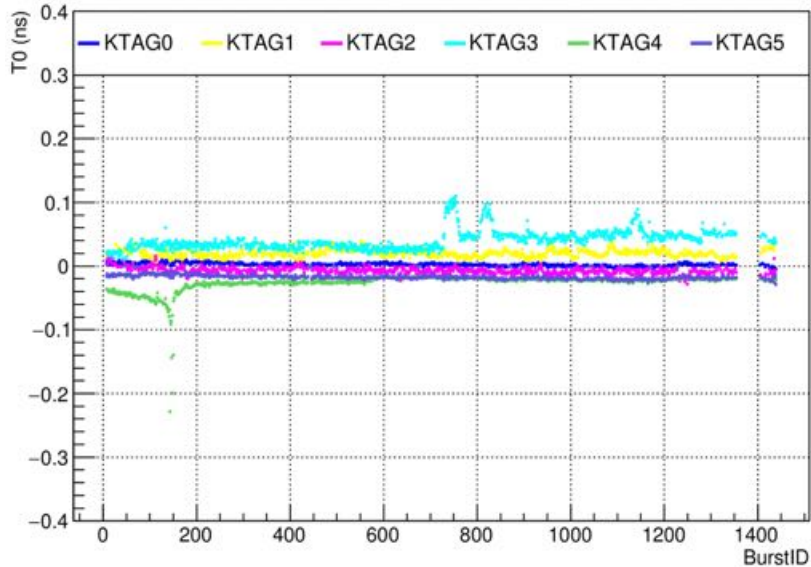


Figure 4.24: Burst-by-burst time offsets for run 8210 for the six TEL62 boards the KTAG is equipped with. The global offset, calculated as the average of all boards, has been subtracted. Different behaviours, such as board time drifts or jumps, can be noticed.

KTAG for a number of runs. An example is shown in fig. 4.24, where some of the boards display in-run variations in their time offset, either abrupt (jumps) or slow (drifts). As explained above, a varying time offset does not affect the quality of data as it is accounted for at reprocessing time; it is nonetheless interesting to monitor the time offsets in order to understand the behaviour of the boards.

**Efficiency and quality of data** On top of monitoring the sub-detector’s behaviour online during data-taking periods, it is important to assess its performance once the data has been collected and stored, in order to identify possible issues to be addressed concerning either the detector or the data processing, and to notify the data users that are performing physics analyses about runs or bursts in which the detector has under-performed. In the NA62 software framework this task is carried out, on a burst-by-burst and run-by-run basis, by a specific algorithm [61].

In order to study the quality of data, the sub-detector’s efficiency is defined, for each SPS burst, as:

$$\epsilon_N = \frac{n_{N, \text{in time}}}{n_{tot}} \quad (4.17)$$

that is the ratio of the number of events for which a reconstructed candidate with hits in at least  $N$  sectors that are compatible with a reference time ( $n_{N, \text{in time}}$ ) is found, to the total number of events in the data sample.

The algorithm uses as input a sub-sample of events that have passed the standard selection for the  $K^+ \rightarrow \pi^+\pi^0$  ( $k2\pi$ ) decay, and thus the reference time is the decay time estimated separately by the algorithm that performs the  $k2\pi$  selection. The time interval between the candidate and reference time must be smaller than 3 ns for the candidate to be “in time”. As an alternative way to estimate efficiency, a sample of  $K^+ \rightarrow \pi^+\pi^+\pi^-$  ( $k3\pi$ ) decays can be used.

The sub-detector is considered to be efficient if this estimate is, when one considers candidates with hits in at least 4 sectors, above a threshold normally chosen as 95%.

For each run, the tool provides burst-by-burst efficiency plots for varying number of sectors, a list of “bad” bursts in which the quality of the KTAG data is low either due to a failure in the detector or because of other reasons, and root files containing more detailed information.

The efficiency plot provided as output by the algorithm for a 2016 run is shown in fig. 4.25. “Holes” within the run may correspond, for example, to a period when the proton beam is absent, or to a time during which one or more read-out boards need to be reset or their firmware reloaded. From the information provided by the CEDAREfficiency analyser for each single run, it is then possible to build efficiency trends for a whole data-taking period.

Data taking efficiencies for 2016, 2017 and 2018 data samples are shown in fig. 4.26, fig. 4.27 and fig. 4.28.

A drop in efficiency that can be observed in 2016 for run 6561 and the following ones is due to one the TEL62 boards being switched off after a period of repeated failures that could only be dealt with through a long and complex procedure impacting data-taking

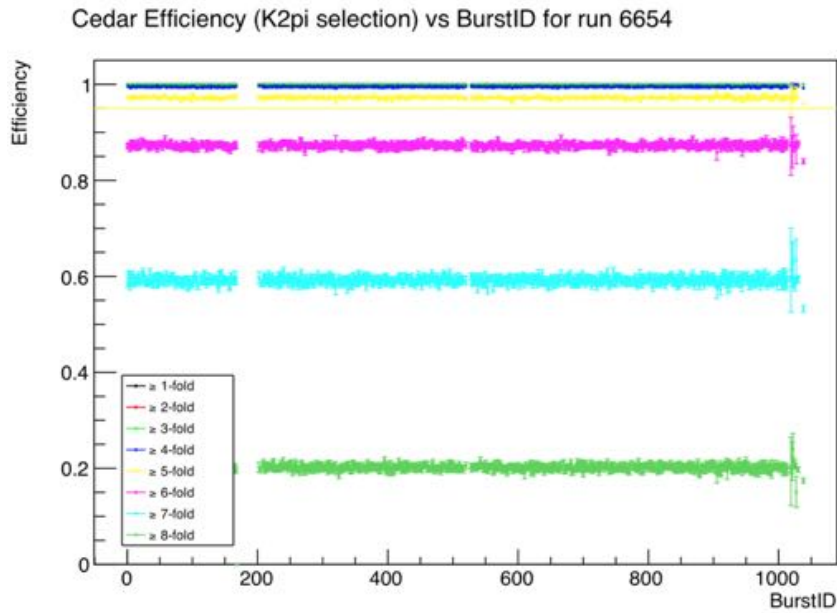


Figure 4.25: Efficiency as a function of burst number for the KTAG sub-detector in 2016 run 6654. The sub-detector is performant if the efficiency for 4-fold coincidences is above a value indicated by the horizontal line.

time. The efficiency when requiring candidates with hits in at least 4 sectors is only mildly affected and still above 99%, and the efficiency for 5 sectors is well above 95%.

As mentioned above, the efficiency algorithm also outputs a list of bursts in which the behaviour of the KTAG sub-detector has not been optimal. Possible failures include:

- the burst contains no triggers, the file is corrupted;
- the number of particles in the beam is too low to provide a reliable estimate of the efficiency;
- the statistics in the  $k2\pi$  or  $k3\pi$  samples is low and insufficient for the computation of efficiency.

The user can decide whether to use or skip these problematic bursts when running their analyses.

The efficiency algorithm relies on the reconstruction of particular data samples, and therefore on the quality of the beam and the performance, both hardware and software, of other sub-systems; in the case of a  $k2\pi$  sample, in particular, it relies on the LKr

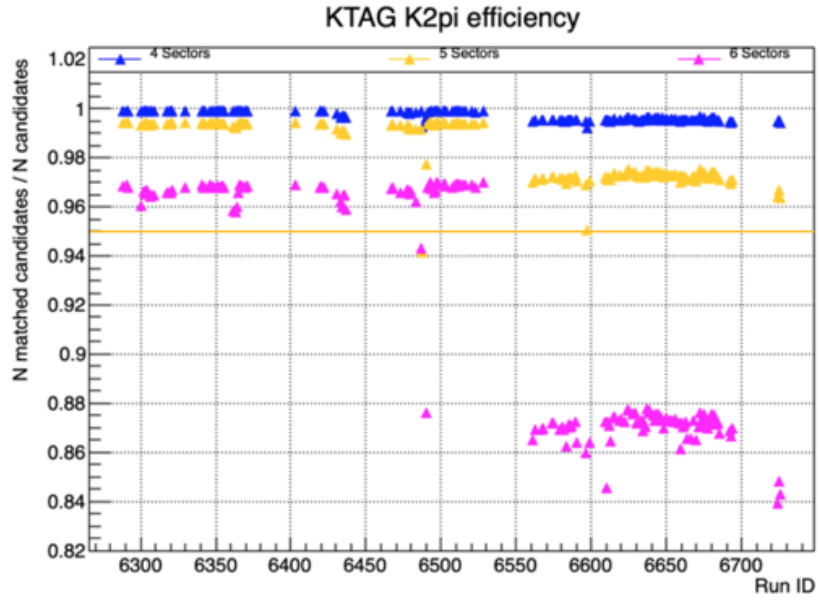


Figure 4.26: CEDAR/KTAG efficiency for the main data sample from 2016. The efficiency is systematically lower from run 6561 after a TEL62 read-out board was switched off following repeated failures.

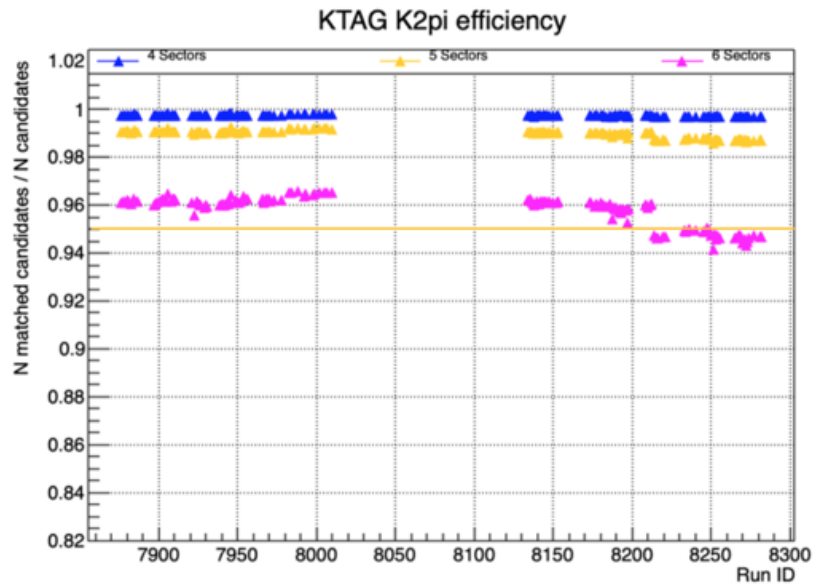


Figure 4.27: CEDAR/KTAG efficiency for the main data samples from 2017.

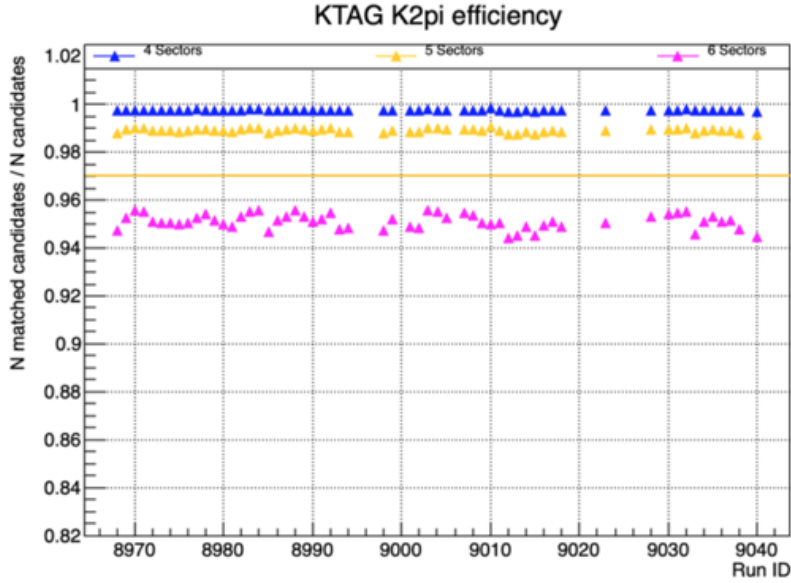


Figure 4.28: CEDAR/KTAG efficiency for a sub-sample of 2018 data.

calorimeter, used to reconstruct the  $\pi^0$  mass from the photons' energy deposits. As software issues can be fixed and the quality of data improved when better refined data processing and reconstruction tools are available, the estimate of the efficiency of the sub-detector can improve as new software versions are released, and the number of bursts labelled as bad can thus decrease.

## 4.4 Conclusions

The NA62 unseparated secondary hadron beam contains a large fraction of pions and protons. This leads to the necessity of tagging the beam kaons; for this purpose, a CERN CEDAR was employed. In order to sustain the NA62 high particle rate and to meet the desired efficiency and time resolution, the light detection and read-out systems of the CEDAR were replaced with a new purpose-designed system, the KTAG, using 384 PMTs instead of 8. In the present chapter the CEDAR/KTAG sub-detector has been described and its performance has been discussed, together with the procedures to carry out to ensure good data-taking and the follow-up studies to confirm its correct functioning and assess the quality of the collected data.

## CHAPTER 5

# MEASUREMENT OF THE BR OF $K^+ \rightarrow \pi^+ \gamma \gamma$

The present chapter describes a measurement of the  $K^+ \rightarrow \pi^+ \gamma \gamma$  BR performed on data samples from the NA62 experiment's 2016 and 2017 data-taking periods. The experimental signature of the decay and the measurement strategy are discussed first. In order to meet storage constraints, NA62 data samples must undergo an additional offline level of reduction or *filtering* following the full reconstruction; the filtering stage and the full selection for signal and normalisation samples are described. The background channels affecting the measurement are then presented, as well as a biased MC generator introduced in the NA62 software framework to study the main mechanism through which they pass the signal selection. Finally, two estimates of the BR, one of which is model-independent, are presented, and the studies of systematics performed are discussed.

### 5.1 Measurement strategy

The experimental signature of the decay consists of a charged track in the downstream spectrometer (STRAW), corresponding to the  $\pi^+$ , and two photon clusters in the electromagnetic calorimeter (LKr) away from the projection of the charged track, with no extra tracks or clusters in time and no in-time activity in the veto sub-detectors. The measurement of the  $K^+ \rightarrow \pi^+ \gamma \gamma$  decay can be normalised to that of the  $K^+ \rightarrow \pi^+ \pi^0$  channel, which has exactly the same signature, except for the di-photon invariant mass:

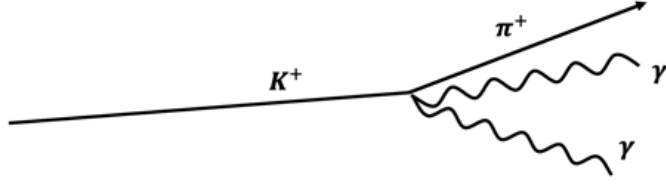


Figure 5.1: Signature of the  $K^+ \rightarrow \pi^+\pi^0$ , consisting in a charged track for the  $\pi^+$  and two electromagnetic clusters in the LKr calorimeter.

$m_{\gamma\gamma} = M_{\pi^0}$ . This allows for first-order cancellation of systematic uncertainties. The full expression of the BR is given in section 5.4.

### 5.1.1 Decays of the charged kaon

The kaon decays with BRs of the same order of magnitude as  $K^+ \rightarrow \pi^+\gamma\gamma$  ( $\approx 10^{-6}$ ) or larger can be grouped in several categories, each of which is eliminated or reduced by one or more cuts in the selection for  $K^+ \rightarrow \pi^+\gamma\gamma$  and  $K^+ \rightarrow \pi^+\pi^0$ . In particular:

- multi-track decays, such as  $K^+ \rightarrow \pi^+\pi^+\pi^-$ ,  $K^+ \rightarrow \pi^+\pi^-e^+\nu_e$  and  $K^+ \rightarrow \pi^+\pi^-\mu^+\nu_\mu$ , can be reduced by only selecting single-track decays, that is by requiring the absence of any group of tracks compatible in time;
- multi-photon decays with more than two photons in the final state, such as  $K^+ \rightarrow \pi^+\pi^0\pi^0$ ,  $K^+ \rightarrow \pi^0\pi^0e^+\nu_e$  and  $K^+ \rightarrow \pi^+\pi^0\pi^0\gamma$ , can be reduced or eliminated via cuts on the number of well-separated EM clusters, via the use of large and small angle veto, and via cuts on the final state reconstructed total and transverse momentum;
- events with missing momentum, such as  $K^+ \rightarrow \mu^+\nu_\mu$  and  $K^+ \rightarrow e^+\nu_e$ , can be reduced by cutting on the final state reconstructed total and transverse momentum.

The full selection for the signal and normalisation channels is described in section 5.2. At the end of the selection, only two backgrounds are found, namely  $K^+ \rightarrow \pi^+\pi^0\pi^0$ , and

$K^+ \rightarrow \pi^+\pi^0$  with an extra radiated inner bremsstrahlung (IB) photon. The mechanisms through which they enter the signal acceptance are discussed in section 5.3.

### 5.1.2 Data samples and trigger lines

The analysis could not benefit from a dedicated trigger line, and therefore was performed on minimum bias samples. The following two samples collected by the NA62 experiment between 2016 and 2017 were used:

- Control trigger sample: collected requiring primitives from the NA48CHOD sub-detector, with variable downscaling;
- Non-muon trigger: collected requiring a primitive in the RICH and the CHOD, and no primitives in the MUV3. At L1, KTAG hits in at least 4 sectors in a 10 ns time window around the trigger time are required.

The NA48 CHOD, CHOD and RICH sub-detectors' primitives determine the presence of a charged track in the event, above threshold in case of the RICH. The absence of MUV3 primitives excludes the presence of muons travelling throughout the decay region. For more information about trigger primitives, one can refer to chapter 4.

### 5.1.3 Filter

The large volume of data and the limitations in the available bandwidth make it so that the full reconstructed data cannot be saved to storage. Furthermore, limitations in distributed computing resources at user level make running an analysis on large data samples a time-consuming process. In consequence, a data reduction or filtering stage has been introduced in the data processing framework.

A specific *filter* has been implemented in the NA62 software framework for the  $K^+ \rightarrow \pi^+\pi^0$  and  $K^+ \rightarrow \pi^+\gamma\gamma$  decays. The filter requires control trigger or non-muon trigger and

it asks, via loose selection criteria, that in each stored event there is at least one decay candidate that matches the common characteristics of the above decays. In particular, at least one combination of one track, satisfying minimal quality requirements, and two EM clusters not associated to the track are required, with total reconstructed momentum between 60 and 80 GeV. The clusters are furthermore required to be closer in time to the track than 10 ns, and less than 10 ns away from each other. Finally, for the above combination of one track and two clusters, there should be no match in the LAV sub-detector within a 5 ns time window around the mean clusters time. The filter reduces reconstructed data to 2% of the original number of reconstructed events.

## 5.2 Data selection

The analysis is performed in two stages: in the first, groups of exactly one track and two clusters that form a candidate decay  $K^+ \rightarrow \pi^+ \gamma \gamma$  are found in the 25 ns-long event timeslot. The groups are formed by asking that the clusters are closer in time to the track than 10 ns, and that no additional track is found within a 3 ns time window from the first one. These conditions are designed to reject extra activity, such as additional kaon decays, accidental beam pions or muons from the beam halo, in time with the decay candidate.

The probability of having an additional kaon decay in fiducial volume (FV) in a triggered event is:

$$P_{2K} = R \times F_K \times P_{FV} \times \Delta t \approx 7\% \quad (5.1)$$

where  $R$  is the secondary beam rate,  $F_K$  is the fraction of kaons in the beam,  $P_{FV}$  is the probability for a kaon to decay in the NA62 FV, and  $\Delta t$  is the 25 ns long time slot corresponding to a triggered event.

Track times are obtained from the closest match in the CHOD sub-detector; in case of failed association, the NewCHOD or RICH sub-detectors are used instead.

In fig. 5.2, the difference between the track's time and the mean cluster time is shown

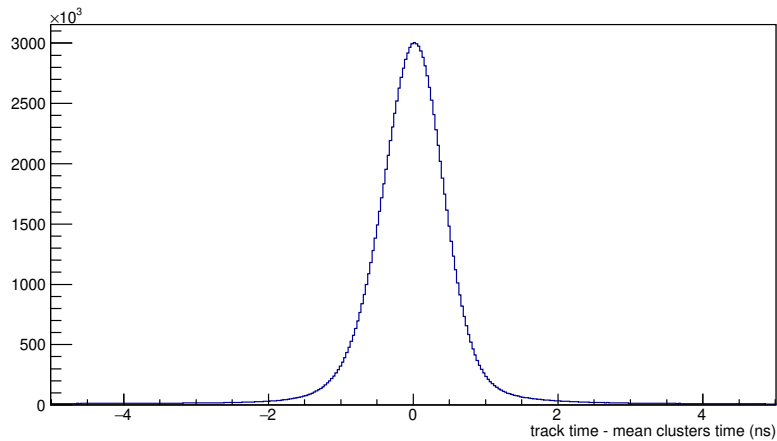


Figure 5.2: Difference between the time of a selected track and the mean time of the associated two clusters for 2016 data. The RMS is  $\approx 490$  ps, consistent with the resolution of the detectors used: 200 ps for the CHOD), and  $2.5/\sqrt{E[GeV]}$  ns, in the range 300 ps - 1 ns, for the LKr.

for 2016 data.

As pions can produce multiple EM clusters at several cm of distance from their impact point on the LKr, an exclusion region is defined: the two clusters in the candidate decay must be at least 25 cm away from the track's projection on the LKr upstream surface.

The second stage of the selection includes cuts on track quality, cluster quality, kinematic variables, and particle identification and veto conditions. They are described below.

**Track quality** The track is required to have positive charge, to be in the geometric acceptance of and to have produced hits in all the spectrometer chambers, to be in the geometric acceptance of the NA62 CHOD and the LKr; it is furthermore required to have momentum between 5 GeV and 70 GeV, a  $\chi^2 < 20$ , and a closest distance of approach (CDA) with the average beam direction smaller than 25 mm.

**Particle identification** The  $E/p$  of the track, where  $p$  is the track's momentum as measured in the spectrometer and  $E$  is the energy of the closest match in the LKr calorimeter, must be consistent with the pion's hypothesis, and is therefore required to

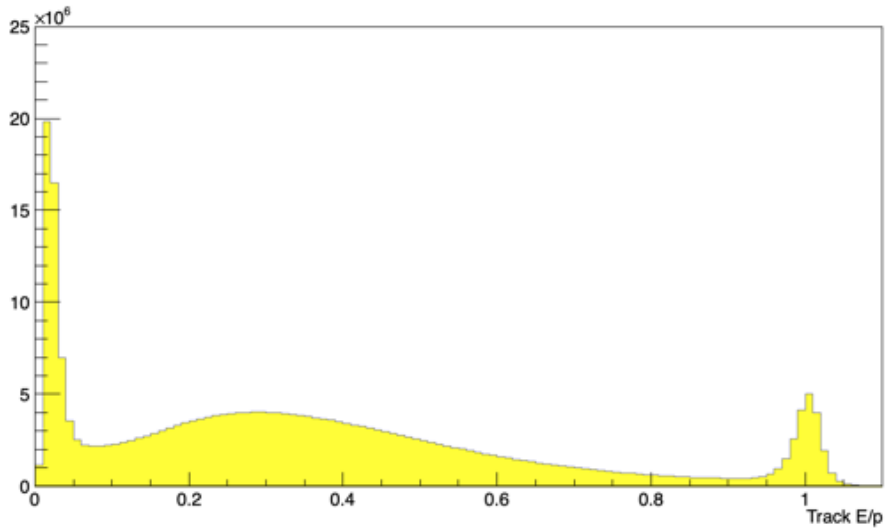


Figure 5.3: Track E/p for a data sample from 2017 data-taking.

be between 0.05 (to exclude muons) and 0.85 (to exclude electrons). The distribution for this variable is shown in fig. 5.3. Additionally, no association must be found in the MUV3 sub-detector.

**Cluster quality** The energy of each cluster in the LKr is required to be larger than 4 GeV. The clusters must be at least 2 cm away from the nearest calorimeter dead cell. The two photon candidates must be maximum 2 ns away from each other, and they must have a space separation of at least 25 cm.

**Photon veto** In order to efficiently reject multi-photon backgrounds, it is asked that no matches are found in the LAV and SAV sub-systems in a 5 ns time window around the decay candidate time, which is given by the average time of the track and the two clusters.

**Kinematic variables** The total momentum of the one track and two cluster system is required to be consistent with that of the kaon parent particle; its magnitude is therefore requested to be between 72.5 GeV and 77.5 GeV. The total transverse momentum of the

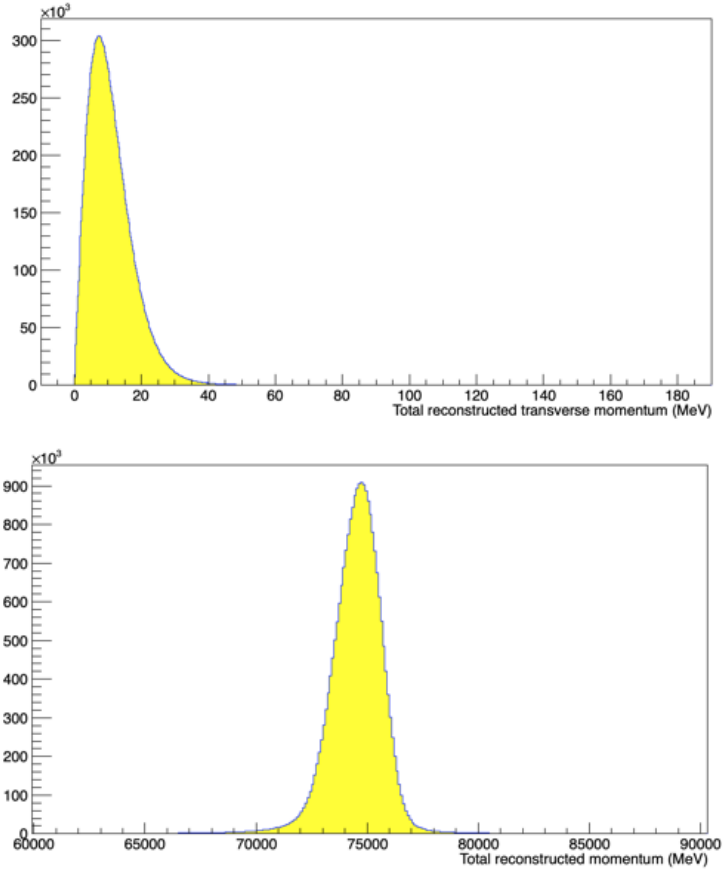


Figure 5.4: Total reconstructed transverse momentum (top) and total reconstructed momentum magnitude (bottom) for a 2017 data sample.

system must be below 50 MeV. Both distributions for a data sample from 2017 can be found in fig. 5.4, from which one can notice that the total momentum distribution is peaked at a smaller number than 75 GeV, due to energy mis-calibrations to be corrected in future studies. The offset is small compared to the size of the cut, and is therefore not matter of concern. The total invariant mass of the system must be compatible with the kaon mass within a  $4\sigma$  interval. The resolution on the total mass, which can be observed for data and MC on the bottom in fig. 5.5, is 6 MeV. The final cut, which distinguishes the signal and normalisation channels and identifies the signal region, is applied to the kinematic  $z$  variable, introduced in chapter 1 and defined as the squared invariant mass of the two photons normalised to the squared kaon mass:  $z = m_{\gamma\gamma}^2/M_K^2$ . The signal region has been chosen as  $z > 0.225$ , while the  $z < 0.225$  region is dominated by  $K^+ \rightarrow \pi^+\pi^0$  decays. The  $K^+ \rightarrow \pi^+\pi^0$  peak in this distribution is shown on the top in fig. 5.5; its

resolution is 0.003.

For both the total invariant mass and the  $z$  distributions, a displacement between data and MC of 1.7 MeV for the reconstructed total invariant mass (kaon mass), and of 0.001 for the reconstructed kinematic  $z$  variable, is observed.

### 5.3 Study of backgrounds

The only two decay channels surviving the selection for  $K^+ \rightarrow \pi^+ \gamma \gamma$  are  $K^+ \rightarrow \pi^+ \pi^0 \gamma$  with an extra radiated IB photon, and  $K^+ \pi^+ \pi^0 \pi^0$ . This is evident from fig. 5.9, where no other contribution except from such channels is found well below the signal region, defined as  $z > 0.225$ . The effect of the main analysis steps and the reduction that each of them performs on potential backgrounds is summarised in table 5.1.

Both channels have more than two photons in the final state and therefore should not be present in the selected sample, however, they pass the selection via the mechanisms listed below:

- A photon reaches the LKr at a distance smaller than 25 cm from the track's projection, within the veto window for clusters produced by the  $\pi^+$ . The cluster is vetoed as it is indistinguishable from a pion cluster, and therefore goes uncounted;
- A photon is outside of the geometric acceptance of the LKr, and it is not detected by the veto sub-detectors;
- A photon is too *soft* - i.e. it has too low energy - to produce a cluster in the LKr;
- Two photons hit the LKr at a short relative distance and produce overlapped showers that result in a single reconstructed cluster (*merged*).

For  $K^+ \rightarrow \pi^+ \pi^0 \gamma$  (IB), which has three final-state photons, one of the above mechanisms is sufficient for the event to be accepted. The relative frequency of occurrence of the above categories is summarised in table 5.2.

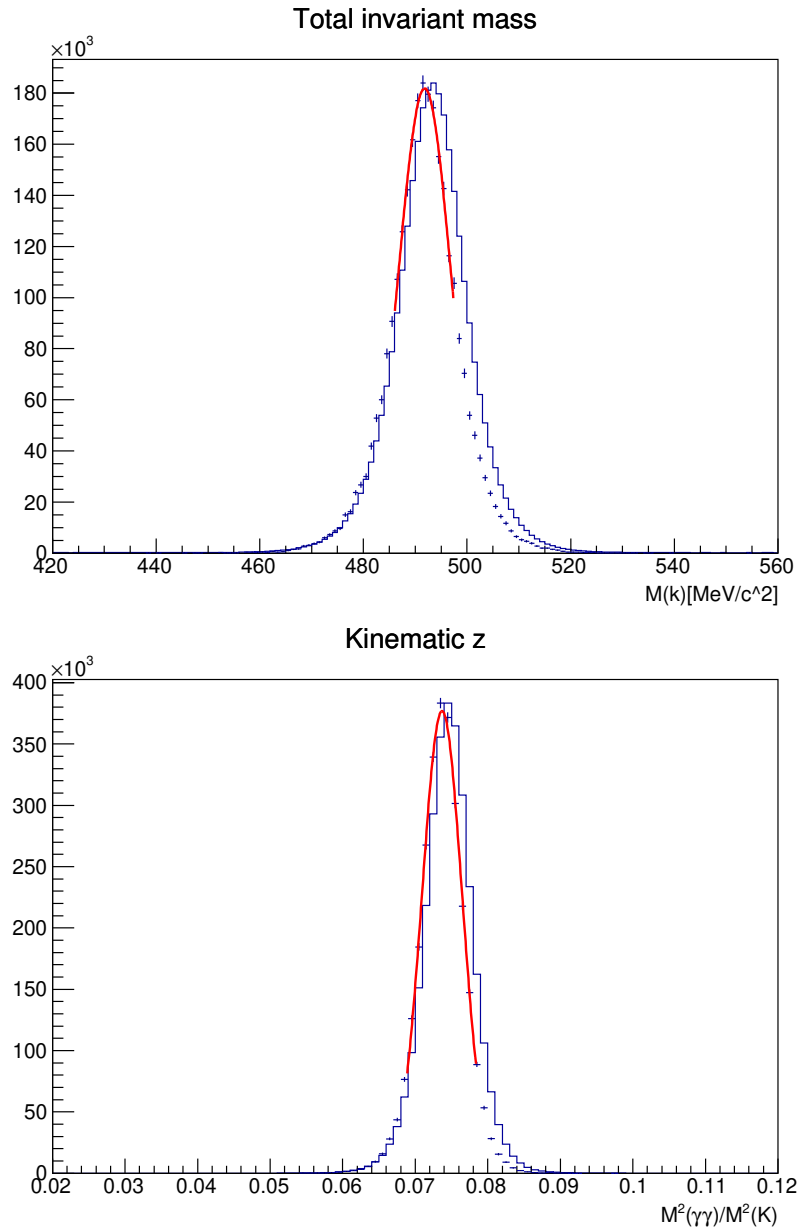


Figure 5.5: Total invariant mass  $M_K$  distribution (top) and kinematic  $z$  distribution (bottom) for data (solid line) and  $K^+ \rightarrow \pi^+ \pi^0$  MC over the 2016 period A data sample.

	$\pi^0 \mu^+ \nu_\mu \gamma$	$\pi^+ \pi^+ \pi^-$	$\pi^0 e^+ \nu_e$	$\pi^+ \pi^- \mu^+ \nu_\mu$	$\mu^+ \nu_\mu \gamma$	$\pi^0 \pi^0 e^+ \nu_e$	$e^+ \nu_e \gamma$	$\pi^+ \pi^- e^+ \nu_e$
Events in FV (tot)	$1.1 \times 10^7$	$1.2 \times 10^7$	$0.9 \times 10^7$	$8.5 \times 10^7$	$1.6 \times 10^7$	$4.4 \times 10^7$	$4.4 \times 10^7$	$8.0 \times 10^7$
1 track 2 clusters ev. (%)	8.7	4.3	21.5	7.2	1.3	17.0	1.3	5.7
Track quality (%)	6.1	1.5	16.3	2.5	0.8	12.4	0.9	2.0
Track E/p and LKr ass. (%)	3.7	0.9	0.2	1.4	0.4	0.2	0.2	0.9
Track momentum (%)	3.6	0.9	0.2	1.4	0.4	0.2	0.2	0.9
Track muon veto ass. (%)	0.06	0.60	0.21	0.70	0.14	0.21	0.14	0.87
No veto matches (%)	0.03	0.37	0.16	0.60	0.08	0.001	0.07	0.33
Clusters quality (%)	0.023	0.106	0.075	0.014	0.053	0.001	0.048	0.126
Total momentum (%)	0.019	0.024	0.006	0.0002	0.050	0.0003	0.044	$4 \times 10^{-5}$
Transverse momentum (%)	0.018	0.023	0.004	0.0002	0.05	0.0002	0.04	$2.5 \times 10^{-5}$
Total mass (%)	0.017	0.022	0.001	0.0002	0.05	0.0002	0.04	0
Kinematic z (%)	0	0	0	0	0	0	0	0

Table 5.1: For each background final state, the first row contains the number of events in FV for the used MC samples, while the following rows show the effect of the main selection steps of the analysis, described in the previous sections.

<i>Category</i>	<i>Relative frequency</i>
1) A vetoed cluster	19%
2) An undetected photon	15%
3) A soft photon	28%
4) A merging of two photons into one cluster	36%

Table 5.2: Mechanisms through which background decays enter the acceptance region for the signal. The dominant effect is due to photons producing overlapping EM showers in the LKr, and therefore resulting in a single merged cluster.

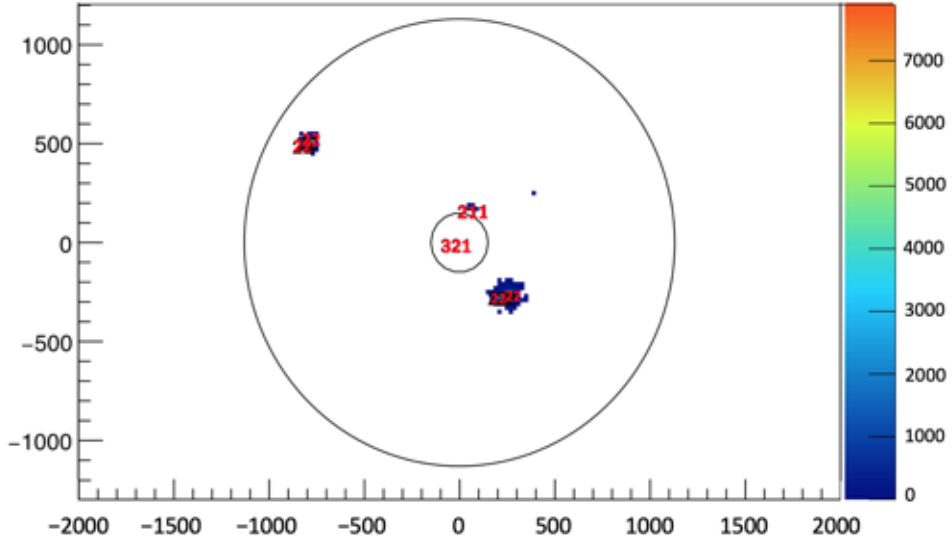


Figure 5.6: Example of the EM clusters produced in a  $K^+ \rightarrow \pi^+ \pi^0 \pi^0$  MC event passing the signal selection. Two pairs of photons, on the left and on the right of the beampipe hole, overlap and produce a single cluster each. The PDG particle codes have the following interpretation: 22 indicates a photon, 321 indicates a charged kaon, 211 indicates a charged pion.

For  $K^+ \rightarrow \pi^+ \pi^0 \pi^0$ , which has four final-state photons, a combination of two of the above mechanisms is necessary for an event to be accepted. The acceptance for this background is therefore at a level of  $A_{\pi^+ \pi^0 \pi^0} \approx 10^{-7}$  over the whole signal range, as opposed to the higher acceptance for  $K^+ \rightarrow \pi^+ \pi^0 \gamma$  (IB):  $A_{\pi^+ \pi^0 \gamma} \approx 10^{-5}$ .

The accepted events in the signal region of  $K^+ \rightarrow \pi^+ \pi^0 \pi^0$  over a sample of six million events produced centrally at NA62 were only eight; of these, five were due to double cluster merging, two were due to a merging combined with a vetoed cluster, and one was due to a merging combined with an undetected photon. An example of a MC event with double cluster merging can be found in fig. 5.6.

### 5.3.1 Implementation of biased MC generators

In order to estimate the background contamination in the events passing the  $K^+ \rightarrow \pi^+\gamma\gamma$  selection, MC samples of appropriate size need to be used for the contributing decay modes.

The minimum size of the necessary MC samples is dictated by requirements on the precision to which one wishes to know each component, and its contribution to the total error (excluding systematics). For the present study, the former requirement has been set to maximum 50%, and the latter to maximum few %. The total relative statistical error on signal events  $S = N - B$ , where the number of background event is indicated as  $B$  and the total events in the signal region as  $N$ , is given by:

$$\frac{\Delta S}{S} = \sqrt{\frac{\Delta N^2}{S^2} + \frac{\Delta B^2}{S^2}} \quad (5.2)$$

The number of expected signal and background events above  $z = 0.225$  is shown in table 5.3. As  $N \approx S$ , that is  $S \gg B$ , then:

$$\frac{\Delta S}{S} \sim \sqrt{\left(\frac{\Delta N}{N}\right)^2 + \left(\frac{\Delta B}{N}\right)^2} \quad (5.3)$$

In eq. (5.3),  $\Delta N = \sqrt{N}$ , and  $B$  and  $\Delta B$  are estimated from the total number of kaon decays, each channel's BR and its acceptance from MC.

The contribution of each background channel  $B_i$  to the total statistical error is then given by:

$$\frac{\Delta(S + B_i) - \Delta S}{\Delta S} = \frac{\sqrt{\Delta N^2 + \Delta B_i^2} - \sqrt{\Delta N^2}}{\sqrt{\Delta N^2}} \quad (5.4)$$

As previously discussed, only the two channels  $K^+ \rightarrow \pi^+\pi^0\gamma$  (IB) and  $K^+ \rightarrow \pi^+\pi^0\pi^0$  survive all selection cuts and enter the signal acceptance region. The largest contribution to the background from these two channels is due to two of the final-state photons producing overlapping showers that result in merged clusters in the LKr calorimeter. The probability that the LKr calorimeter reconstruction merges two photons depends on a

number of variables; these include, in particular, the separation of the photons' impact points on the calorimeter and the ratio of their energies.

$K^+ \rightarrow \pi^+\pi^0\gamma$  (IB) and  $K^+ \rightarrow \pi^+\pi^0\pi^0$  are known with a relative uncertainty of, respectively, 6% and 30%, as proven by the estimates shown in table 5.3. The contribution to the total uncertainty (excluding systematics) is given by:

$$\frac{\sigma_{tot} - \sigma_{MC}}{\sigma_{tot}} \quad (5.5)$$

where  $\sigma_{tot}$  is the uncertainty including both the two background contributions, and  $\sigma_{MC}$  is the uncertainty estimated using only the background under consideration. For the background from  $K^+ \rightarrow \pi^+\pi^0\gamma$  (IB) the contribution to the total uncertainty is of the order of 2%; this was deemed acceptable. For  $K^+ \rightarrow \pi^+\pi^0\pi^0$ , the contribution to the total statistical error is at the level of 5%, indicating the MC sample has insufficient size for a good background estimate.

The production of large MC samples is a computationally expensive and time-consuming process; It is therefore advisable to alter (or *bias*) the existing MC generators in a way that the probability that a background event passes the selection for the decay under study is increased. In this way, the production of smaller samples is sufficient for reaching the desired precision.

For the present study, a biasing option was introduced in the MC FORTRAN routines which are called after a  $K^+$  is generated and are responsible for simulating its decay according to the differential decay spectrum of the specific channel. The biasing is implemented by iteratively calling the routine until it generates an event that satisfies the requirement.

When estimating the background events in a data sample using a biased MC, in order to obtain the correct estimate of the background acceptance, one must multiply the number of background events surviving the acceptance by an additional scale factor that provides the probability that a biased event is produced. The latter factor can be

obtained by estimating, over a sufficiently large sample, the average number of trials, that is the number of times the generator was called before successfully producing an event that satisfies the requirements.

In order to enrich the  $K^+ \rightarrow \pi^+\pi^0\gamma$  (IB) and  $K^+ \rightarrow \pi^+\pi^0\pi^0$  MC samples in events with cluster merging, one possibility is to require that each generated event in the sample contains at least two photons forming an angle small enough that the probability of the photons producing a merged LKr cluster is maximised:  $\theta_{\gamma\gamma}^{min} < \theta_{\gamma\gamma}^{bias}$ . Here  $\theta_{\gamma\gamma}^{min}$  indicates the minimum angle between all the angles formed by each pair of photons in the event, and  $\theta_{\gamma\gamma}^{bias}$  is referred to as the biasing angle. The routine proceeds according to the following steps:

- An event is generated according to the decay spectrum of the channel of interest;
- A nested loop identifies all the pairs of photons in the event, and for each pair it computes the angle formed by their momenta;
- If at least one of the angles in this list is smaller than  $\theta_{\gamma\gamma}^{bias}$ , the event is stored; else, the event is discarded and the routine is called again. The number of times the routine is called before a new event is stored, that is the number of trials, is also saved.

The option was included in the NA62 software framework and it allows every user to set a custom biasing angle for the MC generation of  $K^+ \rightarrow \pi^+\pi^0\gamma$  (IB, direct emission (DE) or interference between the two former processes) and  $K^+ \rightarrow \pi^+\pi^0\pi^0$ .

In order to assess the effectiveness of the biasing option in producing events with clusters that are close to each other in the LKr, the distribution of the minimum distance between two clusters was plotted for several values of the biasing angle in fig. 5.7.

In order to choose the biasing angle  $\theta_{\gamma\gamma}^{max}$ , two considerations must be made: in the first place, the biasing angle must alter as little as possible the spectrum of minimum angles in the events that pass the selection with the unbiased generator, and must therefore be large enough for most of the angles of selected events to lie below its value.

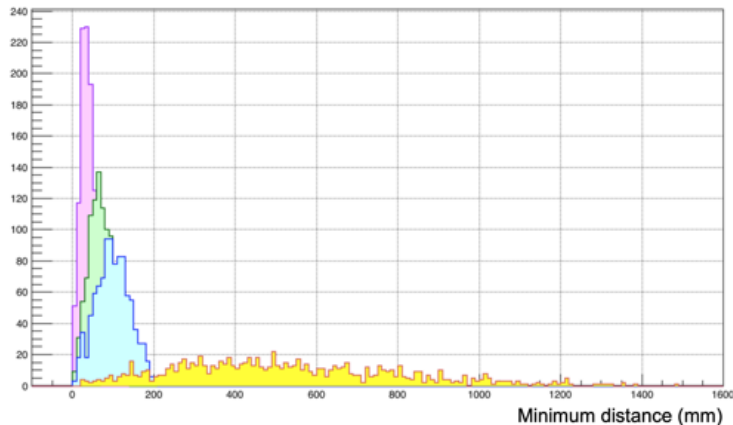


Figure 5.7: Distribution of minimum distance between two clusters on the LKr calorimeter, when using a biased MC with maximum angles  $\theta_{\gamma\gamma}^{max}=0.0005$  rad (pink), 0.001 rad (green), 0.0015 rad (blue) and no bias (yellow). The distributions are not normalised.

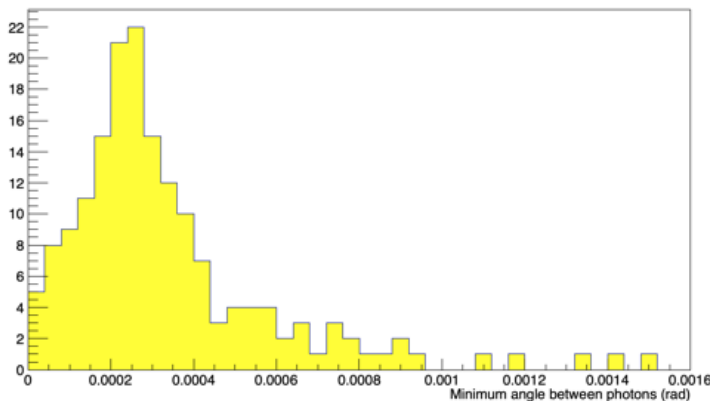


Figure 5.8: Distribution of minimum angles between two photons in  $K^+ \rightarrow \pi^+\pi^0\gamma$  (IB) events passing the full signal selection below  $\theta_{\gamma\gamma}^{bias} = 1.6$  mrad.

The distribution of the minimum angle between two photons in each event, for decays produced with the standard  $K^+ \rightarrow \pi^+\pi^0\gamma$  (IB) generator and passing the full signal selection, can be seen in fig. 5.8.

The second criterion is that the maximum angle must be as small as possible in order to minimise the number of trials necessary before an event that satisfies the requirement is produced. These two considerations led to the choice of a maximum angle  $\theta_{\gamma\gamma}^{max} = 1.6$  mrad. The sample produced with this choice of maximum angle, as shown in fig. 5.7, is characterised by a distribution of minimum distances between LKr clusters that has a peak at approximately 10 cm. As it can be inferred from fig. 5.13, this value is just below

the minimum observed distance between any two pairs of  $K^+ \rightarrow \pi^+\pi^+\gamma$  clusters, and therefore will cause an increase of events with clusters corresponding to merged photons.

For this choice of angle, the average number of trials for  $K^+ \rightarrow \pi^+\pi^0\pi^0$  was estimated to be  $\bar{N} = 18$ .

## 5.4 Measurement of the BR

The BR of  $K^+ \rightarrow \pi^+\gamma\gamma$  is measured with respect to the precisely known BR of  $K^+ \rightarrow \pi^+\pi^0$  according to the following expression:

$$BR(K^+ \rightarrow \pi^+\gamma\gamma) = BR(K^+ \rightarrow \pi^+\pi^0) \frac{A_{\pi^+\pi^0} N_{\pi^+\gamma\gamma}}{A_{\pi^+\gamma\gamma} N_{\pi^+\pi^0}} \quad (5.6)$$

where  $N_{\pi^+\pi^0}$  represents the number of observed  $K^+ \rightarrow \pi^+\pi^0$  decays, that is the number of surviving events after applying the full selection except the final cut on the kinematic  $z$  variable. A cut on the invariant mass of the photons for them to be consistent with  $M_{\pi^0}$  is applied instead. The number of  $K^+ \rightarrow \pi^+\gamma\gamma$  events in the data sample is estimated as:

$$N_{\pi^+\gamma\gamma} = N^{obs} - N_{\pi^+\pi^0\gamma}^{exp} - N_{\pi^+\pi^0\pi^0}^{exp} \quad (5.7)$$

with the expected number of events for background channels given by:

$$N_{\pi^+\pi^0\gamma}^{exp} = N_K \times BR(K^+ \rightarrow \pi^+\pi^0\gamma) \times A_{\pi^+\pi^0\gamma} \quad (5.8)$$

$$N_{\pi^+\pi^0\pi^0}^{exp} = N_K \times BR(K^+ \rightarrow \pi^+\pi^0\pi^0) \times A_{\pi^+\pi^0\pi^0}. \quad (5.9)$$

An estimate of  $N_K$ , that is the total number of kaon decays in the FV in the data samples considered, can be obtained starting from the number of events passing the selection for  $K^+ \rightarrow \pi^+\pi^0$ . The background to the  $K^+ \rightarrow \pi^+\pi^0$  sample is below 1‰.

$$N_K \approx \frac{N_{\pi^+\pi^0}^{obs}}{BR(K^+ \rightarrow \pi^+\pi^0) \times A_{\pi^+\pi^0}} \quad (5.10)$$

Acceptances for signal and background channels are given by:  $A = \frac{N_{sel}}{N_{FV} \cdot b} \pm \sqrt{\frac{A \times (1-A)}{N_{FV} \cdot b}}$ , where  $N_{sel}$  is the number of events surviving the selection for  $K^+ \rightarrow \pi^+ \gamma \gamma$ ,  $N_{FV}$  is the number of kaon decays in the FV for the MC sample considered, and  $b$  is the bias factor, equal to 1 for non-biased samples, and to the average number of iterations  $\bar{N}$  required to produce an event satisfying the biasing conditions otherwise. The value of  $b$  for  $K^+ \rightarrow \pi^+ \pi^0 \pi^0$  was presented in the previous section.

In the next sections, two estimates of the BR are presented. The first one is performed over the whole signal region, defined as  $z > 0.225$ . Such an estimate is highly sensitive to the shape of the differential decay spectrum for the  $z$  variable, determined by the Chiral Perturbation Theory (ChPT) parameter  $\hat{c}$ , as discussed in chapter 1. Different values of  $\hat{c}$  therefore produce different  $z$  distributions, with a significant impact on the number of events in the accepted  $z$  range. As the BR measurement relies on estimating the acceptance of  $K^+ \rightarrow \pi^+ \gamma \gamma$  using a MC sample generated for a specific value of  $\hat{c}$ , the BR estimate depends strongly on the latter parameter, and therefore this measurement is model-dependent.

For the second BR estimate, the accepted  $z$  region is sub-divided in bins, and the BR measurement is performed in each of them. In each  $z$  bin, a variation in  $\hat{c}$  has a smaller effect on the shape of the  $z$  distribution, and therefore on the  $K^+ \rightarrow \pi^+ \gamma \gamma$  acceptance, with respect to a measurement in the full range. Smaller bin sizes correspond to smaller dependence on the model. However, an effect due to *migration* of events to neighbouring bins after the event is reconstructed, described in the next sub-sections, introduces further uncertainties on the BR estimates. The bin size is chosen keeping in mind the impact of both effects. As shown in table 5.5, the model independent results are compatible for all the investigated values of  $\hat{c}$ .

Process	BR(PDG)	Acceptance	$N_{exp}$
$K^+ \rightarrow \pi^+ \gamma \gamma$ ( $\hat{c} = 1.86$ )	$(1.01 \pm 0.06) \times 10^{-6}$	$(10.37 \pm 0.01)\%$	$1217 \pm 72$
$K^+ \rightarrow \pi^+ \pi^0(\gamma)$ (IB)	$(20.67 \pm 0.08)\%$	$(1.4 \pm 0.1) \times 10^{-5}$	$114 \pm 7$
$K^+ \rightarrow \pi^+ \pi^0 \pi^0$	$(1.760 \pm 0.023)\%$	$(1.2 \pm 0.4) \times 10^{-7}$	$25 \pm 8$

Table 5.3: Acceptances, BR from the Particle Data Group (PDG) [64], and number of expected events for the signal (with  $\hat{c} = 1.86$ ) and background channels.

### 5.4.1 Model-dependent BR estimate

A previous measurement of the  $\hat{c}$  parameter by the combined analysis of NA62/2 and NA48 samples yields [51]:

$$\hat{c} = 1.86 \pm 0.25 \quad (5.11)$$

The BR estimate presented below uses the measured value  $\hat{c} = 1.86$ . The acceptances and the number of expected events for the signal and the two backgrounds are shown in table 5.3.

The resulting estimate of the model-dependent BR and its uncertainty is:

$$BR^{MD}(K^+ \rightarrow \pi^+ \gamma \gamma) = (0.86 \pm 0.04) \times 10^{-6} \quad (5.12)$$

The distributions of the  $z$  variable for data, for the expected signal for  $\hat{c} = 1.86$ , and for the background is shown in fig. 5.9

### 5.4.2 Model-independent BR estimate

A model-independent measurement of the BR of  $K^+ \rightarrow \pi^+ \gamma \gamma$  can be performed in bins of the kinematic variable  $z$ . The BR estimates become:

$$BR^{(i)}(K^+ \rightarrow \pi^+ \gamma \gamma) = BR(K^+ \rightarrow \pi^+ \pi^0) \times \frac{A_{\pi^+ \pi^0}}{A_{\pi^+ \gamma \gamma}^{(i)}} \times \frac{(N^{obs,(i)} - N_{\pi^+ \pi^0 \gamma}^{exp,(i)} - N_{\pi^+ \pi^0 \pi^0}^{exp,(i)})}{N_{\pi^+ \pi^0}^{obs}}. \quad (5.13)$$

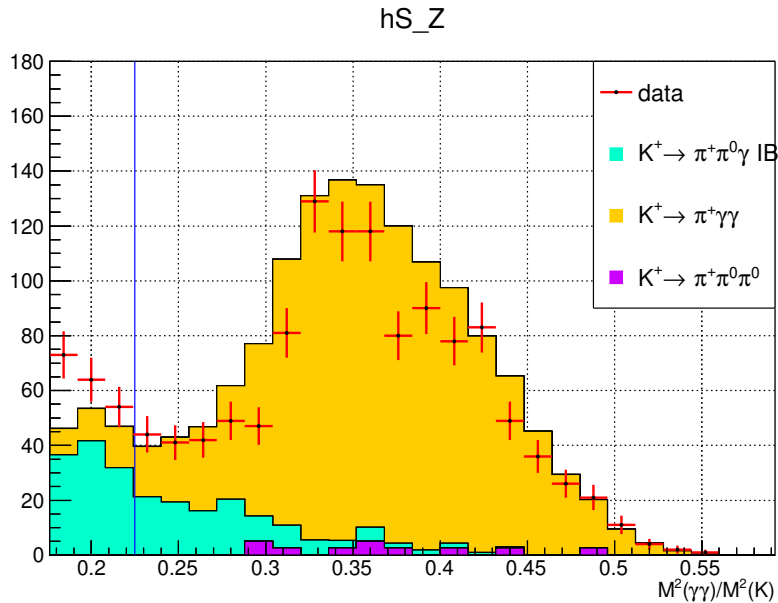


Figure 5.9: Kinematic  $z$  distribution for data (red crosses) and expected MC signal and background (filled histograms). The signal region is defined to start at  $z = 0.225$ , where background stops dominating over signal. The region is indicated in the figure by a solid blue vertical line.

Two acceptances  $A_{\pi^+\gamma\gamma}^{(i)}$  can be defined:

$$A_{\pi^+\gamma\gamma, reco}^{(i)} = \frac{N_{reco}^{sel}}{N_{true}^{gen}} \quad (5.14)$$

$$A_{\pi^+\gamma\gamma, true}^{(i)} = \frac{N_{true}^{sel}}{N_{true}^{gen}} \quad (5.15)$$

$A_{\pi^+\gamma\gamma, reco}^{(i)}$  is the ratio of the number of selected events in bins of the reconstructed variable, to the number of generated events in the corresponding bins of the true variable; the definition of  $A_{\pi^+\gamma\gamma, true}^{(i)}$  is similar, with the number of selected events in bins of the true variable in place of the reconstructed variable. The former definition is used for the computation of the BR in bins of  $z$ , while the latter is used for studying migration effects, discussed in section 5.5.2.

Initially, a constant binning was tested; however, large migration of events from the MC truth  $z$  bin to a different bin in the reconstructed  $z$  led to the choice of a variable binning. This allows grouping together neighbouring bins where large migrations occur, such as the region around the peak:  $z \approx 0.35$ . The systematic uncertainty due to bin

$(z_{min} - z_{max})$	$A^{\pi\gamma\gamma}$	$BR$
(0.225 – 0.3)	$0.1509 \pm 0.0005$	$(7.1 \pm 1.7) \times 10^{-8}$
(0.3 – 0.35)	$0.1304 \pm 0.0003$	$(2.07 \pm 0.15) \times 10^{-7}$
(0.35 – 0.3625)	$0.1256 \pm 0.0005$	$(6.9 \pm 0.8) \times 10^{-8}$
(0.3625 – 0.375)	$0.1232 \pm 0.0005$	$(4.5 \pm 0.7) \times 10^{-8}$
(0.375 – 0.3875)	$0.1194 \pm 0.0005$	$(4.9 \pm 0.8) \times 10^{-8}$
(0.3875 – 0.45)	$0.1014 \pm 0.0002$	$(2.4 \pm 0.3) \times 10^{-7}$
(0.45 – 0.515)	$0.0516 \pm 0.0002$	$(1.35 \pm 0.17) \times 10^{-7}$

Table 5.4:  $K^+ \rightarrow \pi^+\gamma\gamma$  acceptances and BR estimate in bins of the  $z$  variable.

migration is discussed in section 5.5.2.

The estimated acceptance for  $K^+ \rightarrow \pi^+\gamma\gamma$  and the measured BR in bins of  $z$  in the signal region is presented in table 5.4. The combined estimate obtained by summing the measurements over the seven  $z$  bins is given by:

$$BR_{MI} = (0.82 \pm 0.04) \times 10^{-6}. \quad (5.16)$$

This can be compared to previous results from the analysis of NA62 data:  $BR_{MI} = (1.088 \pm 0.093) \times 10^{-6}$  [51]. The results are compatible within  $2.6 \sigma$ . Part of the discrepancy is due to the fact that the sum was performed over bins starting at a lower values of  $z$  ( $z > 0.2$ ). Several systematic studies were performed; they are described in section 5.5.

## 5.5 Study of systematics

Several systematic effects on the measurement of the  $K^+ \rightarrow \pi^+\gamma\gamma$  BR were performed. They are related to the  $\hat{c}$  dependence of the BR, the  $z$  bin migration between true and reconstructed variable, accidental combinations of tracks and clusters, the distance between clusters, and LKr clusters merging. All the above studies are discussed in the present section.

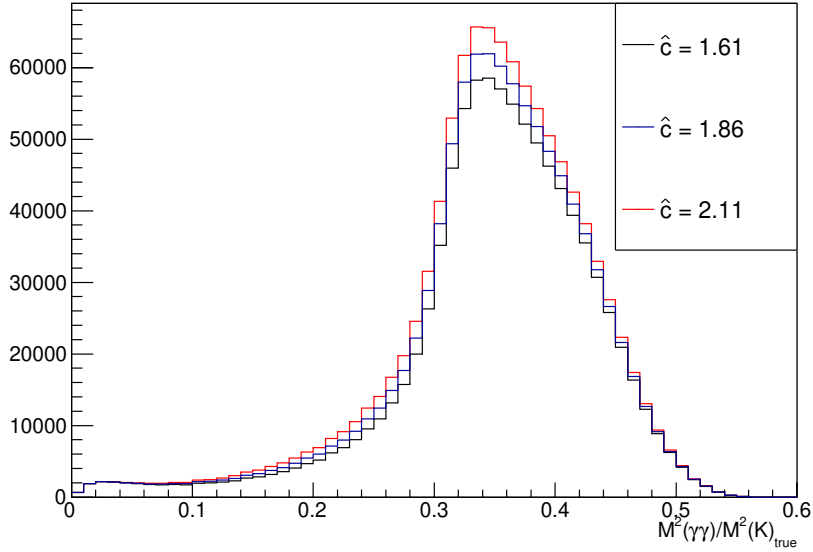


Figure 5.10: MC truth kinematic  $z$  distribution for selected events, for different values of the  $\hat{c}$  parameter.

### 5.5.1 BR dependence on the model parameters

As discussed in section 5.4.2, a measurement of the BR of  $K^+ \rightarrow \pi^+ \gamma \gamma$  relies on the  $\hat{c}$  parameter of the generator model. The variation in the acceptance due to different values of the  $\hat{c}$  parameter in the differential decay spectrum has been estimated via event-by-event reweighting. The true  $z$  distribution for selected events is shown in fig. 5.10, whereas the acceptance in the chosen binning is in fig. 5.11. In the figures, the distributions for the central value are shown, together with the values  $\hat{c} = 1.61$  and  $2.11$ , corresponding to the central value and the  $1 \sigma$  interval extremes for the previous estimate. Different  $\hat{c}$  values are indicated by different colored lines. In fig. 5.10, the acceptance for  $\hat{c} = 1$  is also plotted to show the effect due to a larger  $\hat{c}$  variation.

The BR estimates in bins of  $z$  for the three values of  $\hat{c} = 1.61, 1.86, 2.11$  are reported in table 5.5.

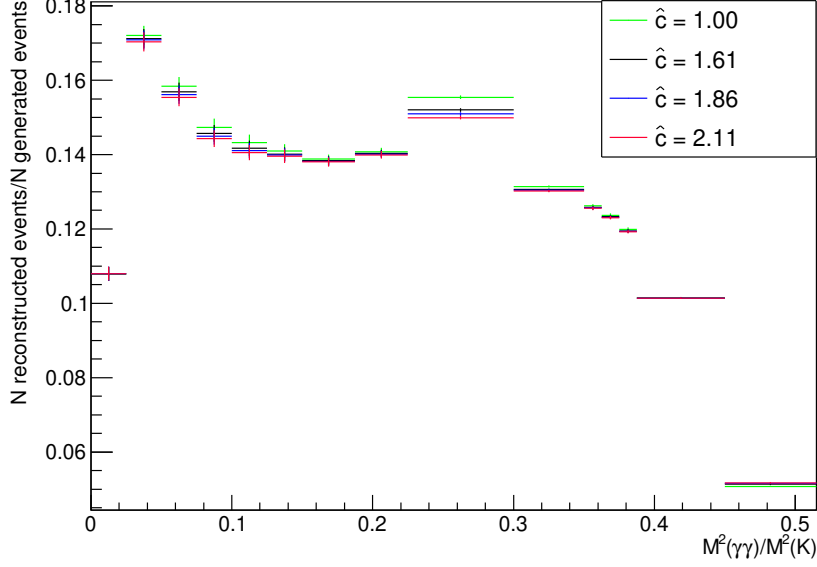


Figure 5.11:  $A_{\pi^+\gamma\gamma, reco}^{(i)}$  in bins of the kinematic  $z$  variable for various models of the ChPT parameter  $\hat{c}$ .

$(z_{min}, z_{max})$	$BR(\hat{c} = 1.86)$	$BR(\hat{c} = 1.61)$	$BR(\hat{c} = 2.11)$
(0.225, 0.3)	$(7.1 \pm 0.9) \times 10^{-8}$	$(7.0 \pm 0.9) \times 10^{-8}$	$(7.1 \pm 1.0) \times 10^{-8}$
(0.3, 0.35)	$(2.07 \pm 0.16) \times 10^{-7}$	$(2.06 \pm 0.16) \times 10^{-7}$	$(2.07 \pm 0.16) \times 10^{-7}$
(0.35, 0.3625)	$(6.9 \pm 1.0) \times 10^{-8}$	$(6.9 \pm 1.0) \times 10^{-8}$	$(6.9 \pm 1.0) \times 10^{-8}$
(0.3625, 0.375)	$(4.5 \pm 0.8) \times 10^{-8}$	$(4.4 \pm 0.8) \times 10^{-8}$	$(4.5 \pm 0.8) \times 10^{-8}$
(0.375, 0.3875)	$(4.9 \pm 0.8) \times 10^{-8}$	$(4.9 \pm 0.8) \times 10^{-8}$	$(4.9 \pm 0.8) \times 10^{-8}$
(0.3875, 0.45)	$(2.37 \pm 0.20) \times 10^{-7}$	$(2.37 \pm 0.20) \times 10^{-7}$	$(2.37 \pm 0.20) \times 10^{-7}$
(0.45, 0.515)	$(1.35 \pm 0.21) \times 10^{-7}$	$(1.36 \pm 0.21) \times 10^{-7}$	$(1.35 \pm 0.21) \times 10^{-7}$

Table 5.5: BR for  $K^+ \rightarrow \pi^+\gamma\gamma$  for  $\hat{c} = 1.61, 1.86, 2.11$  in seven bins of the kinematic variable  $z$  in the signal region.

$(z_{min}, z_{max})$	$A^{\pi\gamma\gamma}(\hat{c} = 1.86)_{reco}$	$A^{\pi\gamma\gamma}(\hat{c} = 1.86)_{true}$	$\Delta A/A$
0.225 – 0.3	$0.1509 \pm 0.0005$	$0.1328 \pm 0.0004$	0.11995
0.3 – 0.35	$0.1304 \pm 0.0003$	$0.1288 \pm 0.0003$	0.01227
0.35 – 0.3625	$0.1256 \pm 0.0005$	$0.1262 \pm 0.0005$	-0.00478
0.3625 – 0.375	$0.1232 \pm 0.0005$	$0.1239 \pm 0.0005$	-0.00568
0.375 – 0.3875	$0.1194 \pm 0.0005$	$0.1205 \pm 0.0005$	-0.00921
0.3875 – 0.45	$0.1014 \pm 0.0002$	$0.1074 \pm 0.0002$	-0.05917
0.45 – 0.515	$0.0516 \pm 0.0002$	$0.0573 \pm 0.0002$	-0.11047

Table 5.6: Acceptance, in seven bins of the kinematic variable  $z$  in the signal region, for the ChPT parameter  $\hat{c} = 1.86$ , according to two different definitions based respectively on the true and the reconstructed  $z$  variable for selected events. The relative variation is also shown.

### 5.5.2 Systematic uncertainties from $z$ bin migration

As discussed in section 5.4.2, the  $z$  variable migrates from the MC truth bin to a different reconstructed  $z$  bin. The systematic uncertainty due to bin migration is determined by the relative change in acceptance in each bin between the true and reconstructed  $z$  distributions. The difference in the acceptance for true and reconstructed  $z$  is shown in fig. 5.12; the effect of bin migration on the acceptance estimate for each  $z$  bin is reported in table 5.6.

### 5.5.3 Systematic uncertainty from the accidental combinations of one track and two clusters

The selection for  $K^+ \rightarrow \pi^+\gamma\gamma$  excludes accidental activity by rejecting events in which more than one group of one track and two clusters compatible in time are found, as explained in section 5.2. The systematic uncertainty on the BR measurement due to the accidental coincidence of one track and two clusters in time was estimated by identifying events in which multiple such groups are found, and randomly selecting one of them to proceed to the further stages of the selection. The systematic effect on the BR when including accidental combinations of one track and two clusters is reported in the summary tables in section 5.5.6.

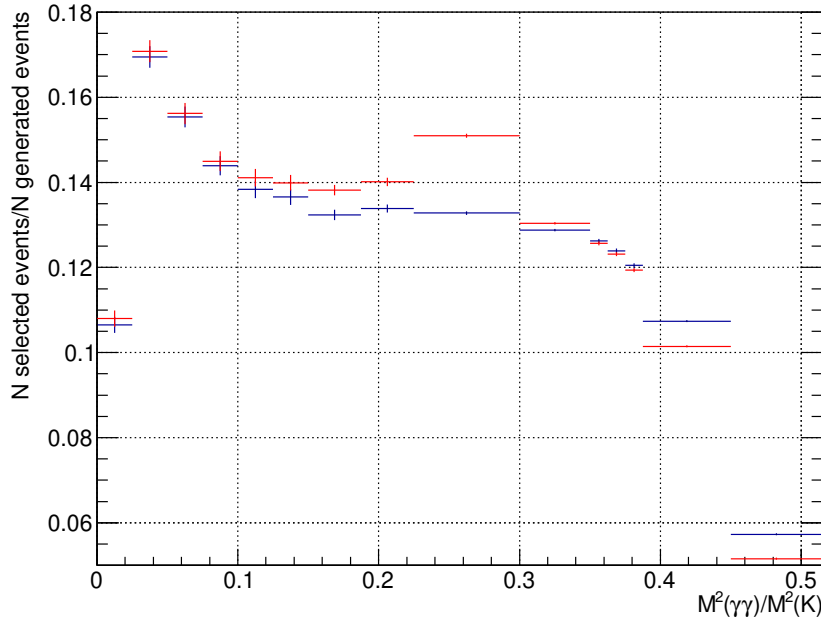


Figure 5.12: Comparison of the acceptance definitions  $A_{\pi^+\gamma\gamma, reco}^{(i)}$  and  $A_{\pi^+\gamma\gamma, true}^{(i)}$ ; larger discrepancies are produced by event migration from a MC truth  $z$  bin to a different reconstructed  $z$  bin.

#### 5.5.4 BR dependence on cluster merging

As merged clusters are responsible for the major background component, it must be ensured that no systematic effect due to a different merging behaviour in data and MC is observed. To this end, the distance between any two clusters in each event is was plotted for data and for  $K^+ \rightarrow \pi^+\pi^0\gamma$  (IB) MC; the distributions are shown in fig. 5.13. For data, the distribution is shown both without timing cuts applied (yellow), and with a maximum  $\Delta t = 10$  ns time cut between clusters (green). The distribution for MC is shown in orange. By comparing the distributions' end points one can infer from what distance clusters start to be merged.

When applying the 10 ns timing cut, the same used in the  $K^+ \rightarrow \pi^+\gamma\gamma$  selection, the data and MC distributions have very similar end points; one can thus conclude that the systematic effect due to different data/MC merging merging behaviour can be neglected.

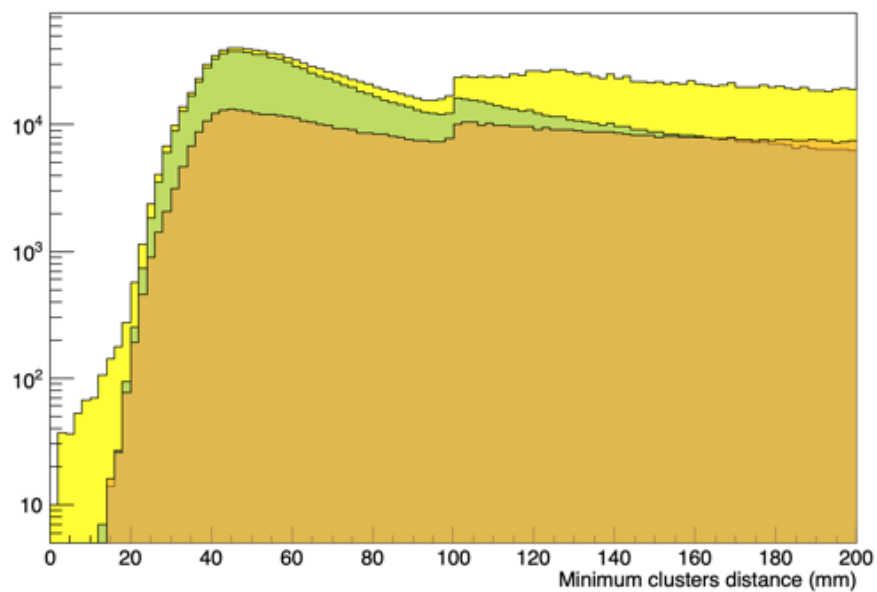


Figure 5.13: Minimum distance between any two clusters for data with no time cut (yellow), data with a 10 ns time cut (green), and  $K^+ \rightarrow \pi^+\pi^0\gamma$  (IB) (orange). The data distribution is plotted with minimum selection cuts and therefore does not match the MC distribution's shape; the former, with a 10 ns time cut, and the latter, have approximately equal starting points, suggesting that there are no differences in the cluster merging behaviours for data and MC.

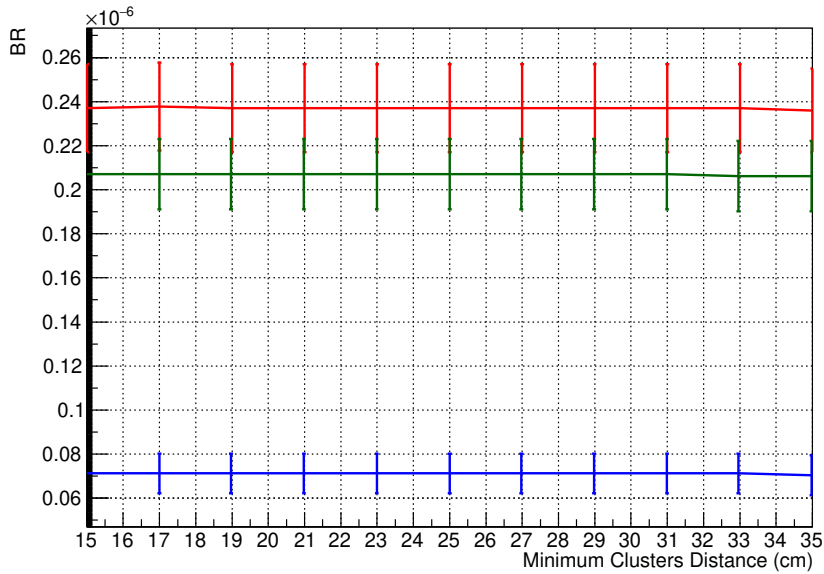


Figure 5.14: BR estimate as a function of the required minimum distance between clusters for three  $z$  bins:  $0.225 < z < 0.3$  (blue),  $0.3 < z < 0.35$  (green),  $0.3875 < z < 0.45$  (red). Only when setting the cut above 33 cm and 25 cm a slight variation of the BR is observed; this is, anyway, well below the statistical error.

### 5.5.5 BR dependence on cluster distance

The signal selection requires clusters in a  $K^+ \rightarrow \pi^+\gamma\gamma$  decay candidate to be at least 25 cm apart. The variation of the BR when this cut is varied at steps of 5 cm in the interval (25 cm, 35 cm) was studied. The BR was found to be unchanged between 15 cm and 31 cm; at 33 cm and 35 cm, the BR exhibits a variations at level of 1.5% ( $0.225 < z < 0.3$ ), 0.5% ( $0.3 < z < 0.35$ ), and 0.4% ( $0.3875 < z < 0.45$ ), in each case well below the statistical uncertainty. The BR stability plot for the above three  $z$  bins can be found in fig. 5.14.

### 5.5.6 Summary and prospects

A model-dependent and a model-independent measurement of the BR of  $K^+ \rightarrow \pi^+\gamma\gamma$  in bins of  $z$  were carried out. The latter was performed on seven bins of the kinematic variable  $z$ . Five systematic studies were performed, and four effects were identified that affect the estimate of the BR. The BR for each  $z$  bin, together with its statistical uncertainty and

the breakdown of MC-related and systematic uncertainties are presented respectively in table 5.7. The combined model independent measurement over the seven  $z$  bins is shown in eq. (5.16).

A direct comparison with previous results is not feasible as the  $z$  binning chosen in the present work, optimised to absorb event migrations within near regions, is different from the one used before, and the signal region is defined to start at a larger value of  $z$ . A fully model-independent measurement can be carried out by performing a likelihood fit to the data distribution of the kinematic  $z$  variable to extract the value of the ChPT  $\hat{c}$  parameter. The data distribution can be compared to a number of template MC distributions generated according to different values of  $\hat{c}$ ; the template corresponding to the maximum likelihood constitutes the best  $\hat{c}$  estimate. The best value of  $\hat{c}$  would provide a handle to compare the current results with previous ones. Because of time constraints, such procedure was not performed as part of this work, and constitutes a future development of the  $K^+ \rightarrow \pi^+ \gamma \gamma$  analysis.

$(z_{min}, z_{max})$	$BR$	$\sigma_{data}$	$\sigma_{K^+ \rightarrow \pi^+ \pi^0 \gamma}$	$\sigma_{K^+ \rightarrow \pi^+ \pi^0 \pi^0}$	$\sigma_{MC}$	$\sigma_{tot}$	$\Delta_{model}$	$\Delta_{acc}$	$\Delta_{mig}$
(0.225, 0.3)	$7.1 \times 10^{-8}$	$0.5 \times 10^{-8}$	$0.02 \times 10^{-8}$	$0.03 \times 10^{-8}$	$0.10 \times 10^{-8}$	$0.5 \times 10^{-8}$	$0.1 \times 10^{-8}$	/	$1.6 \times 10^{-8}$
(0.3, 0.35)	$2.07 \times 10^{-7}$	$0.11 \times 10^{-7}$	$0.13 \times 10^{-8}$	$0.08 \times 10^{-8}$	$0.12 \times 10^{-8}$	$0.11 \times 10^{-7}$	$0.01 \times 10^{-7}$	$0.06 \times 10^{-7}$	$0.09 \times 10^{-7}$
(0.35, 0.3625)	$6.9 \times 10^{-8}$	$0.6 \times 10^{-8}$	$0.02 \times 10^{-8}$	$0.03 \times 10^{-8}$	$0.12 \times 10^{-8}$	$0.7 \times 10^{-8}$	/	$0.4 \times 10^{-8}$	/
(0.3625, 0.375)	$4.5 \times 10^{-8}$	$0.5 \times 10^{-8}$	$0.01 \times 10^{-8}$	$0.02 \times 10^{-8}$	$0.13 \times 10^{-8}$	$0.5 \times 10^{-8}$	$0.1 \times 10^{-8}$	$0.2 \times 10^{-8}$	$0.5 \times 10^{-8}$
(0.375, 0.3875)	$4.9 \times 10^{-8}$	$0.6 \times 10^{-8}$	/	$0.02 \times 10^{-8}$	$0.13 \times 10^{-8}$	$0.6 \times 10^{-8}$	/	$0.2 \times 10^{-8}$	$0.2 \times 10^{-8}$
(0.3875, 0.45)	$2.37 \times 10^{-7}$	$0.14 \times 10^{-7}$	$0.08 \times 10^{-8}$	$0.09 \times 10^{-8}$	$0.02 \times 10^{-7}$	$0.14 \times 10^{-7}$	/	$0.01 \times 10^{-7}$	$0.22 \times 10^{-7}$
(0.45, 0.515)	$1.35 \times 10^{-7}$	$0.14 \times 10^{-7}$	$0.08 \times 10^{-8}$	$0.05 \times 10^{-8}$	$0.03 \times 10^{-7}$	$0.15 \times 10^{-7}$	$0.01 \times 10^{-7}$	$0.04 \times 10^{-7}$	$0.04 \times 10^{-7}$

Table 5.7: BR in seven bins of the  $z$  variable, together with its statistical, MC and systematic uncertainties. The systematic uncertainties due to different effects are presented separately. From left to right, each column represents: the  $z$  range covered by the bin, the BR value, the statistic uncertainty, the uncertainty due to the  $K^+ \rightarrow \pi^+ \pi^0 \gamma$  and  $K^+ \rightarrow \pi^+ \pi^0 \pi^0$  sample sizes, the total uncertainty due to MC samples, the total uncertainty excluding systematics, the uncertainty due to the dependency on the model (*mod*), the uncertainty due to the  $z$  variable migration from true to reconstructed bins (*mig*), the uncertainty due to the inclusion of accidental combinations of one track and two clusters (*acc*)

## CONCLUSION

In this thesis, the research I performed at the NA62 experiment at CERN was presented. The development in the NA62 trigger framework of decoding tools for the STRAW sub-detector, allowing the execution of High-Level Trigger algorithms for this sub-system, and the implementation of structures through which triggered data is sent to storage have been discussed. Studies carried out to assess the performance of the KTAG sub-detector between 2016 and 2018 have been presented; they allow to conclude that the sub-detector's efficiency was well above the 95% threshold during the whole data-taking, including a period in which a read-out board malfunctioned. A model-dependent measurement of the BR of the  $K^+ \rightarrow \pi^+ \gamma \gamma$  decay and a model-independent measurement in bins of the kinematic  $z$  variable on the world largest data sample, collected at the NA62 experiment, have been presented. The combined model-independent estimate over seven  $z$  bins is:

$$BR_{MI} = (0.73 \pm 0.04) \times 10^{-6} \quad (5.17)$$

A direct comparison with previous results was not carried out due to the different definitions of signal region in the  $z$  variable and the different binning; the future perspectives of this analysis include fitting the shape of the kinematic  $z$  distribution to extract the value of the ChPT  $\hat{c}$  parameter, which would allow a comparison with previous experimental results.

## LIST OF REFERENCES

- [1] Y. Fukuda, T. Hayakawa, E. Ichihara, K. Inoue, K. Ishihara, H. Ishino, Y. Itow, T. Kajita, J. Kameda, S. Kasuga, and et al. Measurement of the flux and zenith-angle distribution of upward throughgoing muons by super-kamiokande. *Physical Review Letters*, 82(13):2644–2648, Mar 1999.
- [2] Ying Li and Cai-Dian Lü. Recent anomalies in b physics. *Science Bulletin*, 63(5):267–269, Mar 2018.
- [3] Ashutosh Kumar Alok, Amol Dighe, Shireen Gangal, and Dinesh Kumar. Continuing search for new physics in  $b \rightarrow \mu\mu$  decays: two operators at a time. *Journal of High Energy Physics*, 2019(6), Jun 2019.
- [4] R. Aaij, B. Adeva, M. Adinolfi, Z. Ajaltouni, S. Akar, J. Albrecht, F. Alessio, M. Alexander, S. Ali, G. Alkhazov, and et al. Measurement of the  $b_s^0 \rightarrow \mu^+\mu^-$  branching fraction and effective lifetime and search for  $b^0 \rightarrow \mu^+\mu^-$  decays. *Physical Review Letters*, 118(19), May 2017.
- [5] E. Cortina Gil et al. First search for  $k^+ \rightarrow \pi^+\nu\bar{\nu}$  using the decay-in-flight technique. *Physics Letters B*, 791:156 – 166, 2019.
- [6] J. K. Ahn, B. Beckford, and J. et al. Beechert. Search for  $K_L \rightarrow \pi^0\nu\bar{\nu}$  and  $K_L \rightarrow \pi^0 X^0$  decays at the j-parc koto experiment. *Phys. Rev. Lett.*, 122:021802, Jan 2019.
- [7] G. D. Rochester and C. C. Butler. Evidence for the Existence of New Unstable Elementary Particles. *Nature*, 160:855–857, 1947.

- [8] M. Kobayashi and T. Maskawa. CP-Violation in the Renormalizable Theory of Weak Interaction. *Progress of Theoretical Physics*, 49:652–657, February 1973.
- [9] N. Cabibbo. Unitary Symmetry and Leptonic Decays. *Physical Review Letters*, 10:531–533, June 1963.
- [10] M. Tanabashi et al. Review of Particle Physics. *Phys. Rev.*, D98(3):030001, 2018.
- [11] R. Aaij, B. Adeva, M. Adinolfi, A. Affolder, Z. Ajaltouni, S. Akar, J. Albrecht, F. Alessio, M. Alexander, S. Ali, and et al. Test of lepton universality using  $b^+ \rightarrow k^+ l^+ l^-$  decays. *Physical Review Letters*, 113(15), Oct 2014.
- [12] M. Gell-Mann and A. Pais. *Proceedings of the 1954 Glasgow Conference on Nuclear and Meson Physics*, E.H. Bellamy and R.G. Moorhouse (eds.) London, page 342, 1954.
- [13] M. Gell-Mann and A. Pais. Behavior of neutral particles under charge conjugation. *Phys. Rev.*, 97:1387–1389, Mar 1955.
- [14] T. D. Lee and Chen-Ning Yang. Question of Parity Conservation in Weak Interactions. *Phys. Rev.*, 104:254–258, 1956.
- [15] C. S. Wu, E. Ambler, R. W. Hayward, D. D. Hoppes, and R. P. Hudson. Experimental test of parity conservation in beta decay. *Phys. Rev.*, 105:1413–1415, Feb 1957.
- [16] J. H. Christenson, J. W. Cronin, V. L. Fitch, and R. Turlay. Evidence for the  $2\pi$  decay of the  $k_2^0$  meson. *Phys. Rev. Lett.*, 13:138–140, Jul 1964.
- [17] J.R Batley, R.S Dosanjh, T.J Gershon, G.E Kalmus, C Lazzeroni, D.J Munday, E Olaiya, M Patel, M.A Parker, T.O White, and et al. A precision measurement of direct cp violation in the decay of neutral kaons into two pions. *Physics Letters B*, 544(1-2):97–112, Sep 2002.
- [18] E. Abouzaid et al. Precise Measurements of Direct CP Violation, CPT Symmetry, and Other Parameters in the Neutral Kaon System. *Phys. Rev.*, D83:092001, 2011.

- [19] Murray Gell-Mann. A Schematic Model of Baryons and Mesons. *Phys. Lett.*, 8:214–215, 1964.
- [20] S. L. Glashow, J. Iliopoulos, and L. Maiani. Weak interactions with lepton-hadron symmetry. *Phys. Rev. D*, 2:1285–1292, Oct 1970.
- [21] Augusto Ceccucci. Review and Outlook on Kaon Physics. *Acta Phys. Polon.*, B49:1079–1086, 2018.
- [22] A. D. Sakharov. Violation of CP Invariance, C asymmetry, and baryon asymmetry of the universe. *Pisma Zh. Eksp. Teor. Fiz.*, 5:32–35, 1967. [Usp. Fiz. Nauk161,no.5,61(1991)].
- [23] Cristina Lazzeroni. Lepton universality tests with leptonic kaon decays. In *CKM unitarity triangle. Proceedings, 6th International Workshop, CKM 2010, Warwick, UK, September 6-10, 2010*, 2011.
- [24] Jack L. Ritchie and Stanley G. Wojcicki. Rare  $k$  decays. *Rev. Mod. Phys.*, 65:1149–1197, Oct 1993.
- [25] Eduardo Cortina Gil et al. Searches for lepton number violating  $K^+$  decays. *Phys. Lett.*, B797:134794, 2019.
- [26] Yuval Grossman and Yosef Nir. beyond the standard model. *Physics Letters B*, 398(1-2):163–168, Apr 1997.
- [27] R. Barbieri, D. Buttazzo, F. Sala, and D. M. Straub. Flavour physics and flavour symmetries after the first lhc phase. *Journal of High Energy Physics*, 2014(5), May 2014.
- [28] Monika Blanke, Andrzej J. Buras, Bjoern Duling, Stefan Recksiegel, and Cecilia Tarantino. Fenc processes in the littlest higgs model with t-parity: an update, 2009.

- [29] Andrzej J. Buras, Fulvia De Fazio, and Jennifer Girrbach. The anatomy of  $z'$  and  $z$  with flavour changing neutral currents in the flavour precision era. *Journal of High Energy Physics*, 2013(2), Feb 2013.
- [30] Andrzej J. Buras, Dario Buttazzo, Jennifer Girrbach-Noe, and Robert Knegjens. Can we reach the zeptouniverse with rare k and b s,d decays? *Journal of High Energy Physics*, 2014(11), Nov 2014.
- [31] Monika Blanke, Andrzej J Buras, Björn Duling, Katrin Gemmler, and Stefania Gori. Rare k and b decays in a warped extra dimension with custodial protection. *Journal of High Energy Physics*, 2009(03):108–108, Mar 2009.
- [32] Andrzej J. Buras, Dario Buttazzo, and Robert Knegjens.  $k \rightarrow \pi\nu\bar{\nu}$  and  $\frac{e'}{e}$  in simplified new physics models. *Journal of High Energy Physics*, 2015(11), Nov 2015.
- [33] R. Bernabei, P. Belli, A. Bussolotti, F. Cappella, V. Caracciolo, R. Cerulli, C.J. Dai, A. d' Angelo, A. Di Marco, and et al. First model independent results from dama/libra-phase2. *Nuclear Physics and Atomic Energy*, 19(4):307–325, Dec 2018.
- [34] Katarzyna Frankiewicz. Searching for dark matter annihilation into neutrinos with super-kamiokande, 2015.
- [35] A. M. Sirunyan, A. Tumasyan, W. Adam, F. Ambroggi, E. Asilar, T. Bergauer, J. Brandstetter, E. Brondolin, M. Dragicevic, and et al. Search for low mass vector resonances decaying into quark-antiquark pairs in proton-proton collisions at  $s = 13 \sqrt{s} = 13$  tev. *Journal of High Energy Physics*, 2018(1), Jan 2018.
- [36] M. About, G. Aad, B. Abbott, O. Abdinov, B. Abeloos, S. H. Abidi, O.S. AbouZeid, N. L. Abraham, H. Abramowicz, H. Abreu, and et al. Search for low-mass dijet resonances using trigger-level jets with the atlas detector in pp collisions at  $s=13$  tev. *Physical Review Letters*, 121(8), Aug 2018.

- [37] CMS Collaboration. Search for decays of stopped exotic long-lived particles produced in proton-proton collisions at  $\sqrt{s} = 13$  tev, 2017.
- [38] A. M. Sirunyan, A. Tumasyan, W. Adam, F. Ambrogi, E. Asilar, T. Bergauer, J. Brandstetter, E. Brondolin, M. Dragicevic, and et al. Combined search for electroweak production of charginos and neutralinos in proton-proton collisions at  $\sqrt{s} = 13$ tev. *Journal of High Energy Physics*, 2018(3), Mar 2018.
- [39] ATLAS Collaboration. Search for electroweak production of supersymmetric particles in final states with two or three leptons at  $\sqrt{s} = 13$  tev with the atlas detector, 2018.
- [40] M. About, G. Aad, B. Abbott, O. Abdinov, B. Abeloos, S. H. Abidi, O. S. AbouZeid, N. L. Abraham, H. Abramowicz, H. Abreu, and et al. Search for long-lived, massive particles in events with displaced vertices and missing transverse momentum in s=13 tev pp collisions with the atlas detector. *Physical Review D*, 97(5), Mar 2018.
- [41] G. Aad, B. Abbott, J. Abdallah, O. Abdinov, B. Abeloos, R. Aben, O. S. AbouZeid, N. L. Abraham, H. Abramowicz, and et al. Measurements of the higgs boson production and decay rates and constraints on its couplings from a combined atlas and cms analysis of the lhc pp collision data at s = 7  $\sqrt{s} = 7$  and 8 tev. *Journal of High Energy Physics*, 2016(8), Aug 2016.
- [42] Hyun Min Lee. Lectures on Physics Beyond the Standard Model. 2019.
- [43] Wim de Boer and Christian Sander. Global electroweak fits and gauge coupling unification, 2003.
- [44] G. Ecker. Chiral perturbation theory. *Progress in Particle and Nuclear Physics*, 35:1–80, Jan 1995.
- [45] Vincenzo Cirigliano, Gerhard Ecker, Helmut Neufeld, Antonio Pich, and Jorge Portolés. Kaon decays in the standard model. *Reviews of Modern Physics*, 84(1):399–447, Mar 2012.

- [46] A. Pich. Chiral perturbation theory. *Rept. Prog. Phys.*, 58:563–610, 1995.
- [47] G. Ecker, J. Kambor, and D. Wyler. Resonances in the weak chiral lagrangian. *Nuclear Physics B*, 394(1):101 – 138, 1993.
- [48] Antonio Pich and Eduardo de Rafael. Four quark operators and nonleptonic weak transitions. *Nucl. Phys.*, B358:311–382, 1991.
- [49] G Ecker, Antonio Pich, and E De Rafael. Radiative kaon decays and CP violation in chiral perturbation theory. *Nucl. Phys. B*, 303(CERN-TH-4853-87. UWTHPH-1987-31):665–702. 44 p, Sep 1987.
- [50] G. D’Ambrosio and J. Portoles. Unitarity and vector meson contributions to  $K^+ \rightarrow \pi^+ \gamma \gamma$ . *Phys. Lett.*, B386:403–412, 1996. [Erratum: *Phys. Lett.*B395,389(1997)].
- [51] C. Lazzeroni et al. Study of the  $K^\pm \rightarrow \pi^\pm \gamma \gamma$  decay by the NA62 experiment. *Phys. Lett.*, B732:65–74, 2014.
- [52] Eduardo Cortina Gil et al. The Beam and detector of the NA62 experiment at CERN. *JINST*, 12(05):P05025, 2017.
- [53] CERN CDS Open Photos.
- [54] V. Fanti et al. The Beam and detector for the NA48 neutral kaon CP violations experiment at CERN. *Nucl. Instrum. Meth.*, A574:433–471, 2007.
- [55] R. Ammendola et al. The integrated low-level trigger and readout system of the CERN NA62 experiment. *Nucl. Instrum. Meth.*, A929:1–22, 2019.
- [56] Claude Bovet, René Maleyran, L Piemontese, Alfredo Placci, and Massimo Placidi. *The CEDAR counters for particle identification in the SPS secondary beams: a description and an operation manual*. CERN Yellow Reports: Monographs. CERN, Geneva, 1982.

- [57] Evgueni Goudzovski et al. Development of the kaon tagging system for the {NA62} experiment at {CERN}. *Nuclear Instruments and Methods in Physics Research Section A: Accelerators, Spectrometers, Detectors and Associated Equipment*, 801:86 – 94, 2015.
- [58] The NA62UK collaboration. KTAG mapping guide.
- [59] Joel Swallow. Cedar/ktag study: Impact of using h2 compared to n2. 2018 NA62 Collaboration meeting in Pisa, KTAG Working Group, internal presentation.
- [60] G. Haefeli, A. Bay, A. Gong, H. Gong, M. Muecke, N. Neufeld, and O. Schneider. The LHCb DAQ interface board TELL1. *Nucl. Instrum. Meth.*, A560:494–502, 2006.
- [61] Karim Massri. *Kaon Identification and Search for Lepton Number Violation in  $K^\pm$  decay-in-flight experiments at CERN*. PhD thesis, School of Physics and Astronomy, University of Birmingham, 8 2014.
- [62] Francis Newson. *Kaon Identification and the Search for Heavy Neutrinos at NA62*. PhD thesis, School of Physics and Astronomy, University of Birmingham, 9 2015.
- [63] Angela Romano for the KTAG working group. KTAG Pressure Scan with 2017 data, 06 2017.
- [64] C. Patrignani et al. Review of Particle Physics. *Chin. Phys.*, C40(10):100001, 2016.